

AD-A248 845



ITATION PAGE

Form Approved
OMB No. 0704-0188

REPORT SECURITY CLASSIFICATION Unclassified		1b. RESTRICTIVE MARKINGS None	
SECURITY CLASSIFICATION AUTHORITY APR 17 1992		3. DISTRIBUTION/AVAILABILITY OF REPORT Unlimited	
DECLASSIFICATION/DOWNGRADING SCHEDULE			
PERFORMING ORGANIZATION REPORT NUMBER(S)		5. MONITORING ORGANIZATION REPORT NUMBER(S)	
NAME OF PERFORMING ORGANIZATION Worcester Polytechnic Institute		7a. NAME OF MONITORING ORGANIZATION U.S. Army Materials Technology Laboratory	
6b. OFFICE SYMBOL (If applicable)		7b. ADDRESS (City, State, and ZIP Code) Watertown, MA 02172	
ADDRESS (City, State, and ZIP Code) 100 Institute Road Worcester, MA 01609			
NAME OF FUNDING/SPONSORING ORGANIZATION Group		9. PROCUREMENT INSTRUMENT IDENTIFICATION NUMBER DAAL04-90-C-0024	
6b. OFFICE SYMBOL (If applicable) SLCMT-MRM		10. SOURCE OF FUNDING NUMBERS	
ADDRESS (City, State, and ZIP Code) U.S. Army Materials Technology Laboratory Watertown, MA 02172		PROGRAM ELEMENT NO.	PROJECT NO.
		TASK NO.	WORK UNIT ACCESSION NO.

TLF (Include Security Classification)

Ultrasound NDE of Adhesive Bond Integrity: A Quantitative Measure

PERSONAL AUTHOR(S)
Ludwig, Reinhold and Sullivan, John M.

TYPE OF REPORT Final Report	13b. TIME COVERED FROM 8/17/90 TO 8/18/91	14. DATE OF REPORT (Year, Month, Day) 1992,02.28	15. PAGE COUNT 81
--------------------------------	--	---	----------------------

SUPPLEMENTARY NOTATION

COSATI CODES			18. SUBJECT TERMS (Continue on reverse if necessary and identify by block number) Ultrasonic NDE, Contact Transducer, Signal Processing, Chirp-Z Transform, Adaptive Filtering, Least Squares, Deconvolution, Bondline Transfer Function
FIELD	GROUP	SUB-GROUP	

ABSTRACT (Continue on reverse if necessary and identify by block number)

See attached sheet.

92-09853



02 4 16 001

DISTRIBUTION/AVAILABILITY OF ABSTRACT UNCLASSIFIED/UNLIMITED <input type="checkbox"/> SAME AS RPT. <input type="checkbox"/> DTIC USERS		21. ABSTRACT SECURITY CLASSIFICATION Unclassified	
NAME OF RESPONSIBLE INDIVIDUAL Robert Anastasi		22b. TELEPHONE (include Area Code) (617) 923-5241	22c. OFFICE SYMBOL SLCMT-MRM

Form 1473, JUN 86

Previous editions are obsolete

SECURITY CLASSIFICATION OF THIS PAGE

I: SUMMARY

The objective of this research was to investigate and develop a coupled approach (analytical, numerical and experimental) to the ultrasonic nondestructive evaluation of adhesive bond integrity. Results of these studies were directed toward nondestructive evaluation (NDE) of the integrity of adhesive bonds and bondlines for advanced composites and multi-layered materials by the U.S. Army. Such studies are needed in both the manufacturing phases of products in order to assure quality as well as during the operating lifetime of the products in order to predict water infiltration or bond deterioration and hence prevent failure.

The developed multiple-staged model started from a mathematical description of the ultrasound propagation through an inhomogeneous, isotropic or anisotropic solid with appropriate boundary conditions for the transmitter/receiver unit coupled to the material under test. Analytical solutions were employed to initially test and calibrate the numerical formulations. This numerical approach was configured to be flexible and realistic enough to investigate a wide variety of bond configurations on the computer.

Our strategy was targeted at the coupling of these numerical simulations of the underlying physical processes with the experimental data gathered in-house at MTL. The interaction of transducer signals with different simulated bondline configurations such as disbonds, pure bonds, and bonds of varying thickness were examined. The resulting synthetic data was compared to experimental measurements. The correlations of the experimental and numerical trials were extended to include feature extraction capability related to interfacial bond thickness. Therein, individual characteristic features representing the bond thickness were numerically isolated and overlaid with the experimentally observed signals.

This novel multi-stage approach addressed the generation and propagation of elastic waves, the wave interaction at the interface and advanced signal processing of experimental data.

An executive summary addressing each component of the original proposal is followed by detailed chapters of each work item.

Accession For	
NTIS - Unann	
9740 726	
Distribution	
Justification	
By	
Distribution/	
Availability Codes	
Dist	Avail and/or Special
A-1	

Table of Contents

	Summary	i
I	Executive Summary of Project	1
	Project Description	
	A.) Background	
	B.) Research Accomplishments	2
	C.) Work Statement of Research	6
	D.) Summary	7
	E.) Executive References	7
	F.) List of Articles Acknowledging this Project Support	8
II	Elastodynamic Wave Propagation	9
III	Finite Element Formulation	13
IV	Computational Considerations	23
V	FEM Results and Verification	35
VI	References for Chapters II - V	68
VII	Chirp-Z Transform and Adaptive Filtering	73
VIII	Appendix	81

I: EXECUTIVE SUMMARY

PROJECT DESCRIPTION

A.) Background

The integrity of bonded structures is of paramount importance in the safe and reliable operation of military equipment. The Patriot rocket requires adhesive attachment of the ceramic-dome to the Kevlar ring. Similarly, titanium components must be bonded to phenolic-based materials. Helicopter rotor blades are multilayered composites bonded together. Cobra deck panels, missile radomes, mines, projectiles, and explosive cartridges are samples of advanced military equipment requiring adhesive bonds and bondlines. The operational readiness and security of these units depend to a large extent on the integrity of the interfacial bonds.

Nondestructive evaluation of the bonds and bondlines has experienced very limited success [1]. NDE methods are needed to determine the strength of the bonds *in situ*. Unfortunately, no NDE method has demonstrated the ability to quantitatively state the strength of a bond. Several NDE techniques have been applied to assess adhesive bond quality. They include ultrasonics, acoustic emissions, radiography, holography, nuclear magnetic resonance, eddy current, and thermal imaging.[2] Of these accepted NDE methods only ultrasonics appears to retain a reasonable probability of success in the bondline application [3]. Thermal imaging requires the composite or radome shell to be of extremely small thickness. Otherwise, the thermal image of the interface is completely masked by the diffusion of heat through the substrate. Nuclear magnetic resonance has shown some success in the detection of water within bonds but it has not been able to detect disbonds, foreign matter or weak bonds. Ultrasonic pulse-echo techniques have been shown to reliably detect total disbond regions. Some investigators indicate that the strength of the adhesive layer can be correlated to the attenuation coefficient and velocity of sound in the material [4]. Interfacial and horizontally polarized shear wave measurements have demonstrated the ability to discriminate bond strength [5]. However, the test configurations were highly restrictive and the practical application of the technique is undefined as yet. Leaky Lamb waves technique uses an oblique incident wave. Usually the waves reflect off the interface, howev-

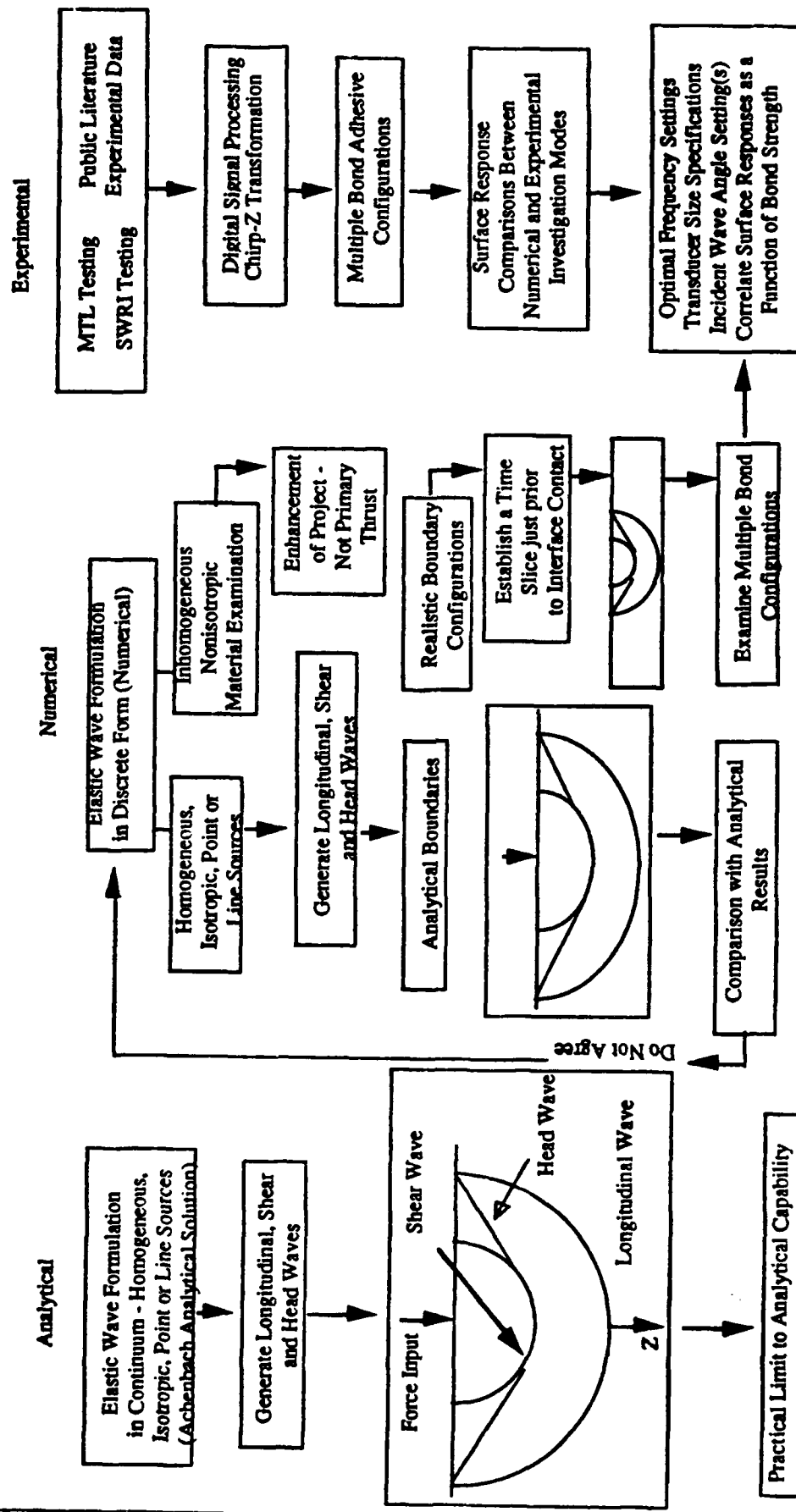
er, certain frequencies excite plate waves in the structure. These leaky waves have been shown to interfere with the expected reflection patterns [6]. Determining the correct frequency for destructive interference patterns is not reliable. Researchers have swept the frequencies to find a zone of interference. If one examines multiple frequency responses of the same test configuration small subtleties of the bond integrity can be inferred. This ability to detect weak bonds is still marginal. However, it does indicate that if one could correlate the multiple values obtained from the complex input signals then the probability of characterizing the system configuration would increase.

B.) Research Accomplishments

The basis of the research plan was the development of a multiple attack strategy as shown in Figure 1. Building on our past experience into the analytical study of transient elastic waves radiating into an elastic half-space [8], a precise model was developed which served as a calibration for our numerical formulation. This numerical model solves the transient elastodynamic equation of motion subject to realistic boundary and initial conditions in two-dimensional (x,y) space and in three-dimensional (axisymmetric) space.

Depending on the employed probe, a longitudinal or shear wave contact transducer have been simulated. The boundary and initial conditions can be set over a wide range of practically relevant bounds. Furthermore, since the model discretizes the general stress equation of motion, anisotropic and inhomogeneous material parameters can be taken into account. It is this feature of material inhomogeneity that makes our numerical modeling approach particularly suitable for bondline inspection. A realistic transducer response signal was incorporated into the numerical model and tested against the analytical theory, the propagation of the acoustic pulse was monitored throughout the test specimen. With the displacement field given at discrete instances in time it was possible to "freeze" the acoustic pulse prior to reaching the bonded area. The bond line itself can be studied in a broad fashion depending on geometric, material, and density parameters. Figure 2 shows some of the bond configurations tested using our numerical system and experimentally tested at MTL. The simulated signals are currently being stored and compared with practical measurements to train a neural net. The initial feature targeted for extraction from the data is bond thickness which is the main focus in the second phase of this project (MTL # DOD/U.S. Army - DAAL04-91-C-0054).

Figure 1 - Multiple Attack Strategy for the Solution of Adhesive Bond Integrity



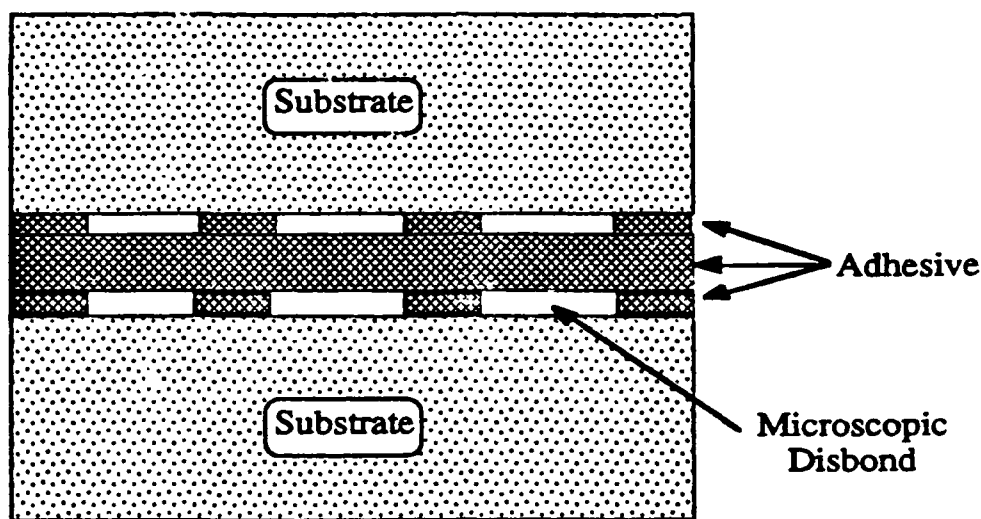


Figure 2a - Double area discontinuity model - Uniformly distributed microscopic disbonds resulting from surface contamination - Taken from Thompson.

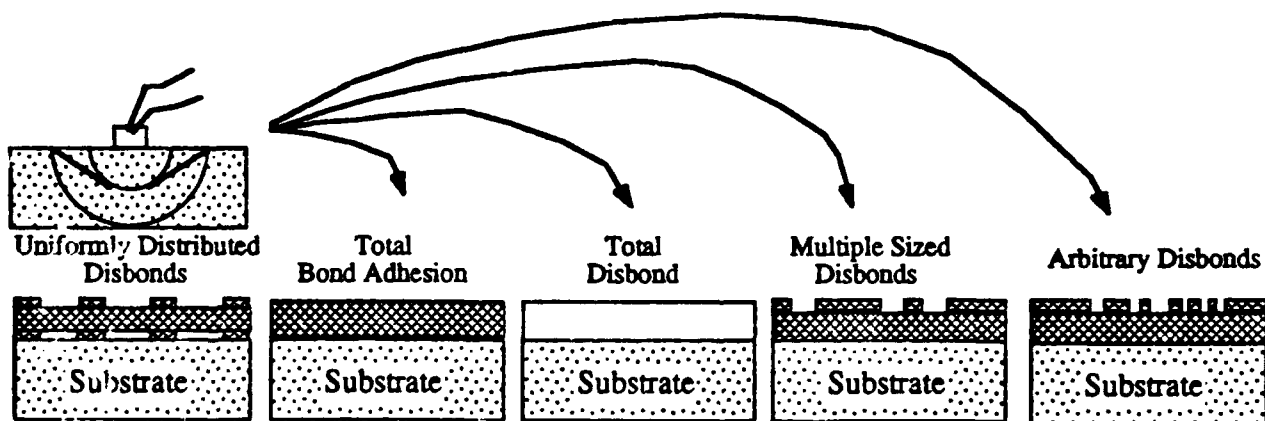


Figure 2b - Captured displacement field in upper substrate is applied to numerous bondline configurations

The use of our numerical model has allowed us:

- a) to gain crucial insight into the physical processes of ultrasound/bondline interaction. This view of the interior region and the physics of the system are evident in Figure 3. Note how the numerical model shows the longitudinal, shear, Rayleigh, and head waves propagating and reflecting within the material. This transparent window is unavailable in an experimental investigation.

- b) to generate synthetic data which can be correlated with practical measurements in order to interpret field data of relevance to the U.S. Army;
- c) although not implemented completely in this phase I study, the numerical model will allow us to optimize the NDE inspection process by determining optimal transducer configurations, aperture sizes, frequency settings, etc.

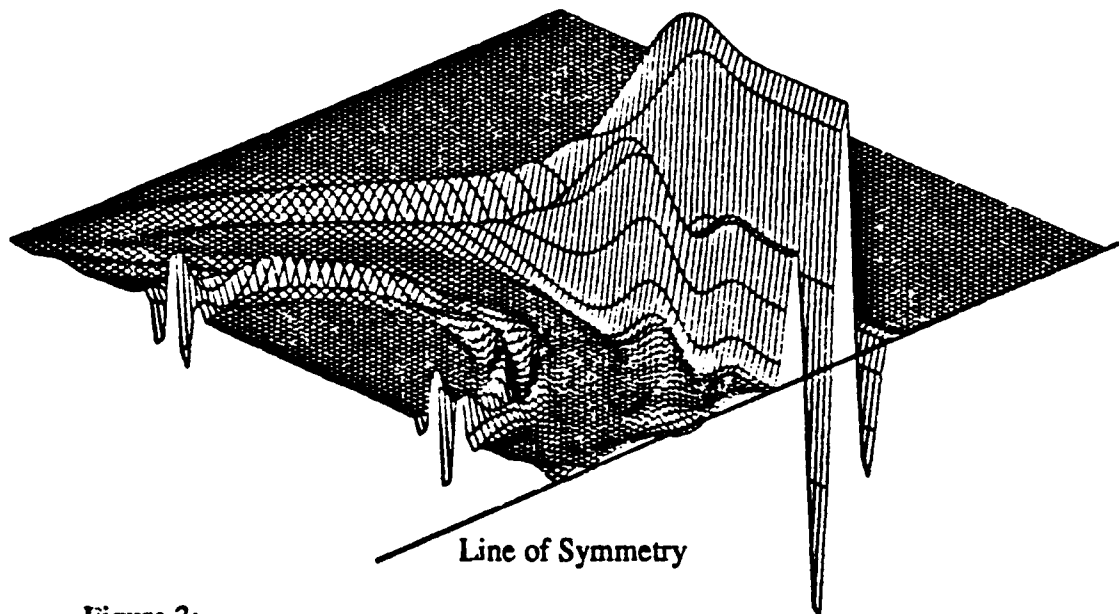


Figure 3:

U_z surface plot for plane strain with a 1/4 inch transducer, $f = 10 \text{ MHz}$ $t = 0.8 \text{ } \mu\text{s}$

Our numerical approach was closely coupled with the in-house experimental investigations at MTL. The simulated transient outputs (A-scans) were directly compared to the MTL measurements. The result section of this report shows the excellent agreement between the two investigation modes. Additionally, the numerical approach aided in the development of new or modified signal processing methods such as the Chirp-Z approach currently under investigation at MTL [12].

C.) Work Statement of Research

WPI in conjunction with MTL explored the ultrasound bondline NDE integrity from all three accepted modes of scientific endeavor - i.e. experimental, analytical, and numerical modes.

- **Experimental Investigations**

- a.) **MTL testing**

The dominant focus was in experimental measurement of samples at MTL. These bond samples underwent extensive analysis using longitudinal and horizontally polarized shear waves. The Chirp-Z transformation techniques were applied to enhance the obtained measurements. The experimental output was saved in multiple formats. The unfiltered transducer signals (A-scans) as well as hardware Chirp-Z transformed outputs were stored for all test configurations.

- b.) **Feature Analysis**

The rationale for this procedure was that a specimen prepared with a prescribed flaw or geometry exhibits a characteristic signal response as given by such features as frequency content, maximum amplitude, rise time, etc. [13]. We have tested experimentally and numerically multiple layer specimens with variety of thicknesses. These signatures are inputs to a neural net software system which is being trained to output discrete thickness values of the interface. The training is ongoing with encouraging results and is a dominant component of our phase II effort. The neural net program was obtained by MTL.

- **Mathematical Problem Formulation**

Based on the proposed multiple attack strategy the analytical formulations of the problem were thoroughly investigated as to their applicability for realistically modeling the physical process. Initial and boundary conditions were examined relative to their influence on the underlying equations. Approximations to the governing equations were derived and investigated.

- **Numerical Modeling**

A finite element model of the elastic wave equation was implemented on a mid-size computer (DecStation 5000 model 200). The code includes pre- and post processing options such as adaptive mesh generation and

graphics routines. The user identifies the physical properties of the various layers (density, wave velocities) and a desired resolution. The system automatically discretizes a domain with individualized nodal resolutions in each material. The successful two-dimensional modeling (x,y) was extended to account for full three-dimensional geometries (axisymmetric).

- **Verification**

The verification of our numerical investigations was two fold. Using prescribed test configurations our simulations were compared to existing analytical solutions yielding graphically indistinguishable results. Equally important, numerical simulations were compared to experimental field tests gathered at MTL. The result section shows that the numerical simulations reproduced that observed experimentally with fidelity.

D.) Summary

This work presents a concise overall approach to the analysis of bond-line integrity as measured via ultrasound NDE. Based on the previously outlined multiple attack strategy, a clear mathematical recipe was presented that describes the primary components of the coupled physical phenomenon of ultrasonic waves impinging on an adhesive interface. It is expected that this novel approach will increase the general comprehension of ultrasonic interfacial interaction for nondestructive testing purposes. Moreover, the numerical analysis approach was directly tested against analytical studies given certain simplifying constraints and against experimental results gathered at MTL. In each situation the simulated results predicted that observed in the analytical or experimental investigative mode with fidelity.

E.) References

- [1] Workshop on NDE of Adhesive Bond Strength, Orlando, Florida, April 13-14, 1988.
- [2] R. R. Teagle, "Recent Advances in Mechanical Impedance Analysis Instrumentation for the Evaluation of Adhesive Bonded and Composite Structures," 3rd European Conference on Nondestructive Testing, Florence, Italy, pp. 139-162, 1984.
- [3] E. Segel & J. Rose, "NDT Techniques for Adhesive Bond Joints," Res. Tech in NDT, V 4, 1980.

- [4] G. Alers, P. Flynn, and J. Buckley, "Ultrasonic Techniques for Measuring the Strength of Adhesive Bonds," *Materials Evaluation*, Vol. 35, No. 4, pp. 77-84, 1977.
- [5] J. Jones & J. Whittier, "Waves at a Flexibly Bonded Interface," *J of Ap Mech*, pp. 905-909, 1967.
- [6] Y. Bar-Cohen and A. Mal, "Ultrasonic NDE of Bonded Structures," *Workshop on NDE of Adhesive Bond Strength*, Orlando, FL, pp. 201-227, 1988.
- [7] B. Thompson and D. Thompson, "Past Experiences in the Development of Tests for Adhesive Bond Strength," *ibid*, pp. 24-75, 1988
- [8] R. Ludwig, D. Moore, W. Lord, "A Comparative Study of Analytical and Numerical Transient Force Excitations on an Elastic Half-Space, *IEEE Trans. on UFFC*, V 36, pp. 342-350, 1989.
- [9] R. Ludwig and W. Lord, "A Finite-Element Formulation for the Study of Ultrasonic NDT Systems," *IEEE Trans. on UFFC*, Vol. 35, No. 6, pp.809-820, 1989.
- [10] J. Achenbach, *Wave Propagation in Elastic Solids*, North-Holland, 1973.
- [11] B. Thompson and D. Thompson, "Past Experiences in the Development of Tests for Adhesive Bond Strength", *Workshop on NDE of Adhesive Bond Strength*, Orlando, FL, pp. 24-75, 1988.
- [12] O. Guericke, "Determination of the Geometry of Hidden Defects by Ultrasonic Pulse Analysis Testing," *J. Acoustical Soc. America*, Vol. 35, No. 3, pp. 364-368, 1963.
- [13] G. Weinfurter, K. Langenberg, and V. Schmitz, "Material Characterization with Ultrasound based on Features of Scattered Pulses," *German Soc. of NDT*, Kiel, Germany, 1989.
- [14] R. Duda, P. Hart, *Pattern Classification and Scene Analysis*, John Wiley, 1973.

F.) List of Articles Acknowledging this Project Support

- R. Ludwig, J.M. Sullivan, Jr. and R. Anastasi, "A Combined Theoretical and Experimental UNDE Investigation of Adhesively Bonded Metal-to-Metal Materials", 18th Rev Prog. QNDE , (1991).
- Nair, V.K., D. Dai, R. Ludwig and J.M. Sullivan, Jr., "Ultrasonic Signal Processing of Adhesive Bonding Data Employing Chirp-Z Transform and Adaptive Filtering Techniques", 18th Rev Prog in QNDE , (1991).
- Sullivan, J.M., Jr , R. Ludwig, R. Anastasi, and G. Charron, "Comparison of Adhesive Bond Thickness Measurements using Experimental and Numerical Ultrasonic NDE Systems", 10th Invitational Int. Symp. of UFEM, Unification of Finite Element Methods Through Parallelism in Analysis and Experimentation, July (1991).
- Sullivan, J.M., Jr., R. Ludwig, and Y. Geng, "Numerical Simulation of Ultrasound NDE for Adhesive Bond Integrity", *IEEE 1990 Ultrasonics Symposium*, IEEE Press, pp 1095-1098, (1991).
- Sullivan, J.M., Jr., R. Ludwig, Y. Geng, and V. Nair, "Numerical Comparison of Experimentally Measured Ultrasounds Through a Bonded Composite", *Rev Prog in QNDE , V10B*, Plenum Press (1991).

2 ELASTODYNAMIC WAVE PROPAGATION

2.1 Governing Equations

The governing equation is the balance of linear momentum (Cauchy's first law of motion) which in indicial notation can be expressed as

$$\sigma_{ij,j} + F_i = \rho \frac{\partial^2 u_i}{\partial t^2} \quad (2.1)$$

where σ_{ij} is the stress tensor, F_i is the body force vector, ρ is the density and u_i is the displacement vector. The Einstein summation convention is assumed where $i,j=1,2,3$ representing the three coordinate directions x, y and z respectively. $()_{,j}$ represents a spatial derivative with respect to the j direction.

In order to solve this equation for displacements it is necessary to express the stress tensor in terms of displacements. A Kelvin model constitutive relation is chosen to allow viscous damping.[15]

$$\sigma_{ij} = C_{ijkl} \epsilon_{kl} + D_{ijkl} \dot{\epsilon}_{kl} \quad (2.2)$$

where C_{ijkl} is the elastic constitutive matrix, D_{ijkl} is the damping constitutive matrix, ϵ_{kl} is the strain matrix and $\dot{\epsilon}_{kl}$ is the rate of strain tensor. A single dot above a variable signifies a first derivative with respect to time, two dots a second derivative. Choosing a Maxwell model, or a more complicated model for that matter, makes it difficult to solve for the stress directly. It is assumed that the strains are small and that the material behaves in a linear elastic manner. The strain-displacement and rate of strain-rate of displacement relations are as follows

$$\epsilon_M = \frac{1}{2} (u_{k,i} + u_{i,k}) \quad \dot{\epsilon}_M = \frac{1}{2} (\dot{u}_{k,i} + \dot{u}_{i,k}) \quad (2.3)$$

Substituting equations (2.3) into (2.2) yields

$$\sigma_y = C_{yM} \left(\frac{1}{2} (u_{k,i} + u_{i,k}) \right) + D_{yM} \left(\frac{1}{2} (\dot{u}_{k,i} + \dot{u}_{i,k}) \right) \quad (2.4)$$

which can be written as

$$\sigma_y = C_{yM} u_{k,i} + D_{yM} \dot{u}_{k,i} \quad (2.5)$$

by expanding equation (2.4) and swapping the dummy indices k and l in the second and fourth terms. Substituting equation (2.5) into equation (2.1) yields

$$C_{yM} u_{k,i} + D_{yM} \dot{u}_{k,i} + F_i = \rho \frac{\partial^2 u_i}{\partial t^2} \quad (2.6)$$

which is the elastodynamic wave equation expressed in terms of displacements. Note that the wave equation is a set of three coupled second order hyperbolic partial differential equations.

2.1 Wave Motion

The nature of the motion can be categorized into three types of waves; longitudinal, shear and surface. Longitudinal (or primary) waves are characterized by particle motion that is parallel to the direction of propagation. Shear (also called transverse or secondary) waves are characterized by motion that is perpendicular to the direction of propagation. Surface waves have motion with components in each direction but whose magnitude decreases exponentially away from the surface. Surface waves on a free surface are known as Rayleigh waves. Waves at solid-solid boundaries are referred to as Stonely waves.

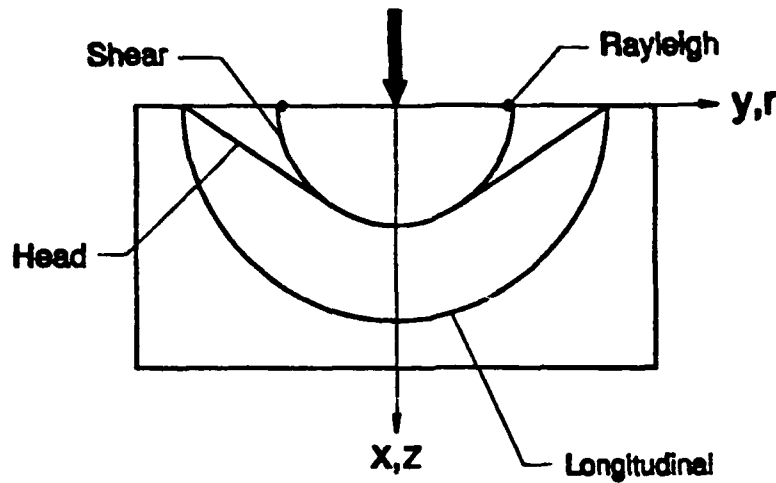


Figure 2.1: Wavefronts generated by a point or line source.

Figure (2.1) shows the wave propagation for a point force on an infinite half-space. All the waves propagate perpendicular to their wavefronts. The schematic only identifies wavefront positions; it does not reflect the wave amplitudes which may be zero at some points on the wavefront. The longitudinal wave travels with greatest speed which is expressed as: $C_p = \sqrt{\frac{\mu + \lambda}{\rho}}$ for an isotropic, linear, homogenous medium where, μ and λ are Lamé's constants and ρ is the material density. The shear wave speed is defined as $C_s = \sqrt{\frac{\mu}{\rho}}$. The Rayleigh wave has a velocity between 86.2 and 95.5 percent of the C_s , depending on Poisson's ratio. If the half-space is viewed from above, the Rayleigh wave has a linear wavefront for plane strain and a circular wavefront for axisymmetric. The head wave is a shear wave that is produced by the longitudinal wave at the free surface. The mode conversion is necessary to satisfy the stress free boundary condition.[16]

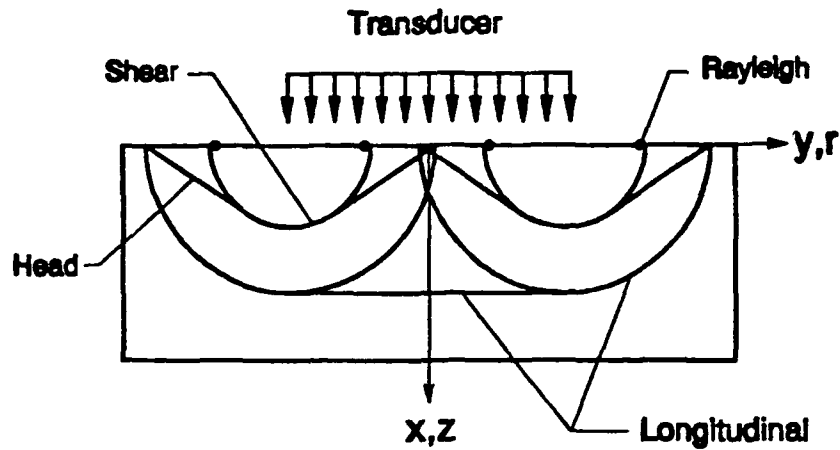


Figure 2.2: Expected wavefronts for finite width transducer.

Figure (2.2) shows the expected wavefronts for a finite width transducer. The applied force is spread uniformly over the transducer width. The discontinuity at the edge of the applied force produces wavefronts similar to those generated by a point force. The width of the transducer only contributes to the flat longitudinal wave.

3 FINITE ELEMENT FORMULATION

3.1 Numerical Formulation

Finite element solution techniques for partial differential equations are most commonly derived by variational principles or by the method of weighted residuals. Each method attempts to satisfy the differential equation by approximating the solution with a set of known functions multiplied by a set of arbitrary constants.

$$u_i = \sum_{M=1}^P U_M N_M \quad (3.1)$$

Where N_M are the known functions, or shape functions, and the unknown coefficients are the displacements U_M . The capitalized subscript M refers to the number of discrete points p used to approximate the solution [18].

The variational approach is based on minimizing a scalar functional derived from the original differential equation. When solving equilibrium problems of elasticity this functional represents the potential energy of the system. In the static case, the minimization produces an extremum of the functional guaranteeing convergence of the solution. However, applying the variational method to the elastodynamic wave equation produces only a stationary value not an extremum of the functional [10], therefore convergence is not guaranteed, which is to be expected considering the hyperbolic nature of the wave equation.

The weighted residual approach will be presented for its simpler mathematical nature, ie. knowledge of variational calculus is not required. The method of weighted residuals deals directly with the differential equations. Substituting the assumed solution for the exact

solution into equation (2.6), the differential equation will usually not be satisfied over the entire domain. The resulting error is known as the residual.

$$R_i = C_{ijk} U_{km} N_{m,j} + D_{ijk} \dot{U}_{km} N_{m,j} + F_i - \rho \ddot{U}_{im} N_m \neq 0 \quad (3.2)$$

The spatial derivative does not appear on the U_{km} , \dot{U}_{km} and \ddot{U}_{im} terms because they are spatial constants. This error is then forced to be zero on average over the domain by setting the volume integral of the product of a set of weighting functions W_L and the residual R_i equal to zero.

$$\int_V W_L [C_{ijk} U_{km} N_{m,j} + D_{ijk} \dot{U}_{km} N_{m,j} + F_i - \rho \ddot{U}_{im} N_m] dV = 0 \quad (3.3)$$

This formulation produces an independent equation for each degree of freedom. Although the equations can be solved at this point, Green's theorem of integration by parts is used on the first two terms of equation (3.3). This practice reduces the order of the derivative on the assumed solution, allowing simple linear shape functions to be used, and also expresses the boundary conditions explicitly.

$$\begin{aligned} & -\int_V W_L C_{ijk} U_{km} N_{m,j} dV - \int_V W_L D_{ijk} \dot{U}_{km} N_{m,j} dV \\ & + \int_S W_L C_{ijk} u_{k,j} n_j dS + \int_S W_L D_{ijk} \dot{u}_{k,j} n_j dS \\ & + \int_V W_L F_i dV - \int_V W_L \rho \ddot{U}_{im} N_m dV = 0 \end{aligned} \quad (3.4)$$

Note that the exact solution has been reinserted into the surface integrals and that n_j is the unit outward normal on the surface. By combining the surface integrals and substituting for the stress tensor using equation (2.2), it becomes obvious that they represent the surface tractions at the boundary.

$$\int_s W_L (C_{\theta\theta} u_{t,\theta} + D_{\theta\theta} \dot{u}_{t,\theta}) n_j dS = \int_s W_L \sigma_{\theta} n_j dS = \int_s W_L T_i dS \quad (3.5)$$

where T_i is the surface traction vector at the boundary. Equation (3.4) can be further simplified by moving the constant U_{LM} terms out of the integrals. According to the Galerkin method of weighted residuals setting the weighting functions equal to the shape functions yields

$$\begin{aligned} [\int_V N_L \rho N_M dV] \ddot{U}_{LM} + [\int_V N_L D_{\theta\theta} N_{M,\theta} dV] \dot{U}_{LM} \\ + [\int_V N_L C_{\theta\theta} N_{M,\theta} dV] U_{LM} = \int_V N_L F_i dV + \int_s N_L T_i dS \end{aligned} \quad (3.6)$$

Equation (3.6) is applicable to the entire domain. The equation is effectively discretized into finite elements by the appropriate choice of shape functions N_L .

3.2 Plain Strain and Axisymmetric Formulation

In order to avoid the complexities of a full three dimensional formulation, the simpler two dimensional plain strain and axisymmetric models are formulated. Advantages include reduced total degree of freedom models, simpler mesh generation, and ease of graphical presentation of results. The computational strategies developed in section 5 are not limited in any way to a two dimensional formulation and can be easily extended to a full three dimensional formulation.

The plain strain formulation models an object infinitely thick in the z coordinate direction. This eliminates normal strains in the z direction as well as shear strains in the x-z and y-z directions. The transducer is now modeled as an infinite strip and any voids become infinite tubes. The waves generated are cylindrical about the z axis. As the cylindrical waves expand the amplitude of the wave decreases because its energy is spread over a

larger area. This phenomenon is referred to as geometric dispersion. The actual geometric dispersion for a circular transducer is spherical and as a result A-scans from this formulation do not compare well with experimental data quantitatively.

The axisymmetric formulation models a body of revolution under axisymmetric loading conditions. This formulation models the physical transducer extremely well because the geometric dispersion is spherical. The formulation does not work well for voids that are off of the centerline which are modeled as circular rings. If the emphasis of the analysis is on the wave interaction between layered mediums the axisymmetric formulation is the most practical.

The fourth order tensors of equation (3.6) are difficult to deal with and can be reduced to second order tensors by index contraction [19]. For the plain strain case the C_{ijkl} and D_{ijkl} matrices become

$$C_{ijkl} = C_{ji} = \begin{bmatrix} c_{1111} & c_{1122} & c_{1112} \\ c_{1122} & c_{2222} & c_{2212} \\ c_{1112} & c_{2212} & c_{1212} \end{bmatrix} \quad D_{ijkl} = D_{ji} = \begin{bmatrix} d_{1111} & d_{1122} & d_{1112} \\ d_{1122} & d_{2222} & d_{2212} \\ d_{1112} & d_{2212} & d_{1212} \end{bmatrix} \quad (3.7)$$

An axis of symmetry may be chosen in an x' or y' direction if the stiffness and damping matrices transform such that $c'_{1112} = c'_{2212} = 0$ and $d'_{1112} = d'_{2212} = 0$. The shape function matrix is defined as

$$N_L = \begin{bmatrix} N_1 & 0 & N_2 & 0 & \dots & N_L & 0 \\ 0 & N_1 & 0 & N_2 & \dots & 0 & N_L \end{bmatrix} \quad (3.8)$$

The derivatives of the shape functions become assuming that the displacements have been contracted according to

$$N_{L,j} = \begin{bmatrix} \frac{\partial N_1}{\partial x} & 0 & \frac{\partial N_2}{\partial x} & 0 & \dots & \frac{\partial N_L}{\partial x} & 0 \\ 0 & \frac{\partial N_1}{\partial y} & 0 & \frac{\partial N_2}{\partial y} & \dots & 0 & \frac{\partial N_L}{\partial y} \\ \frac{\partial N_1}{\partial y} & \frac{\partial N_1}{\partial x} & \frac{\partial N_2}{\partial y} & \frac{\partial N_2}{\partial x} & \dots & \frac{\partial N_L}{\partial y} & \frac{\partial N_L}{\partial x} \end{bmatrix} \quad (3.9)$$

$$U_{uL} = U = [U_{11} \ U_{21} \ U_{12} \ U_{22} \ \dots \ U_{1L} \ U_{2L}]^T \quad (3.10)$$

where the first subscript is the direction and the second is the node number.

Equation (3.6) can now be cast in the more familiar form

$$[M]\ddot{U} + [D]\dot{U} + [K]U = F_b + F_s \quad (3.11)$$

with the following definitions.

$$\begin{aligned} [M] &= \int_A N_L \rho N_M dx dy & F_b &= \int_A N_L F_i dx dy \\ [D] &= \int_A N_{L,j} D_{ji} N_{M,i} dx dy & F_s &= \int_s N_L T_i dS \\ [K] &= \int_A N_{L,j} C_{ji} N_{M,i} dx dy \end{aligned} \quad (3.12)$$

where $[M]$ is the mass matrix, $[D]$ is the damping matrix, $[K]$ is the stiffness matrix, F_b are the nodal body forces and F_s are the nodal surface forces. The volume integrals have been reduced to area integrals due to the two dimensional formulation in which a unit depth in the z direction has been assumed.

For the axisymmetric formulation, N_L is the same and C_{ji} , D_{ji} and $N_{L,j}$ take the following forms.

$$C_{\theta\theta} = C_{\theta} = \begin{bmatrix} c_{1111} & c_{1122} & c_{1122} & 0 \\ c_{1122} & c_{2222} & c_{2233} & 0 \\ c_{1122} & c_{2233} & c_{2222} & 0 \\ 0 & 0 & 0 & c_{1212} \end{bmatrix} \quad D_{\theta\theta} = D_{\theta} = \begin{bmatrix} d_{1111} & d_{1122} & d_{1122} & 0 \\ d_{1122} & d_{2222} & d_{2233} & 0 \\ d_{1122} & d_{2233} & d_{2222} & 0 \\ 0 & 0 & 0 & d_{1212} \end{bmatrix} \quad (3.13)$$

$$N_{L,j} = \begin{bmatrix} \frac{\partial N_1}{\partial z} & 0 & \frac{\partial N_2}{\partial z} & 0 & \dots & \frac{\partial N_L}{\partial z} & 0 \\ 0 & \frac{\partial N_1}{\partial r} & 0 & \frac{\partial N_2}{\partial r} & \dots & 0 & \frac{\partial N_L}{\partial r} \\ \frac{N_1}{r} & 0 & \frac{N_2}{r} & 0 & \dots & \frac{N_L}{r} & 0 \\ \frac{\partial N_1}{\partial r} & \frac{\partial N_1}{\partial z} & \frac{\partial N_2}{\partial r} & \frac{\partial N_2}{\partial z} & \dots & \frac{\partial N_L}{\partial r} & \frac{\partial N_L}{\partial z} \end{bmatrix} \quad (3.14)$$

In order for an axisymmetric formulation to be valid, the material must be at least transversely isotropic with the material axis of symmetry parallel to the z axis [11]. The expressions presented for the [C] and [E] matrices have been appropriately reduced. Equation (3.11) is now defined by

$$\begin{aligned} [M] &= \int_A 2\pi r N_L \rho N_M dr dz & F_b &= \int_A 2\pi r N_L F_b dr dz \\ [D] &= \int_A 2\pi r N_L D_{\theta} N_M dr dz & F_s &= \int_s 2\pi r N_L T_i dS \\ [K] &= \int_A 2\pi r N_L C_{\theta} N_M dr dz \end{aligned} \quad (3.15)$$

The integrations in equations (3.12) and (3.15) can be calculated numerically using Gauss quadrature. The shape functions N_L for common element types and the procedure for Gauss quadrature can be found in many textbooks [20,21].

3.3 Time Integration

Equation (3.11) represents a system of linear second order differential equations in time. Numerical solution schemes are based on discretizing time into intervals and satisfying the system only at those time slices. Various schemes include the central difference method, the Newmark method, the Houbolt method and the Wilson- Θ method. The difference between these schemes is determined by how they estimate the displacements, velocities and accelerations within each time step [22]. Although these methods are commonly referred to as finite difference methods in time, Zienkiewicz has shown that they are equivalent to a finite element formulation using the weighted residual method applied to an interval $2\Delta t$ if the shape functions are chosen appropriately [23].

These methods fall into two groups, implicit and explicit. Explicit implies that the solution at time $t + \Delta t$ depends only on known values at previous time steps. Implicit implies that the solution at time $t + \Delta t$ depends on known values at previous time steps as well as values at the current time step. The main advantage of the explicit methods is that the system of equations is decoupled. The disadvantage is that small time steps are required for stability. Implicit schemes are stable for larger time steps but require a matrix to be either inverted or triangularized at the first time step. Due to the large size of the matrices involved, the explicit central difference method is employed.

Using the central difference method the acceleration term is estimated as

$$\ddot{U}^t = \frac{1}{(\Delta t)^2} [U^{t+\Delta t} - 2U^t + U^{t-\Delta t}] \quad (3.16)$$

assuming that Δt remains fixed. The velocity term was estimated using a backward difference to avoid a matrix inversion and maintain an explicit solution [23]

$$\dot{U}^t = \frac{1}{\Delta t} [U^t - U^{t-\Delta t}] \quad (3.17)$$

Substituting for \ddot{U}^t and \dot{U}^t using equations (3.16) and (3.17) into equation (3.11) and solving for $U^{t+\Delta t}$, yields the following fully explicit equation neglecting body forces.

$$U^{t+\Delta t} = \Delta t [M]^{-1} \{ \Delta t (F_s^t - [K]U^t) + [D](U^{t-\Delta t} - U^t) \} + 2U^t - U^{t-\Delta t} \quad (3.18)$$

3.4 Mass Matrix Diagonalization

The mass matrix resulting from the integration defined in (3.12) and (3.15) is called the consistent mass matrix. It can be evaluated using Gauss quadrature numerical integration. However, to maintain an explicit solution the mass matrix is diagonalized. The mass matrix can be diagonalized without a significant loss of accuracy by using the following formula on an elemental basis [24].

$$M_u^d = \frac{M_u^c}{\sum_{j=1}^P M_u^c} \sum_{j=1}^P \sum_{k=1}^P M_{jk}^c \quad (3.19)$$

where the superscripts d and c stand for diagonal and consistent matrices respectively. Alternatively the diagonalized mass matrix can be evaluated directly by moving the Gauss quadrature points to the node points. This approach works well with the plane strain formulation but fails for the axisymmetric case when the element is on the centerline ($r = 0$). After diagonalization, the matrix inversion is reduced to inverting each diagonal component individually. If a central difference formula is used to estimate the velocity, solving for $U^{t+\Delta t}$ would require the sum of $[M]$ and $[D]$, which would no longer be diagonal, to be inverted. The $[D]$ matrix can not be diagonalized because the sum of the components will always equal zero.

3.5 Stability Constraints

The disadvantage of the explicit method is that it is only conditionally stable. The constraint governing the stability is known as the Courant constraint.

$$Courant = q = C_{\max} \frac{\Delta t}{\Delta x_{\min}} \leq 1.0 \quad (3.20)$$

Where C_{\max} is the longitudinal wave velocity C_l of the material of that element and Δx_{\min} is the length of the shortest edge for a rectangular four noded element. For a three noded triangular element or a four noded parallelogram, Δx_{\min} will be the shortest distance from any node to a non-adjacent side. Every element must satisfy equation (3.20) for the solution to be stable. In the explicit method information flows across one element per time step. Therefore the minimum rate at which information flows is the minimum Δx divided by the time step Δt . If that rate is slower than C_{\max} the numerical solution can not approximate the actual wave motion and the solution will diverge, which is the constraint of equation (3.20). [26]

3.6 Initial Conditions

The initial conditions needed to start equation (3.18) are the full displacement vectors at $t = -\Delta t$ and $t = 0$. The first displacements calculated are for $t = \Delta t$. Alternatively, if the acceleration, velocity and displacement vectors are known at $t = 0$ a Taylor series expansion can be used to approximate the displacement at $t = \Delta t$.

$$U^{\Delta t} = U^0 + \Delta t \dot{U}^0 + \frac{1}{2}(\Delta t)^2 \ddot{U}^0 \quad (3.21)$$

If only the initial velocity and displacement vectors are known a backwards Taylor series

expansion can be used to find the displacements at $t = -\Delta t$ as follows [11].

$$U^{-\Delta t} = U^0 - \Delta t V^{-\Delta t} \quad (3.22)$$

Equation (3.18) can then be used at subsequent time steps. Although non-zero initial conditions are acceptable, it is assumed that the medium is initially at rest with no internal stresses. The initial conditions then become $U^{-\Delta t} = 0$ and $U^0 = 0$. If a forcing function is applied that is zero at $t = 0$ the solution of equation (3.18) at $t = \Delta t$ will not produce any displacements and can be avoided by substituting $F^{t+\Delta t}$ for F^t in equation (3.18) and increasing the total time at each time step by Δt and setting the response at $t = \Delta t$ equal to zero.

4 COMPUTATIONAL CONSIDERATIONS

Upon first inspection, it would seem that implementing the finite element solution could be done in a similar manner to the simple static case. However, it becomes apparent quickly that there are several problems. The extremely short wavelengths of the ultrasonic waves force the finite element mesh to become extremely dense. Due to the large number of degrees of freedom of the dense mesh, the memory required to store the matrices is excessive. The difficulty is compounded by the requirement of a time step size that is proportional to the element spacing through the Courant constraint. The number of time steps necessary to complete an analysis quickly grows into the thousands. Consequently execution times can easily stretch into months. This section presents a computer implementation strategy that avoids these pitfalls, creating a useful tool for the investigation of ultrasonic phenomena.

4.1 Memory Storage

For large meshes the memory required to store the stiffness and damping matrices quickly becomes prohibitive because their size is of the order of the number of degrees of freedom squared. For example, if the mesh has 1,000,000 degrees of freedom, the full stiffness matrix will need 4,000 gigabytes of memory using single precision. For a banded matrix solver, assuming a 500 by 1000 node mesh, the memory reduces to 8 gigabytes. However using a sparse matrix solver only requires the storage of the non-zero values, reducing the memory to 72 megabytes for the stiffness matrix. The damping matrix is of equal size increasing the total to 144 megabytes. Although this amount could be handled, it requires the cpu to swap memory back and forth from secondary storage

which is extremely inefficient and time consuming. An alternative method for storing those matrices is pursued.

One of the advantages of using the explicit formulation is that the global matrices are not assembled. Bathe and Wilson [22] suggest that the displacements can be computed using an element by element approach. Displacements are multiplied by the elemental matrices and the contributions are assembled in the new displacement vector. Further savings can be achieved if only the unique elemental matrices are saved. Although the element by element strategy reduces the memory required to the absolute minimum it creates redundant operations. Assuming a rectangular linear mesh, each node will be visited by four elements. There are eight multiplications for each degree of freedom per element visit or 64 total multiplications per node. The assembled matrix multiplication is completed by eighteen multiplications per degree of freedom resulting in a total of 36 multiplications per node. For uniformly meshed linear triangular elements, there are 72 multiplications for the element by element approach and only 28 for the assembled matrix. For a 3-dimensional, 8 noded brick formulation there are 576 multiplications for the element by element and 243 for the assembled matrix.

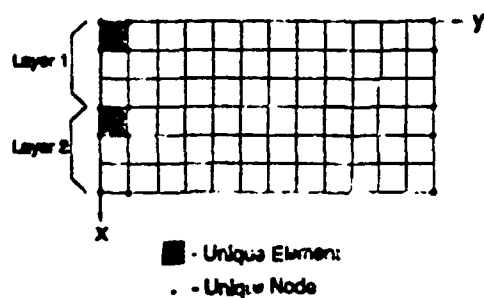


Figure 4.1: Plane strain unique node and element locations.

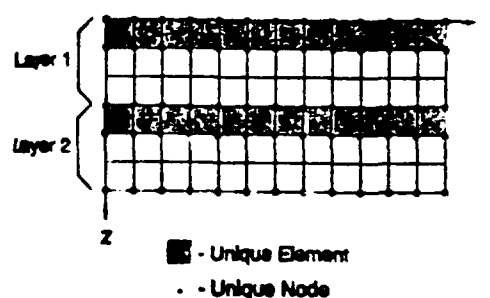


Figure 4.2: Axisymmetric unique node and element locations.

This redundancy can be eliminated by identifying and storing unique rows of the assembled matrices. A node by node approach can then be utilized to reduce the number

of operations to the minimum. A unique node location is determined by the properties of the surrounding elements and by their relative positions. For simple layered geometries, with homogeneous material properties within each layer, an a priori method of determining the unique nodal locations is shown in Figures (4.1) and (4.2) for the plain strain and axisymmetric configurations, respectively. The number of unique nodes for the layered model can be calculated using the following formulas.

$$\begin{aligned} \text{Number of unique nodes} &= 6(NL) + 3 && \text{(Plane Strain)} \\ \text{Number of unique nodes} &= 2(NL + 1)(NR) && \text{(Axisymmetric)} \end{aligned} \quad (4.1)$$

Where NL is the number of layers and NR is the number of nodes in the r direction. The plane strain formula is independent of the number of nodes in the x or y directions. The axisymmetric formula is independent of the number of nodes in the z direction but dependent on the number of nodes in the r direction. The memory required to store the stiffness and damping matrices for a 500 by 1000 node, three layered model is reduced from 144 Mbytes to 12 kbytes for plane strain and 2.3 Mbytes for axisymmetric. Each unique node is given an integer flag to associate it with its unique row. The remaining non-unique nodes are assigned the flag number for the appropriate corresponding unique node. The mass matrix can be stored in the same fashion because the unique nodes in Figures (4.1) and (4.2) are also unique mass nodes.

The local stiffness matrices are only calculated at the unique element locations shown in Figures (4.1) and (4.2). The unique elements are flagged in a similar manner as the unique nodes. Row assemblage is accomplished by visiting each unique node, calculating the unique element flags for the four surrounding elements and assembling the appropriate values from the local stiffness matrices into the unique rows, one for each degree of freedom. The process is exactly the same as in conventional finite element methods except that only two rows of the assembled matrix are saved.

The node by node form of equation (3.18) can be written as follows.

$$U_{iM}^{t+\Delta t} = \Delta t [M]_{diagonal}^{-1} \left\{ \Delta t (F_s^t - [K]_{row} \bar{U}^t) + [D]_{row} (\bar{U}^{t-\Delta t} - \bar{U}^t) \right\} + 2U_{iM}^t - U_{iM}^{t-\Delta t} \quad (4.2)$$

The bar over the displacements indicates a vector quantity and $[]_{row}$ indicates the appropriate row of the matrix. $[]_{diagonal}$ indicates only the diagonal component of the appropriate row, making $[M]_{diagonal}$ a scalar quantity.

4.2 Solver Efficiency

The bulk of the time used by the solver can be attributed to two processes. The first is the actual solution to the differential equation. The second is the determination of the element connectivity necessary to place local node contributions in the correct global locations. To develop the most efficient solver possible both of these processes are streamlined.

Equation Reduction

The first step in minimization of the actual solution factors equation (4.2) for the displacements. The resulting coefficients are constant and are premultiplied to avoid repeating the same multiplications every time step. The factored equation becomes

$$U_{iM}^{t+\Delta t} = F_s' + [K]_{row}' \bar{U}^t + [K]_{row}'' \bar{U}^{t-\Delta t} \quad (4.3)$$

with the following definitions.

$$\begin{aligned} F_s' &= \Delta t^2 [M]_{diagonal}^{-1} F_s^t \\ [K]_{row}' &= -\Delta t^2 [M]_{diagonal}^{-1} [K]_{row} - \Delta t [M]_{diagonal}^{-1} [D]_{row} + 2[I]_{row} \\ [K]_{row}'' &= \Delta t [M]_{diagonal}^{-1} [D]_{row} - [I]_{row} \end{aligned} \quad (4.4)$$

where $[I]$ is the identity matrix. If damping is not included, equation (4.3) becomes

$$U_{UM}^{t+\Delta t} = F_s' + [K]_{row}' \bar{U}^t - U_{UM}^{t+\Delta t} \quad (4.5)$$

with the following definitions.

$$\begin{aligned} F_s' &= \Delta t^2 [M]_{diagonal}^{-1} F_s^t \\ [K]_{row}' &= -\Delta t^2 [M]_{diagonal}^{-1} [K]_{row} + 2[I]_{row} \end{aligned} \quad (4.6)$$

Note that the $U^{t+\Delta t}$ term is no longer a vector quantity in equation (4.5).

Automatic Connectivity

The time expended on the element connectivity can be minimized if the mesh is restricted so that the connectivity is determined algebraically. The restriction simply requires the connectivity to be equivalent to a rectangular grid with regular node numbering. It is important to note that the nodal coordinates are not restricted as long as gaps or overlaps are not created. Voids can be modeled by giving a rectangular section of elements zero local stiffness matrices and skipping the displacement solution at nodes that lie completely within that area. The connectivity is then calculated using the row and column of the element. However, if the node numbers are determined solely by the row and column numbers the node numbers themselves do not produce any new information. The impetus for global node numbering is to represent the assembled matrices as two dimensional arrays that can be inverted using stock solvers. Since the matrices are not inverted, nodes can be labeled using the row and column numbers by increasing the dimensionality of the arrays

$$\bar{U} = U(k, i, j) \quad (4.7)$$

Where k is the displacement direction ($1 = x, z$, $2 = y, r$), i is the row number and j is the column number. This eliminates the operations necessary to convert to global node

numbers. The connectivity is then easily calculated as the following.

$$\begin{aligned} \bar{U}_{connectivity} = [& U(k,i-1,j-1) , U(k,i-1,j) , U(k,i-1,j+1) , \\ & U(k,i,j-1) , U(k,i,j) , U(k,i,j+1) , \\ & U(k,i+1,j-1) , U(k,i+1,j) , U(k,i+1,j+1)]^T \end{aligned} \quad (4.8)$$

Where each term is repeated twice, first for $k = 1$ and second for $k = 2$ (see equation (3.10)). The elements are also numbered using row and column numbers when the unique stiffness and damping rows are determined before the first time step. After that the element numbers are no longer needed using the node by node solution.

Row-Column Multiplication

To facilitate the row-column multiplications in equation (4.3), the unique rows are separated into two (3x3) arrays. One array are for the values that are multiplied by displacements in the x,z direction and the second are for the values multiplied by the displacements in the y,r direction. Equation (4.3) becomes

$$U_{UM}^{t+\Delta t} = F_s' + [K]_{row,1}' \bar{U}_1^t + [K]_{row,2}' \bar{U}_2^t + [K]_{row,1}'' \bar{U}_1^{t-\Delta t} + [K]_{row,2}'' \bar{U}_2^{t-\Delta t} \quad (4.9)$$

The primed stiffness rows in equation (4.9) are stored as $[K]_{row,k}' = UNK(k,l,m,n)$ and $[K]_{row,k}'' = UND(k,l,m,n)$ where k indicates the displacement direction, l and m are the (3x3) array indices and n is the unique row number. The (3x3) arrays are arranged to correspond to the node connectivity which is also defined by a (3x3) array (equation (4.8)). The row-column multiplication can then be accomplished by multiplying values in the same array positions and adding the result.

Boundary Conditions

Dirichlet type boundary conditions can be applied simply by setting the nodal displacement at time $t + \Delta t$ equal to the specified displacement. This can be done after the solution at the node is calculated or if it is more efficient the solution at the node can be skipped. If the Dirichlet boundary conditions are not functions of time, the displacement vectors can be initialized with the prescribed values and the solver can ignore those nodes. The boundary conditions are then implicitly applied at every time step. For the layered medium model, Dirichlet boundary conditions are applied only at the nodes along the axis of symmetry which are restricted from moving in the y, r direction.

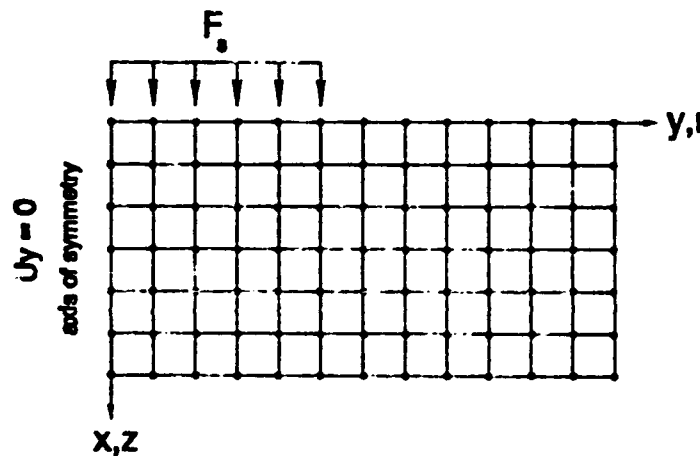


Figure 4.3: Boundary conditions for half symmetry model.

Neumann type boundary conditions can be applied at the specified nodes by including the F_z term in equation (4.3). The force term appears only at the nodes on the top surface under the transducer. This reduces the amount of memory required to store the F_z array and eliminates unnecessary computations. The remaining regions are traction free boundaries, see Figure (4.3). It is interesting to point out that free body motion is not restricted in the x, z direction. This does not cause a problem because the stiffness matrix is not inverted. If the forcing function has a non-zero net force, the mesh will eventually gain a net velocity in the same direction. The displacements will then continue to grow

in time. If the forcing function has a zero net force the displacements will remain centered about the initial mesh location.

Solution Regions

As the solver moves from node to node it needs to recognize whether the node is on an edge, on a corner or in the interior. It also needs to know if boundary conditions are being applied at that node. As the solver visits each node it determines the unique flag, performs the row-column multiplications and completes equation (4.3) or (4.5) by adding the remaining scalar quantities. To accomplish this as efficiently as possible, the nodes are divided into regions where the solution is performed separately. After a number of iterations the solver changes to a different sectional configuration.

The initial solver has five sections as shown in Figure (4.4). Section 1 contains only the corner node on the top surface on the axis of symmetry. Section 2 contains the nodes on the top surface under the transducer. Section 3 contains the nodes on the top surface not under the transducer. Section 4 contains the node on the axis of symmetry. Section 5 contains the interior nodes, right boundary nodes and the bottom surface nodes. The Neumann type boundary conditions are applied in sections 1 and 2. The Dirichlet boundary conditions are applied in section 4. The row-column multiplications are reduced in sections 1 through 4 because the connectivity is lowered from 9 to 6 for the edge sections and from 9 to 4 for the corner node.

The secondary solver also has five sections (Figure 4.5). Section 1

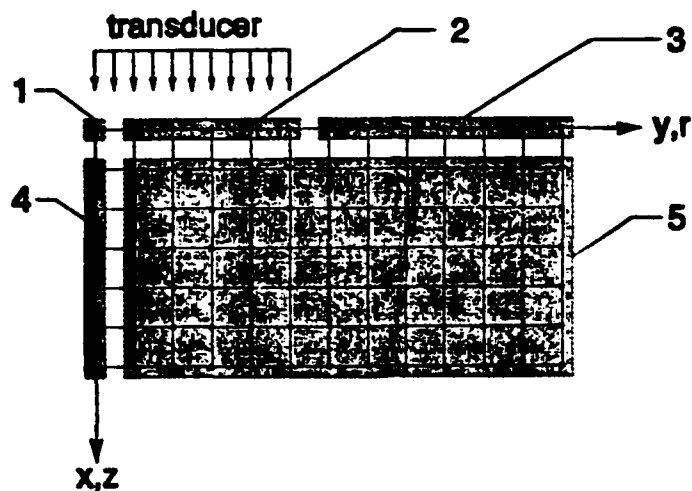


Figure 4.4: Initial solver solution regions.

contains the nodes on the top surface excluding the corner nodes. Section 2 contains the nodes along the axis of symmetry. Section three contains all of the interior nodes. Sections 4 and 5 contain the right hand side boundary nodes and the bottom surface nodes respectively. Similarly row-column multiplications are reduced in sections 1,2,4 and 5.

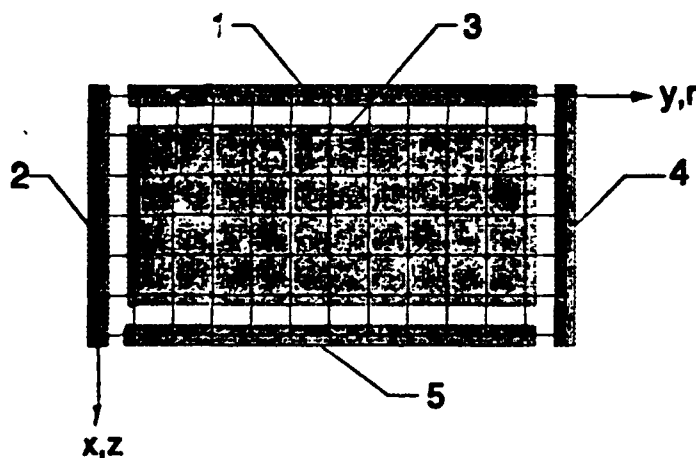


Figure 4.5: Secondary solver solution regions.

When computing the solution in section 5 of the first solver and in section 3 of the second solver, the order in which the solver proceeds from node to node greatly affects the execution time for the axisymmetric formulation. The sweep should be carried out by starting at the upper left-hand node and moving down the column and then advancing

one column to the right. This sweep pattern is more efficient because the unique node number does not change in a single layer as the solution proceeds down the column. This is faster because the pointer to the stiffness and damping arrays is not recalculated for each node. If a horizontal sweep is used cpu time is increased by 30 percent.

Expanding Solution Domain

At each time step information travels across one element. For the nodes that have not been reached yet, the solution of equation (4.3) consists of 72 zero multiplications and 72 zero additions because the displacement vectors will contain all zero entries. Obviously no new information is gained by carrying out the solution at those nodes. Therefore the solution will be extremely inefficient at early time steps when a majority of the nodes fall into this group.

Expanding the solution domain at the same rate as the flow of information eliminates the unnecessary calculations. The initial domain consists of the nodes under the transducer (section 1 and 2 in the initial solver) and expands by one row and one column with each time step until it reaches the boundary. Figure (4.6) shows an example of how the solution domain advances.

The advantage of using the expanding solution

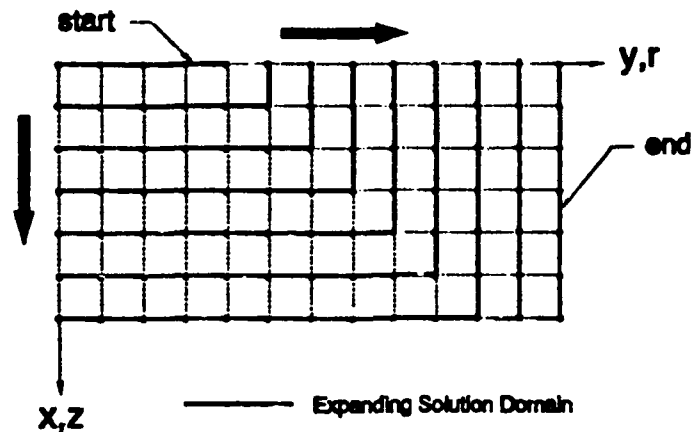


Figure 4.6: Example of expanding solution domain procedure. domain is most pronounced when the total time of the analysis is short. As the number of iterations beyond the time when the solution covers the entire domain increases, the realized time savings become a smaller percentage of the total execution time. It is extremely helpful when debugging changes to the program because of the quick initial response.

Solver Switching

The switch from the first solver to the second solver is determined by either the number of iterations necessary to complete the solution domain expansion or the number of iterations over which the forcing function F_r is applied. The greater of the two determines the iteration at which the switch is made. If the expansion is the determining factor, the forcing function will be set to zero after it is complete. If the opposite is true, the expansion will stop when the outer boundaries have been reached. The solver will not distinguish between the interior nodes and outer nodes when sections 3, 4 and 5 reach the edge of the domain and will assume a connectivity of six, six and nine respectively. The displacement vectors are dimensioned to include one extra row and one extra column of 'imaginary' nodes on the right-hand and bottom sides. The solution is unaffected

because the corresponding stiffness matrix components will be zero and solutions are never calculated at those nodes.

Displacement Vector Rotation

The solution of equation (4.3) requires three separate displacement vectors to be stored simultaneously, namely $U0 = \bar{U}^{t-\Delta t}$, $U1 = \bar{U}^t$ and $U2 = \bar{U}^{t+\Delta t}$. As the time step advances the $\bar{U}^{t+\Delta t}$ vector becomes \bar{U}^t and \bar{U}^t becomes $\bar{U}^{t-\Delta t}$. Therefore at the end of every time step $U0$ must be set equal to $U1$ and then $U1$ must be set equal to $U2$. The solution is then repeated solving for the new $U2$. In order to avoid this operation, the solver is repeated three times in succession. In the first section $U0 = \bar{U}^{t-\Delta t}$, $U1 = \bar{U}^t$ and $U2 = \bar{U}^{t+\Delta t}$. In the second section $U0 = \bar{U}^{t+\Delta t}$, $U1 = \bar{U}^{t-\Delta t}$ and $U2 = \bar{U}^t$. The third section completes the cycle with $U0 = \bar{U}^t$, $U1 = \bar{U}^{t+\Delta t}$ and $U2 = \bar{U}^{t-\Delta t}$. This process shifts the displacement vectors back implicitly.

If damping is neglected and equation (4.5) is used, only two displacement vectors need to be stored. The $\bar{U}^{t+\Delta t}$ displacement vector can be calculated directly into the $\bar{U}^{t-\Delta t}$ because of the one to one correspondence in equation (4.5). In this case the solver is only split into two sections. In the first section $U1 = \bar{U}^t$ and $U0 = \bar{U}^{t-\Delta t}$ to start with $U0$ becoming $\bar{U}^{t+\Delta t}$ as the solution proceeds from node to node. The second section has $U0 = \bar{U}^t$ and $U1 = \bar{U}^{t-\Delta t}$ with $U1$ becoming $\bar{U}^{t+\Delta t}$ to complete the cycle. For simple models where the number of unique nodes is small, the displacement vectors become the limiting memory requirement. For the 500 by 1000 node model, each displacement vector takes 4 Mbytes of memory. By rolling $\bar{U}^{t+\Delta t}$ into $\bar{U}^{t-\Delta t}$ the total memory required is reduced by nearly 33 percent.

5 FINITE ELEMENT CODE VERIFICATION

5.1 Convergence

Several factors influence solution convergence. The stability of the time integration, as discussed previously in section 4.3, requires the Courant number to be less than or equal to one. However, the solution will not converge for $q = 1.0$. The numerical integration of the stiffness matrices, time integration methods, computer round-off errors and dispersive effects are possible causes of solution divergence. The inability of the model to represent the forcing function either in time or space will not affect solution convergence. The solution will, however, not produce the correct displacements. The mass matrices are not a source of error because they are exactly integrated by a four point Gauss quadrature.

Stiffness Matrix Numerical Integration

The numerical integration of the stiffness matrix for the plane strain case is exact for 4 point quadrature. Increasing the order of integration will not increase the accuracy of the solution. Single point integration is not acceptable because it allows certain combinations of displacements to exist in the absence of nodal forces. The axisymmetric formulation of the stiffness matrix involves a r^{-1} term which can not be exactly integrated using Gauss quadrature. However, for the axisymmetric case increasing the order of numerical integration to 9 and 16 point quadratures had no appreciable effect on solution convergence or wave velocity. One reason for this is that the wave propagations investigated were all axial in nature. The axial waves are driven by the terms in the stiffness matrix that do not contain the r^{-1} term and are integrated exactly by the 4 point quadrature. For a complete study, radial wave propagation properties must be investigated.

Time Integration

The central difference approximation of equation (3.16) does not produce any instabilities as long as the Courant constraint is satisfied. The backwards difference approximation in equation (3.17), however, does introduce an instability proportional to the magnitude of the components of the damping matrix. The addition of viscous damping usually increases the stability of a numerical solution by damping out spurious modes. With the backward difference formula the velocity at time t is estimated as the velocity at $t - \frac{\Delta t}{2}$ which can cause the viscous force to be larger than the sum of the other forces acting on the node causing the solution to diverge [25]. Decreasing the Courant constraint will decrease the time step and reduce the effect of the error of the backward difference approximation. If the velocity was approximated with a central difference formula the viscous damping would indeed increase the stability of the solution.

Computer Round-off Error

The code was written in both single precision (8 digits) and double precision (16 digits). The solution convergence was not affected by the increase in accuracy of the double precision representation. Divergent solutions showed exactly the same A-scan for single precision as for double precision. Double precision is only necessary to retain accuracy during matrix inversions. Because there are no matrix inversions in the formulation single precision accuracy is acceptable. However, because single precision is more sensitive to underflow conditions, i.e. when numbers become smaller than can be represented by the computer, equations (4.3) and (4.5) must be modified. Factoring out the Δt^2 term from $[K]_{row}'$ and $[K]_{row}''$ will minimize the number of underflow checks. The main advantage of using single precision is a 25 percent increase in processing speed.

Spatial and Temporal Discretization

The degree of spatial and temporal discretization is determined by the frequency of the forcing function. For sinusoidal input, the degree of spatial discretization is defined by the number of nodes per wavelength, $n_x = \frac{\lambda}{\Delta x}$. The degree of temporal discretization is defined by the number of time steps per period, $n_t = \frac{T}{\Delta t}$. The degrees of discretization are not independent due to the Courant stability constraint. Substituting n_x and n_t into equation (3.20) yields the following relation

$$n_x = q n_t \quad (5.1)$$

which guarantees that the temporal discretization will always be greater than the spatial discretization. The forcing function is a raised cosine function given by

$$F_x = [1 - \cos(\frac{\omega t}{3})] \cos(\omega t) \quad 0 \leq t \leq \frac{6\pi}{\omega} \quad (5.2)$$

which has a Gaussian frequency distribution centered at ω , see Figure (5.1). Figures (5.2-4) compare displacement results for three different values of n_x for the initial wave, the first reflection and the second reflection, respectively. Note how the error for $n_x = 4$ does not increase as it propagates. Depending on the degree of accuracy required, an n_x in the range of 6 to 10 is suggested. The numerical model used is explained in the next section.

5.2 Dispersion

Dispersion is the variation of wave velocity with frequency. If the forcing function has a broad band frequency content, dispersion will cause the wave to change shape as it propagates. An isotropic, homogeneous, lossless material is non-dispersive. Numerical solutions will often introduce an artificial dispersion creating an error in the solution.

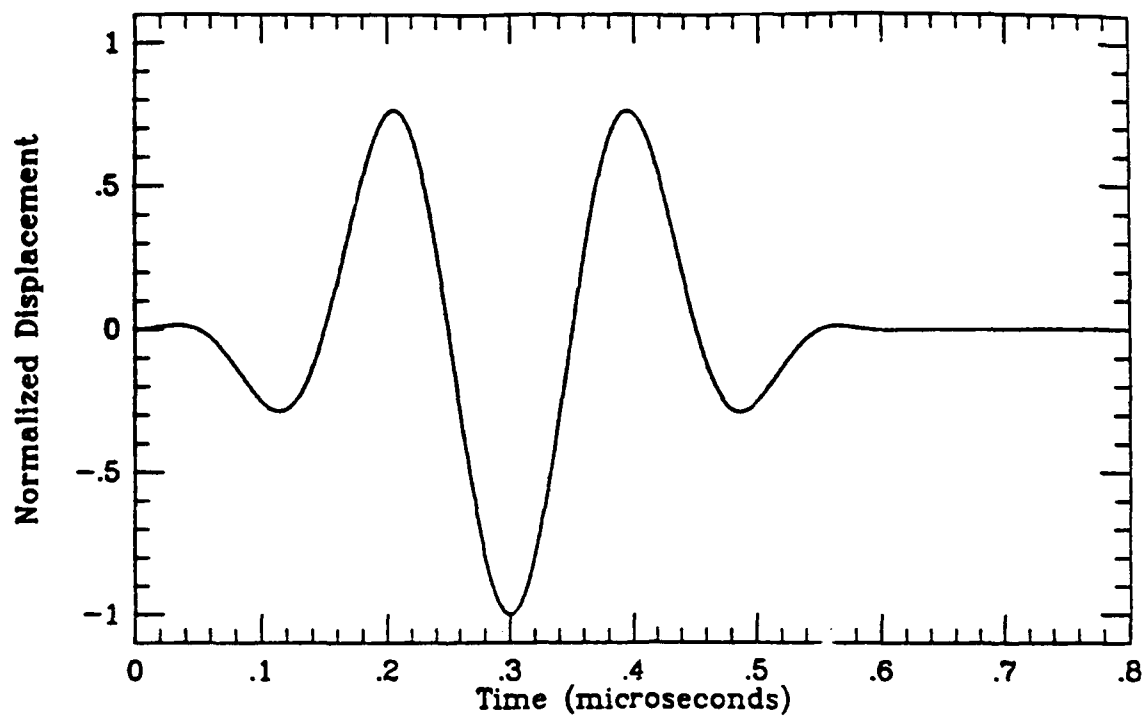


Figure 5.1: Raised cosine forcing function

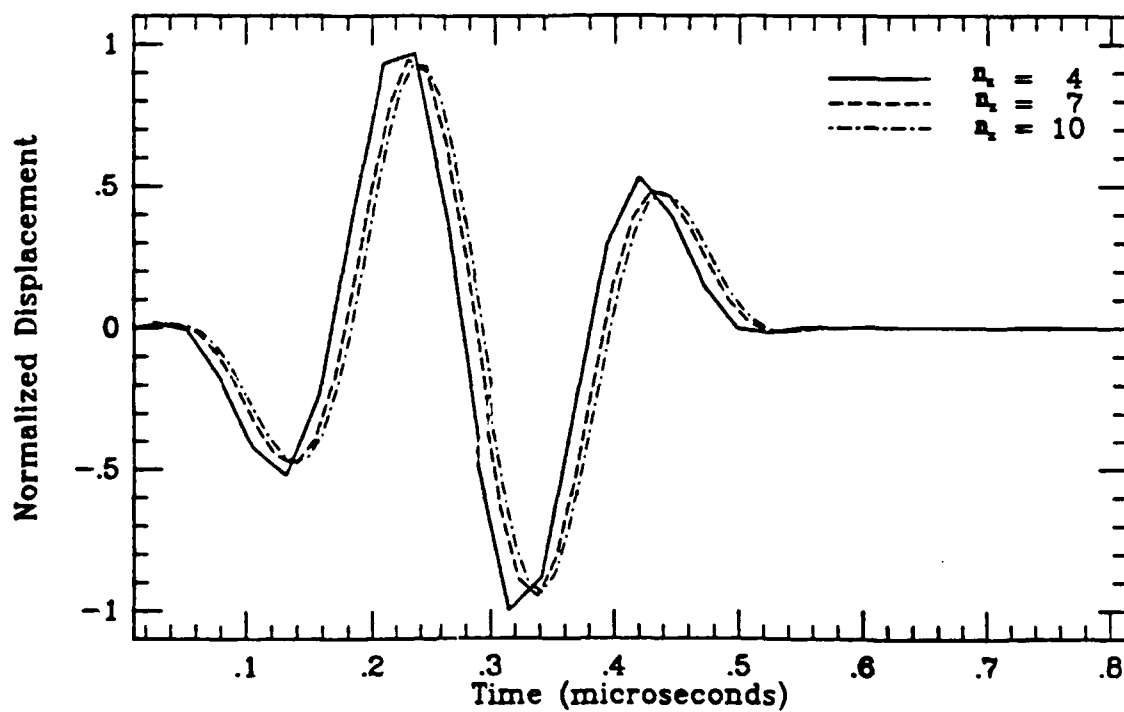


Figure 5.2: Initial waveform for $n_t = 4, 7$ and 10

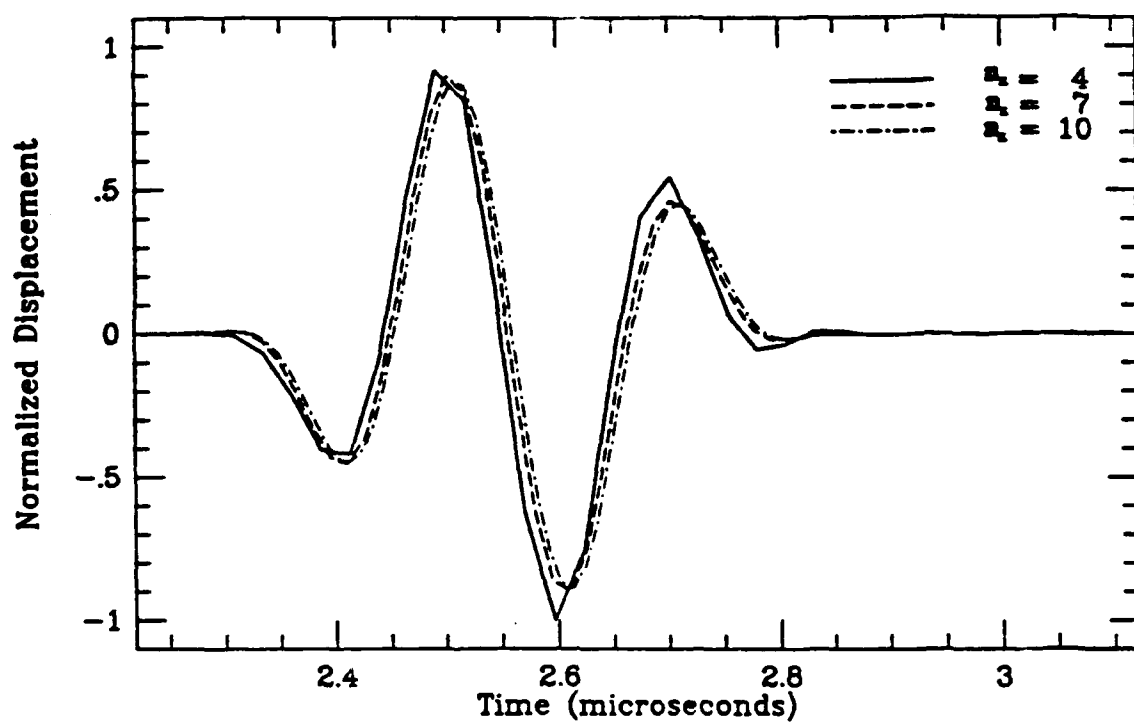


Figure 5.3: First reflection waveform for $n_t = 4, 7$ and 10

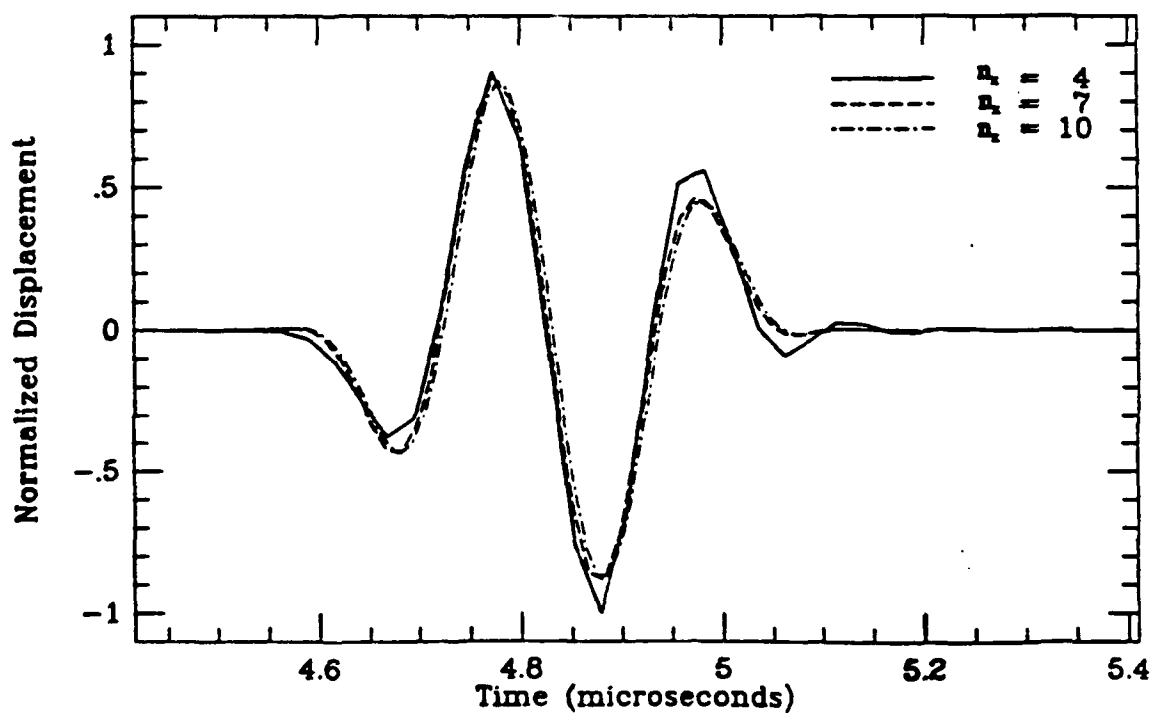


Figure 5.4: Second reflection waveform for $n_t = 4, 7$ and 10

The numerical solution of equation (2.1) employs both spatial and temporal discretizations. Each of the approximations causes dispersion. As shown by Krieg and Key [27] and Belytschko and Mullen [28,29], choosing the appropriate combination of mass matrix and time integration can minimize the artificial dispersion. The combination of lumped mass matrix and central difference time integration for $q = 1.0$ is a completely nondispersive solution along element edges. The lumped mass matrix decreases the phase velocity as frequency increases and the central difference integration increases the phase velocity as frequency increases. As q is reduced the dispersive effect of the central difference integration is reduced which shifts the net dispersive curve towards the lumped mass dispersive curve. Because the dispersion is dependent on the element size through the Courant constraint, a mesh with nonuniform elements in the same material will have nonuniform dispersive properties. For models containing more than one material, the spatial discretization n_x must be the same in each material for uniform dispersive properties.

Although a completely nondispersive solution is desirable, it is not possible because the solution diverges if extremely high frequencies are not attenuated. In fact, for the undamped case, solution convergence is completely determined by the combination of the highest unattenuated frequencies and the lowest natural frequency at a node.

A special model is created to reveal the effect of dispersion on the solution. Starting with the same model as shown in Figure (4.3) the boundary conditions on the right-hand side are changed to model another axis of symmetry, see Figure (5.5). The forcing function is applied to the entire top surface with a uniform distribution. The raised cosine signal imparts a zero net force on the model and approximates the actual wave pulse generated by a piezoelectric transducer [30]. The model then becomes one dimensional, which eliminates any geometric dispersion. Figures (5.6-8) show how the artificial dispersion affects the wave shape as it bounces back and forth. When q is close to 1.0 the solution is nearly non-dispersive as predicted [29]; as the q is lowered the dispersive effect is increased. With decreasing q , the solution converges to the dispersive

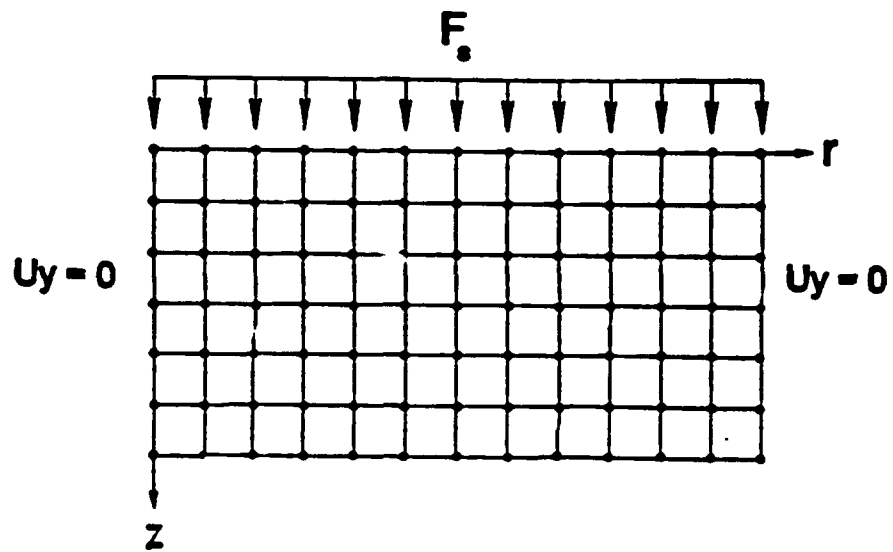


Figure 5.5: Boundary Conditions for dispersion test.

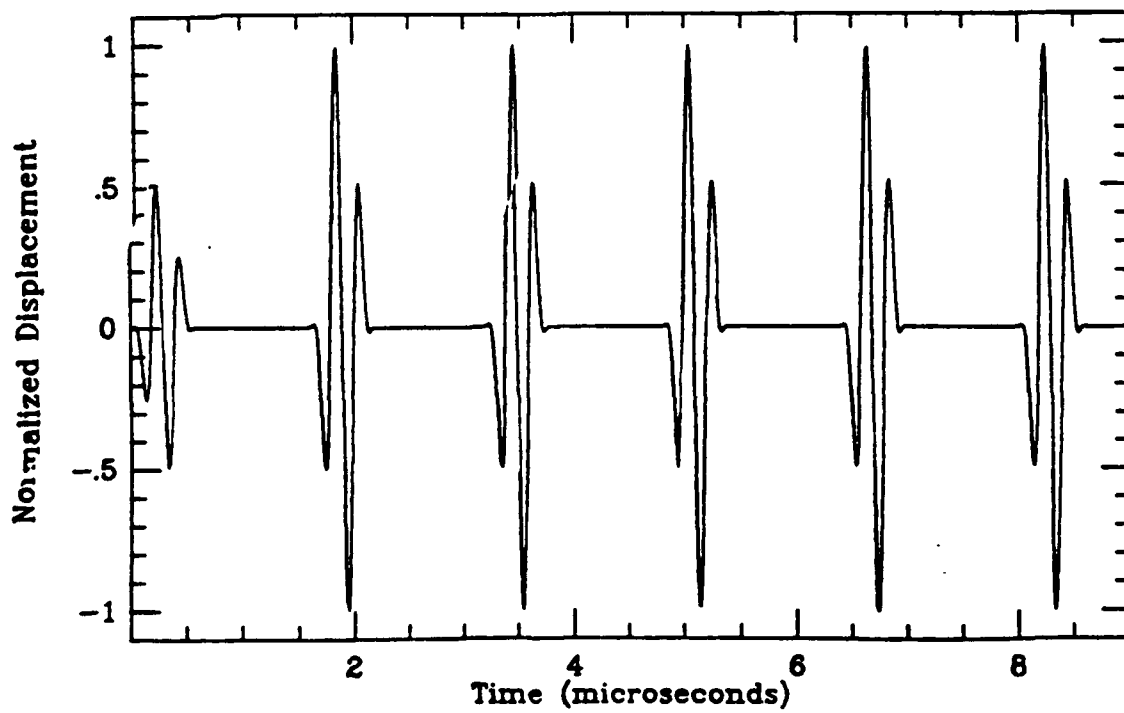


Figure 5.6: Effect of artificial dispersion for $q = .995$

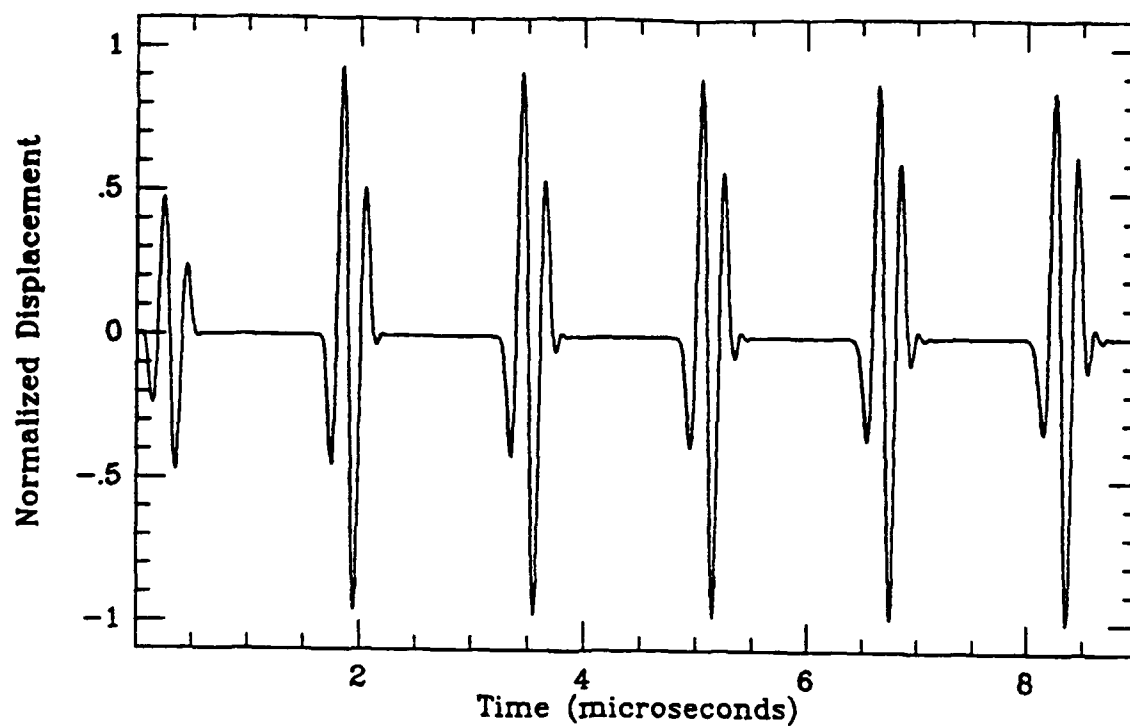


Figure 5.7: Effect of artificial dispersion for $q = .800$

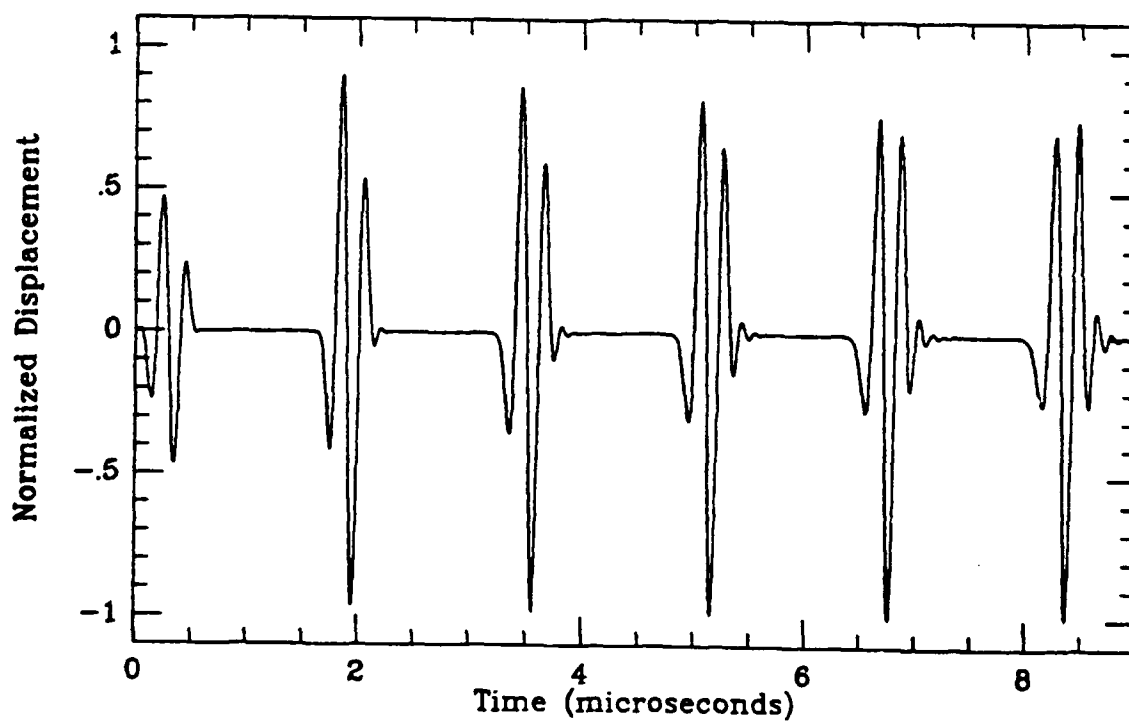


Figure 5.8: Effect of artificial dispersion for $q = .500$

effect caused purely by the mass lumping.

5.3 Qualitative Results

The wavefronts produced by the finite element code are compared with Figure (2.1) and (2.2) qualitatively by plotting the displacement fields for a point source and a one quarter inch transducer at a given time step. Surface plots are used to display a single displacement component. Although the wavefronts can be clearly identified, the plots do not represent the actual wavefront shapes which contain only in-plane displacements. A 7.0 by 7.0 mm mesh with Aluminum material properties is used and displacements are stored at 1.2 μs for the point source and at 0.8 μs for the transducer.

Line and Point Source

Figures (5.9) and (5.10) show the point force displacement results for the plane strain and axisymmetric codes, respectively. The wavefronts agree with those predicted in Figure (2.1). The longitudinal, shear, head and Rayleigh waves can all be identified. The longitudinal wave does not fully appear in either plot. The x,z displacements are zero in the y,r direction and the y,r displacements are zero in the x,y direction as expected, which confirms that the displacement direction is parallel to the direction of wave propagation. There is a small bias in amplitude to the x,z direction which is justified because that is the direction of the applied load. The slope of the shear wave in the y,r direction is not zero at the axis of symmetry. This does not create a discontinuity because in the mirror image the y,r displacements must be reversed in sign to maintain a symmetric response. There is no sign reversal for the x,z displacements. The Rayleigh wave will also have a similar sign reversal for its y,r displacements. The Rayleigh wave has the largest amplitude and does appear to decrease exponentially away from the surface. The x,z and r,y displacements for the Rayleigh wave are out of phase by 90 degrees which agrees with the expected ellipsoidal motion. The large Rayleigh wave obstructs the view of the head wave that originates where the longitudinal wave

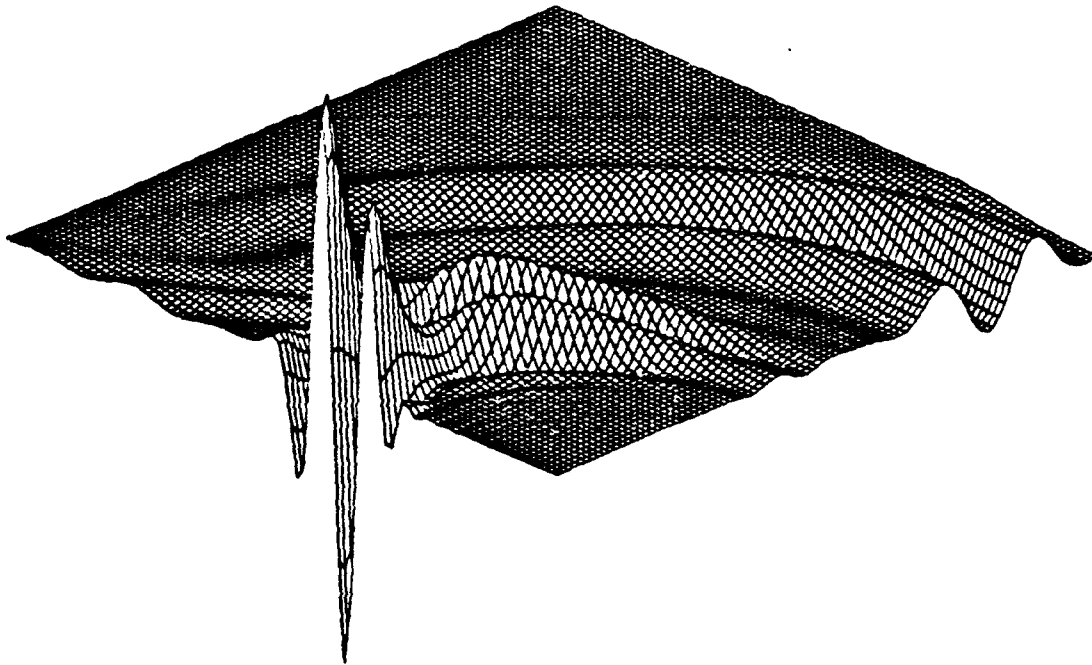


Figure 5.9a: U_x surface plot for a line source , $f = 5 \text{ MHz}$ $t = 1.2 \mu\text{s}$

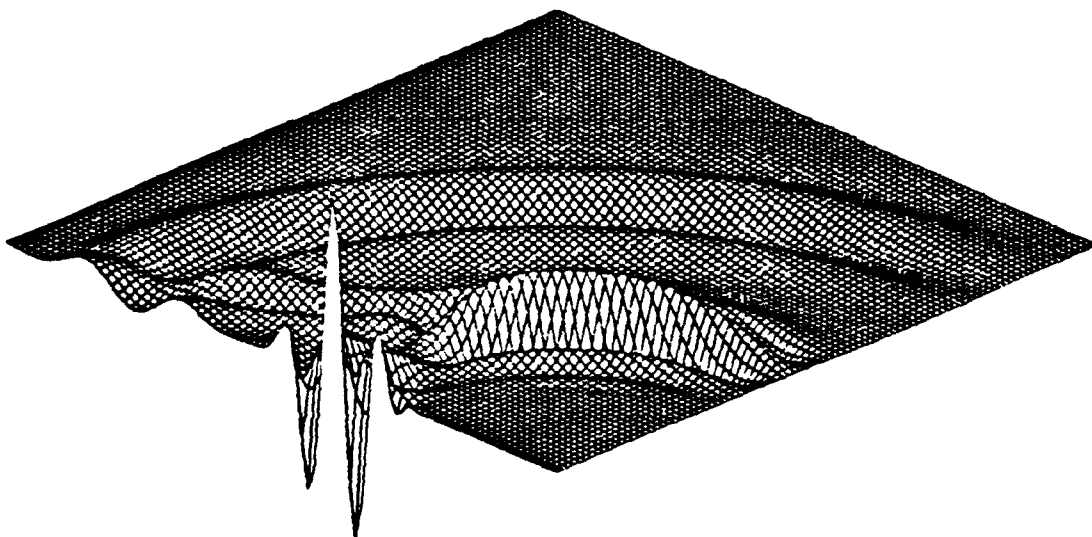


Figure 5.9b: U_y surface plot for a line source , $f = 5 \text{ MHz}$ $t = 1.2 \mu\text{s}$

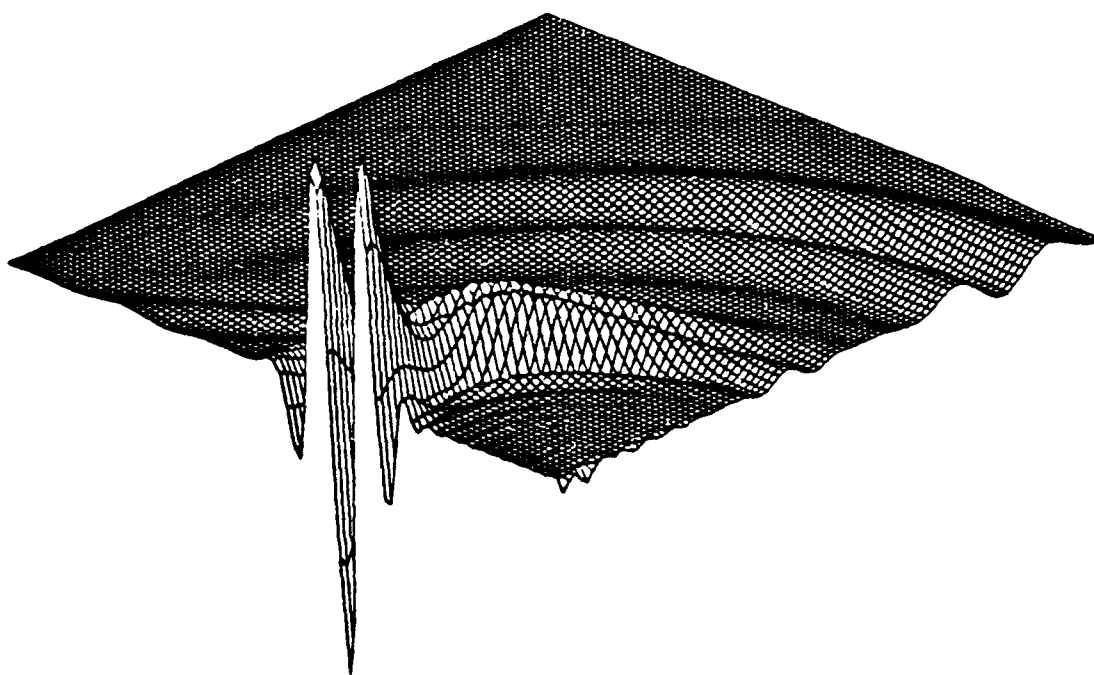


Figure 5.10a: U_z surface plot for a point source , $f = 5 \text{ MHz}$ $t = 1.2 \mu\text{s}$

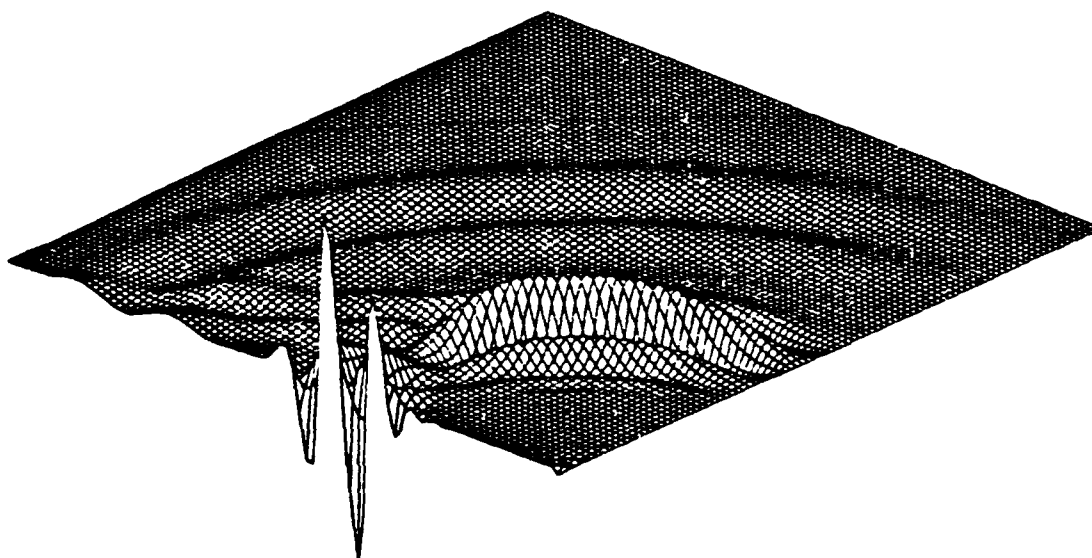


Figure 5.10b: U_r surface plot for a point source , $f = 5 \text{ MHz}$ $t = 1.2 \mu\text{s}$

grazes the top surface and connects tangentially to the shear wave. The axisymmetric wave amplitudes decrease faster than the plane strain wave amplitudes as the waves move away from the center because of the difference in geometric dispersion.

Transducer

Figures (5.11) and (5.12) show the displacement plots for the one quarter inch transducer. Again the wavefronts agree well with those predicted in Figure (2.2). Most of the energy from the center of the transducer goes directly into the flat longitudinal wave giving it the greatest amplitude. The other waves are smaller because they are generated only from the discontinuity at the edge of the

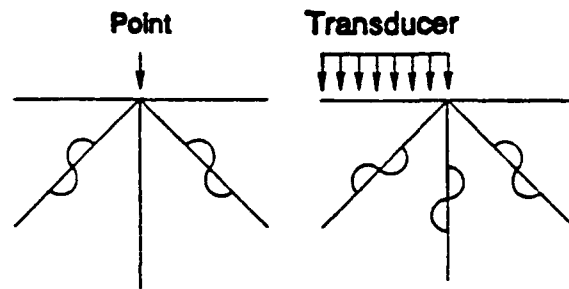


Figure 5.13: Point source and edge effect shear wave propagation.

transducer. The waves caused by the discontinuity are similar but not identical to those caused by a point force. The shear and Rayleigh waves are now inverted in the x, z displacements and have the same sign in the y, r displacements. Figure (5.13) shows more clearly how the step discontinuity differs from the point source. Again, waves moving away from the center are attenuated faster in the axisymmetric case because of the difference in geometric dispersion. Waves that are travelling towards the center for the axisymmetric case will actually gain amplitude as the spherical wavefront collapses.

5.4 Analytic Results Comparison

Analytic solutions for a line source and a point source at points within the domain are plotted against the numerical solutions as a means of validating the finite element code. The analytic solutions presented here were calculated with the Cagnaird de-Hoop

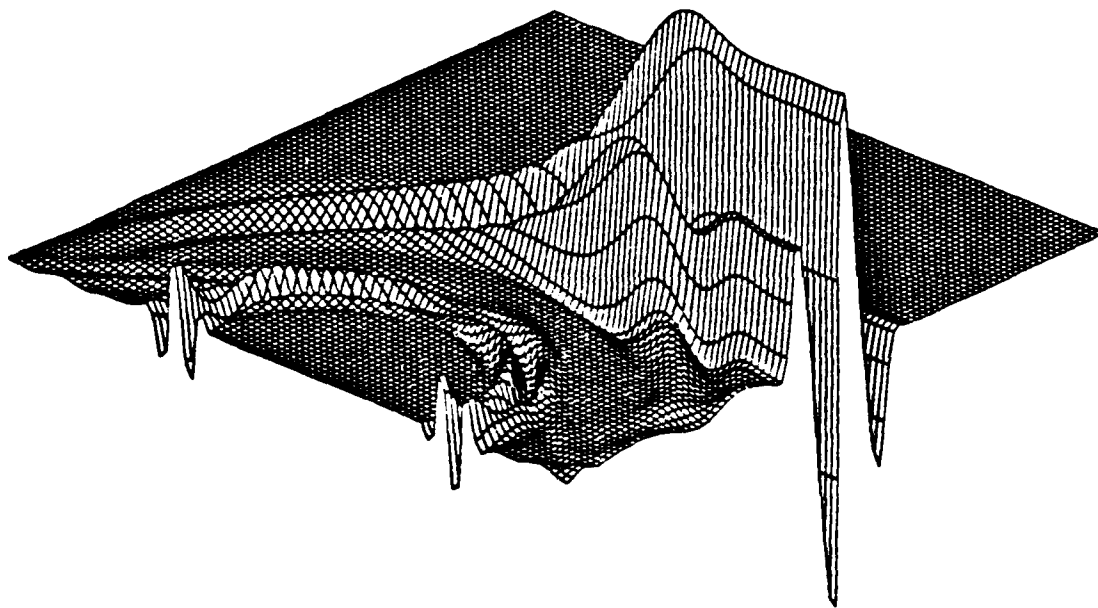


Figure 5.11a: U_x surface plot for plane strain with a 1/4 inch transducer, $f = 10 \text{ MHz}$ $t = 0.8 \mu\text{s}$

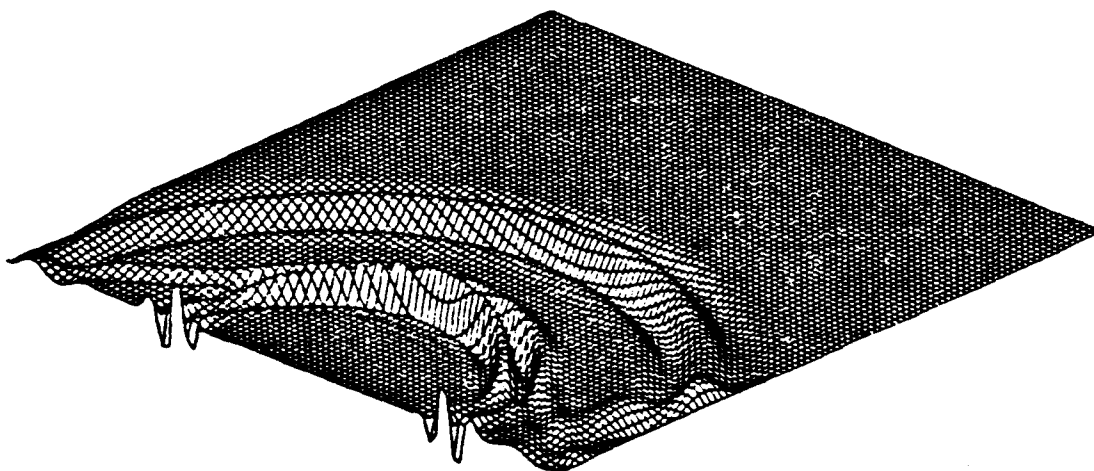


Figure 5.11b: U_y surface plot for plane strain with a 1/4 inch transducer, $f = 10 \text{ MHz}$ $t = 0.8 \mu\text{s}$

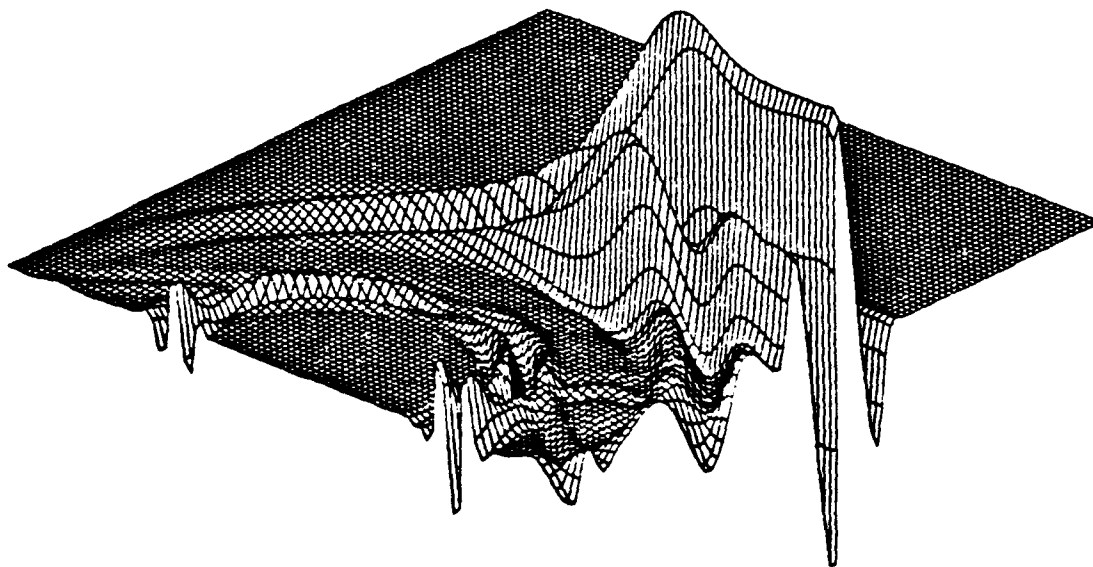


Figure 5.12a: U_z surface plot for axisymmetric with a 1/4 inch transducer, $f = 10 \text{ MHz}$ $t = 0.8 \text{ } \mu\text{s}$

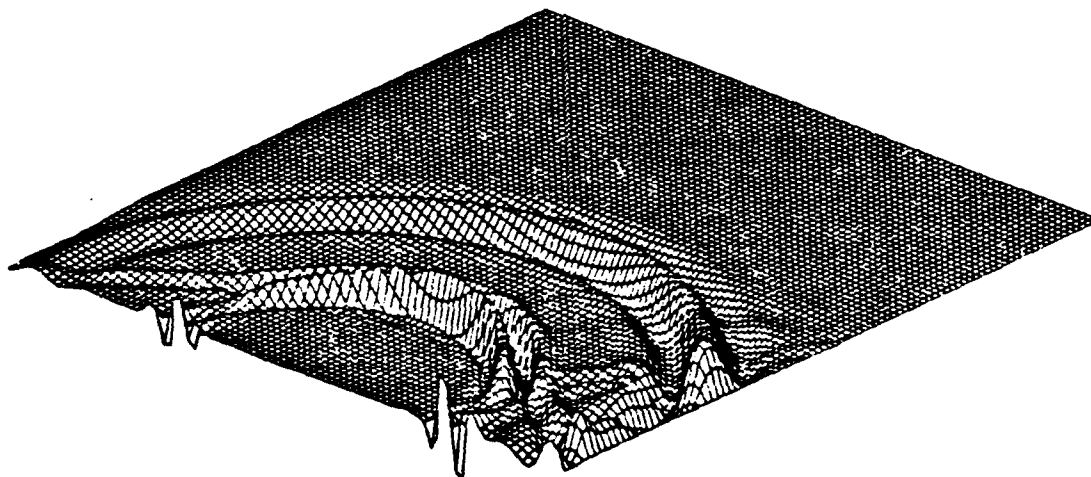


Figure 5.12b: U_r surface plot for axisymmetric with a 1/4 inch transducer, $f = 10 \text{ MHz}$ $t = 0.8 \text{ } \mu\text{s}$

formalism presented in [4] by S. Dai. A raised cosine signal at 10 MHz is used as an input and the points were taken at radii of $R = 1.0, 2.0$ and 4.0 mm each at angles of $\psi = 0, 30, 60$ and 87 degrees, see Figure (5.14). The results are shown in Figures (5.15-21). At $\psi = 0$, y, r

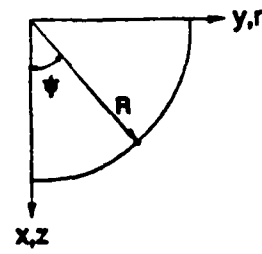


Figure 5.14: Location of points for analytic comparisons.

direction displacements are not plotted because they are set to zero by the applied boundary condition along the axis of symmetry. Reflections from the finite sized numerical model are not shown because the analytic solution assumes an infinite medium.

All three R locations are plotted on the same graph. The $R = 2.5$ and 4.0 mm signals have been offset on the abscissa by 1.0 and 2.0 , respectively, to separate the signals completely.

The line source results for the plane strain code compare very well with the analytic solutions for angles of less than 30 degrees. As ψ increases, the solutions no longer agree. This is due to the singularity of the analytic integration at the $x = 0$ surface which distorts the head wave. Table (5.1) lists the correct arrival time for the longitudinal, shear and head waves. The head wave is tangent to the shear wave at $\psi = 33.4$ degrees, therefore head wave timings are only listed for 60 and 80 degrees. The longitudinal and shear waves arrive at the same time for all values of ψ for a given R . The numerical solution gives the correct arrival times. The solutions also appear to agree better once the longitudinal and shear waves have separated at $R = 2.0$ and 4.0 mm. The difference at $R = 1.0$ mm might be explained by a slight difference in timing which causes the waves to add differently making the displacements appear to be dissimilar.

The point source numerical solution results are plotted in Figures (5.22-28). Although the analytic data was not available, the results compare well with those presented in [24]. The analytic solution for a dirac delta function point load is a dirac delta displacement wave, therefore a longitudinal wave created by convolving a dirac delta function into a

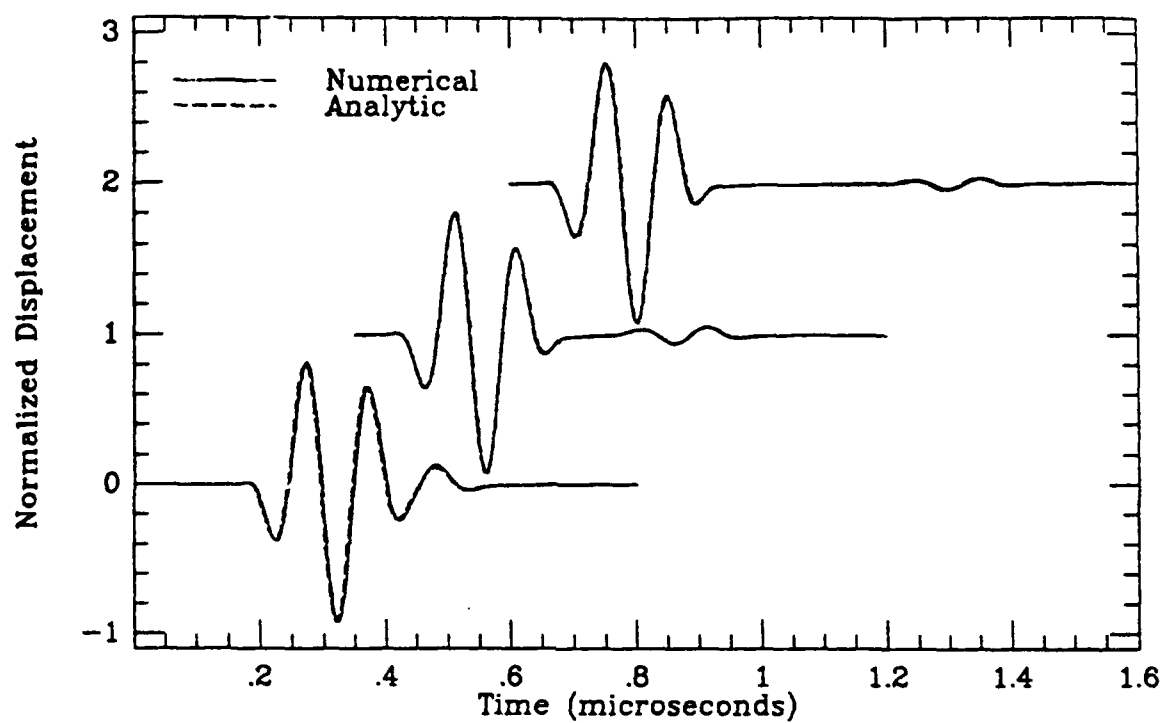


Figure 5.15: Line source x-direction displacement $\psi = 0$ $f = 10$ MHz

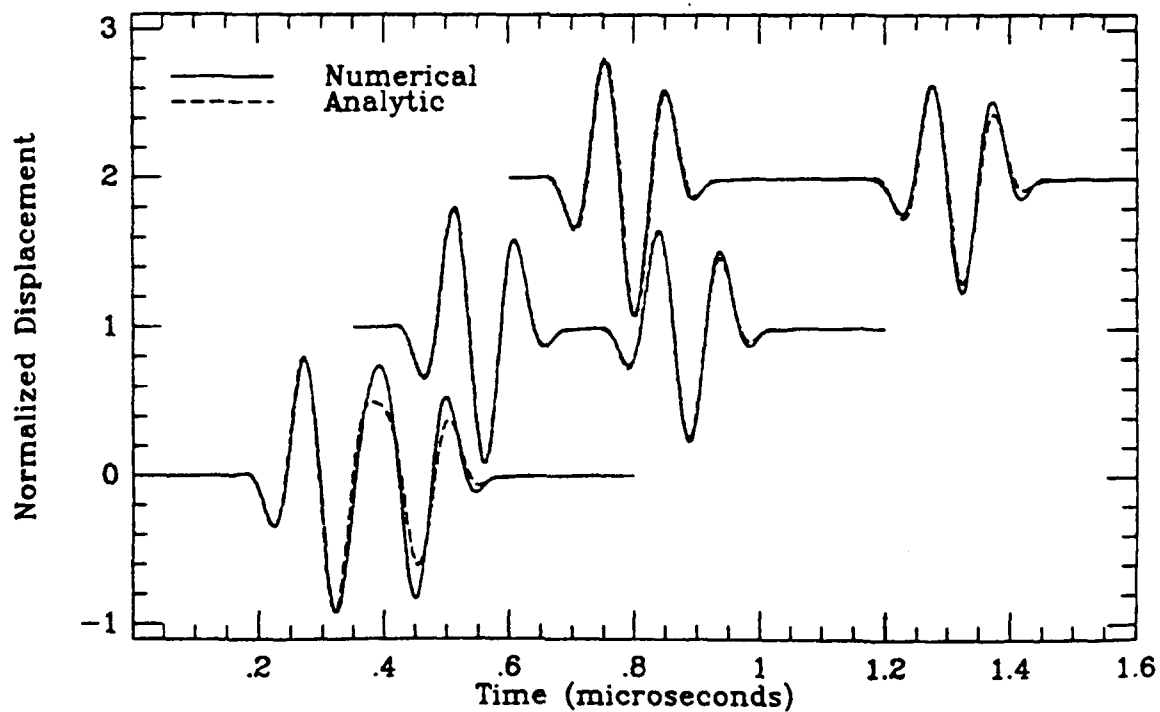


Figure 5.16: Line source x-direction displacement $\psi = 30$ $f = 10$ MHz

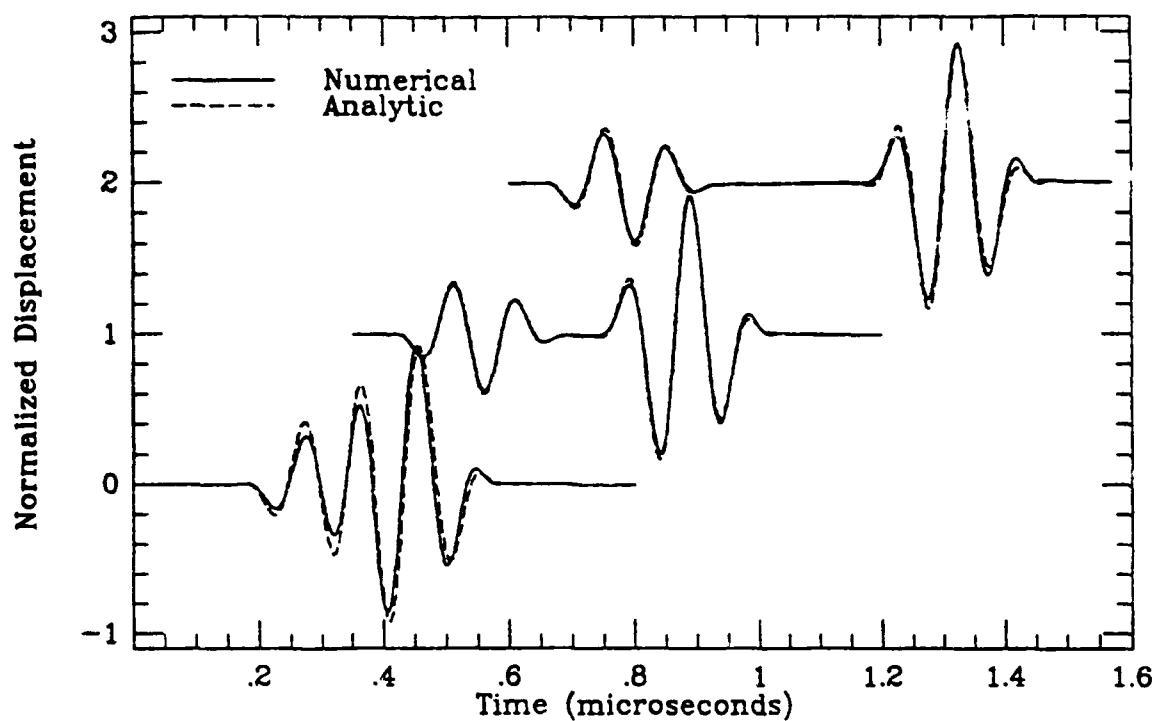


Figure 5.17: Line source y-direction displacement $\psi = 30 f - 10 \text{ MHz}$

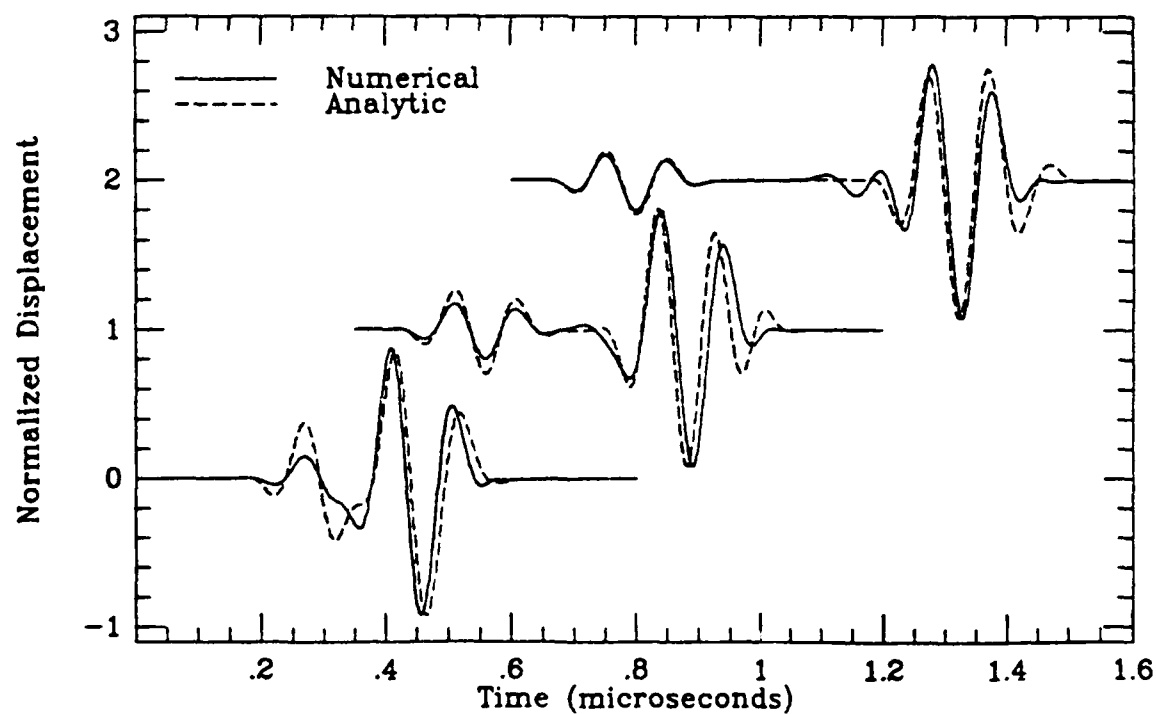


Figure 5.18: Line source x-direction displacement $\psi = 60 f - 10 \text{ MHz}$

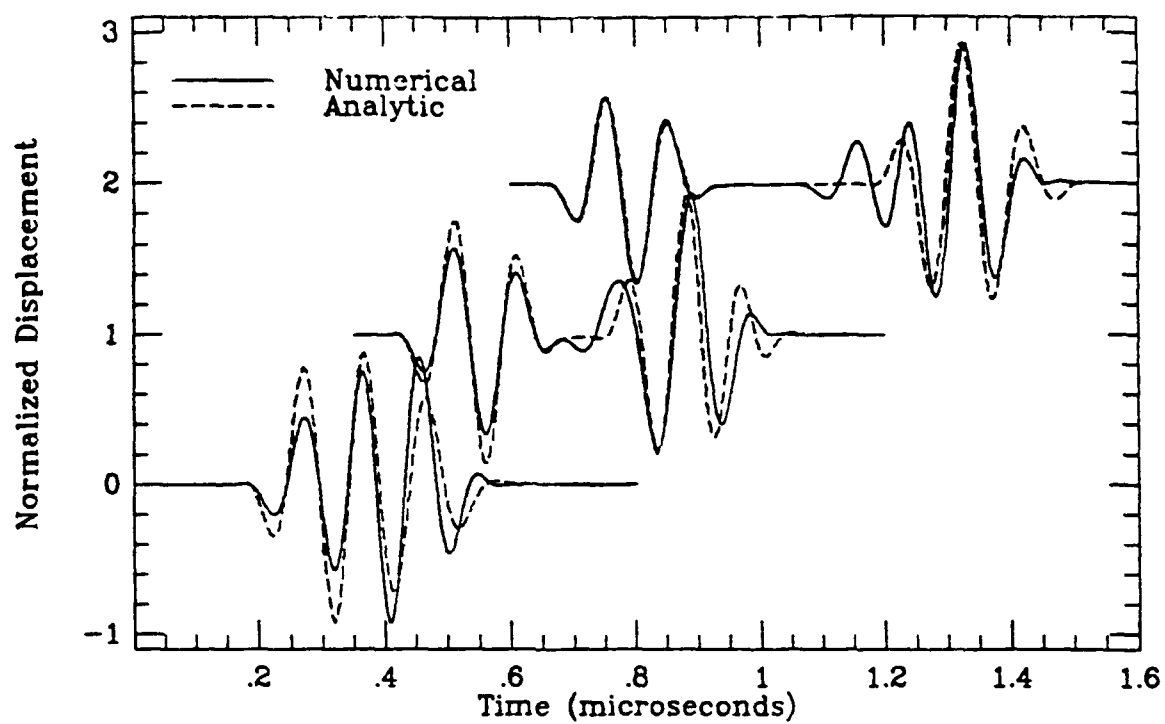


Figure 5.19: Line source y-direction displacement $\psi = 60^\circ$ $f = 10$ MHz

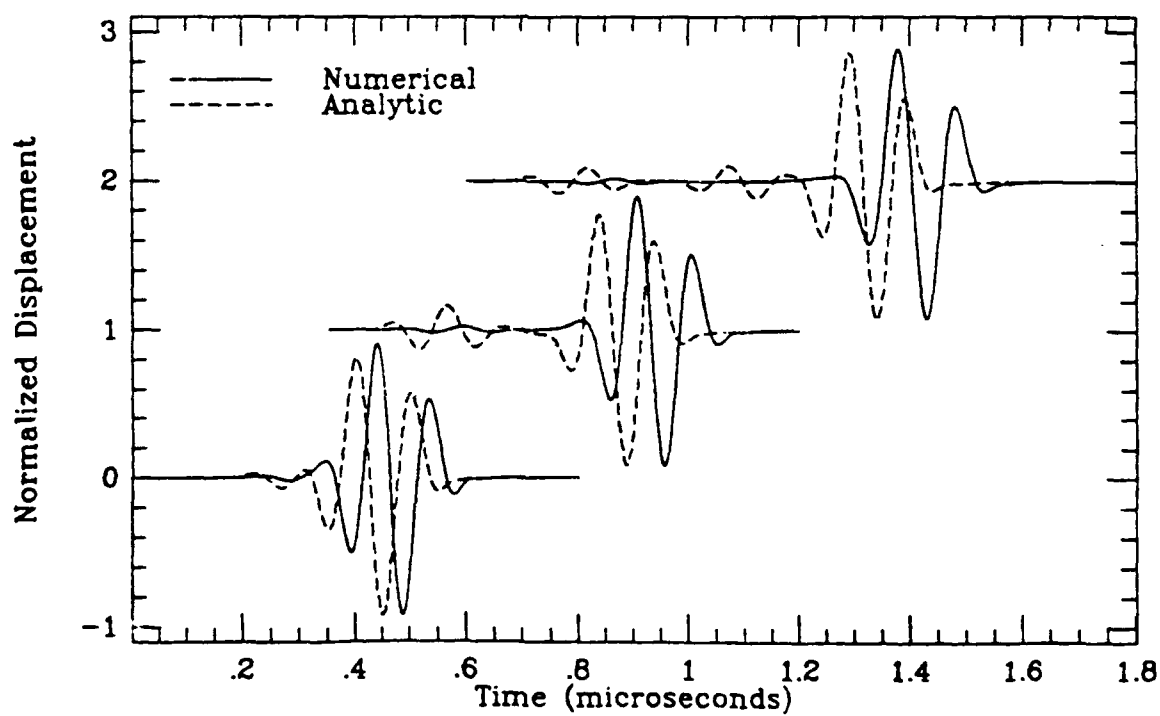


Figure 5.20: Line source x-direction displacement $\psi = 87^\circ$ $f = 10$ MHz

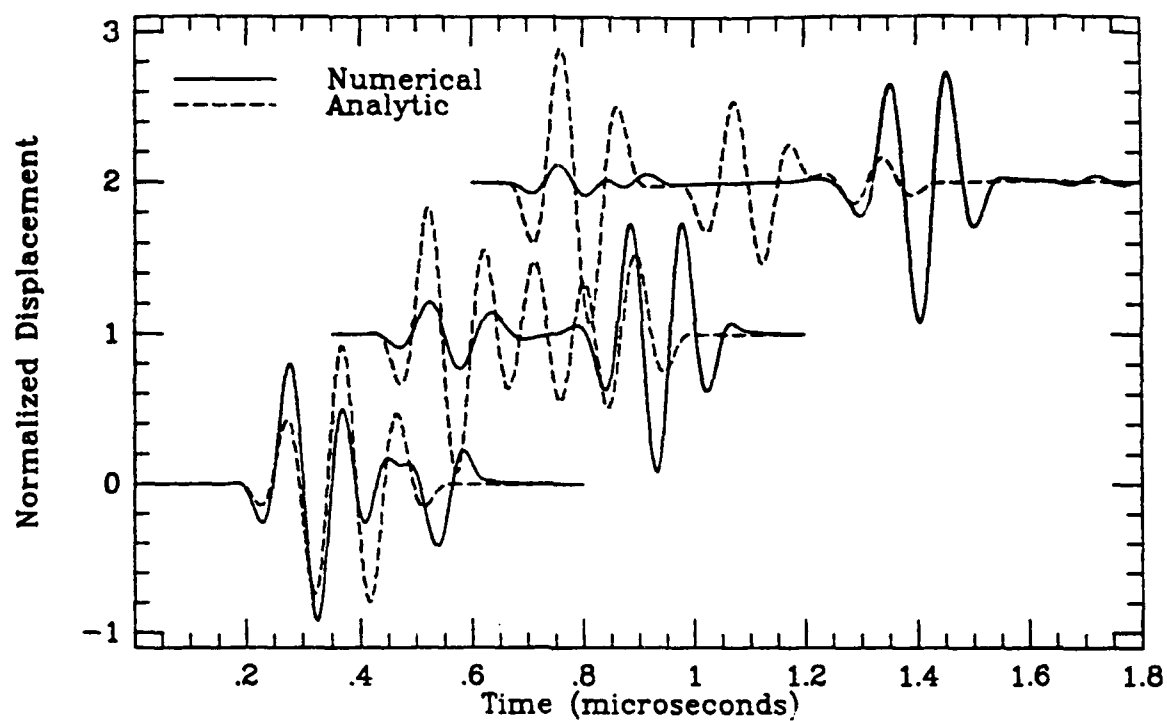


Figure 5.21: Line source y-direction displacement $\psi = 87 f - 10 \text{ MHz}$

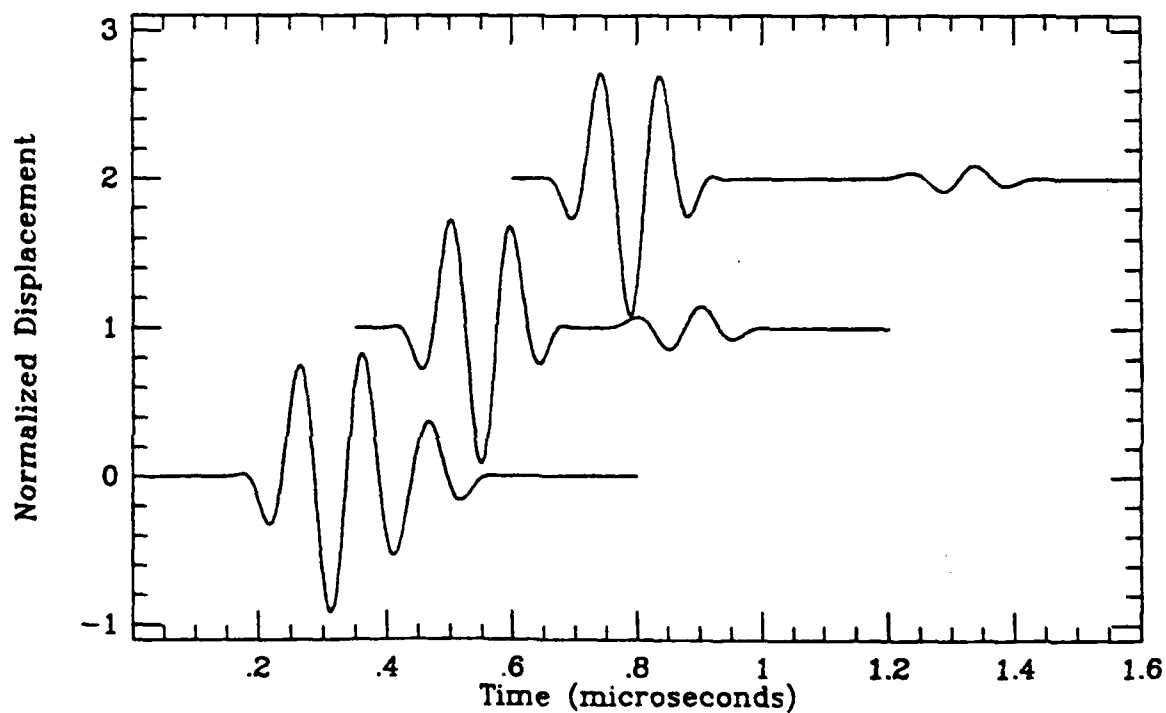


Figure 5.22: Point source z-direction displacement $\psi = 0 \quad f - 10 \text{ Mhz}$

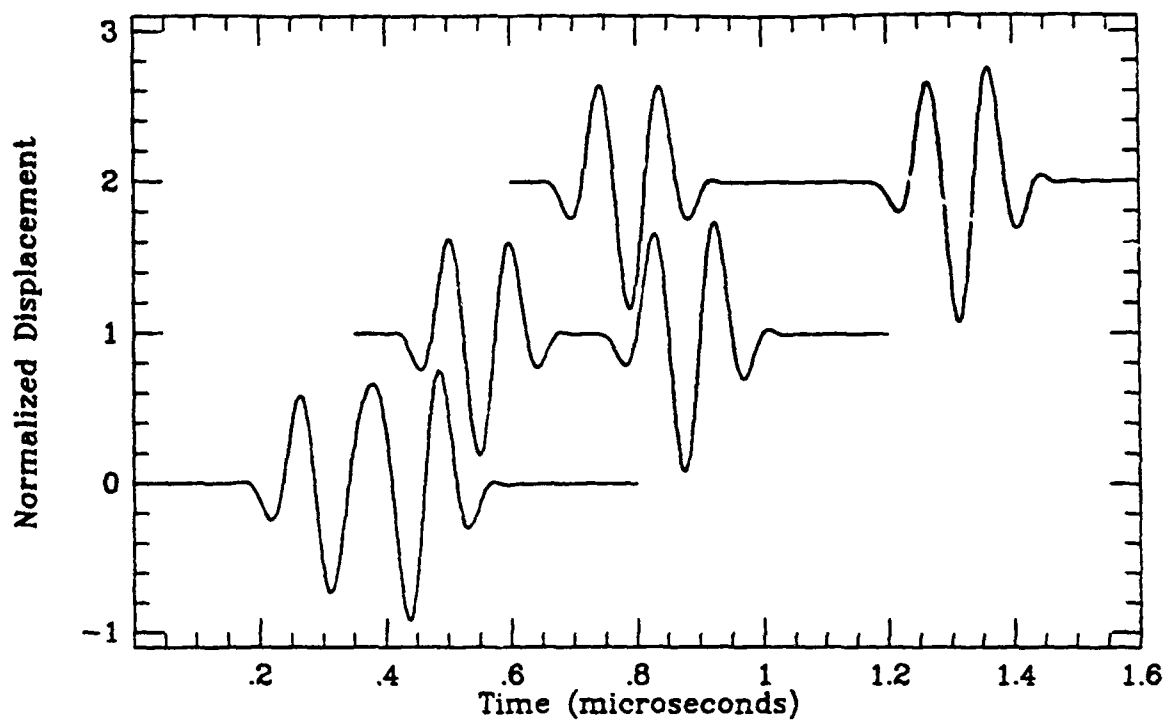


Figure 5.23: Point source z -direction displacement $\psi = 30$ $f = 10$ MHz

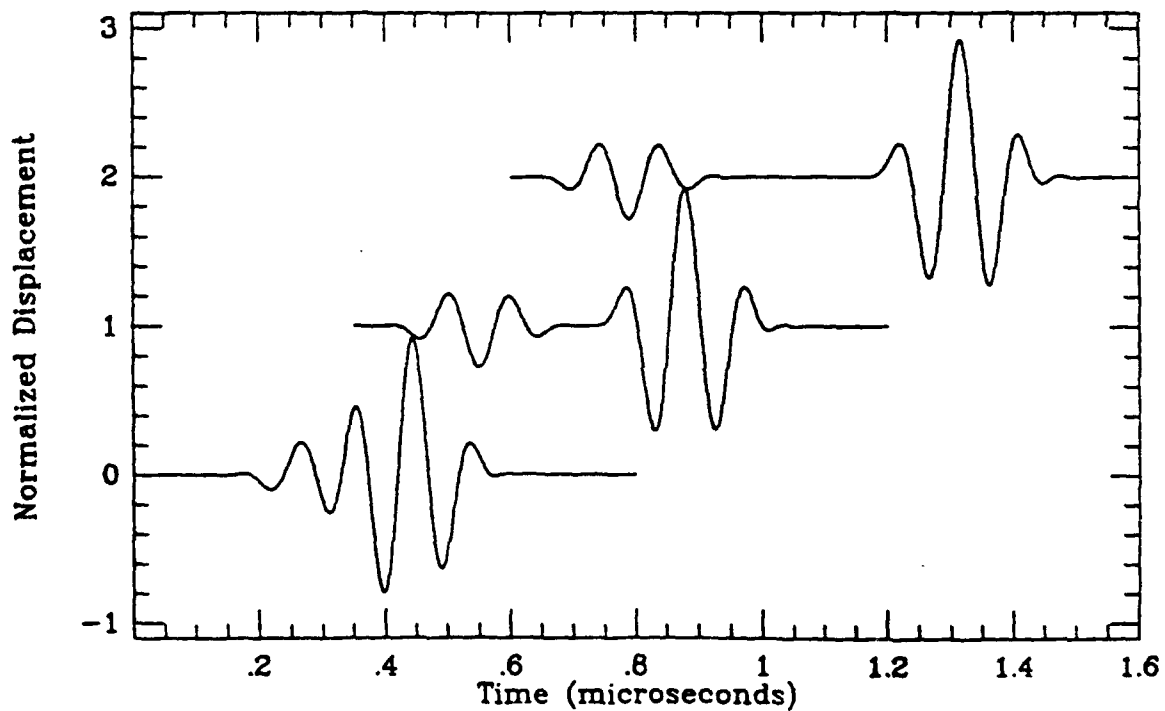


Figure 5.24: Point source r -direction displacement $\psi = 30$ $f = 10$ MHz

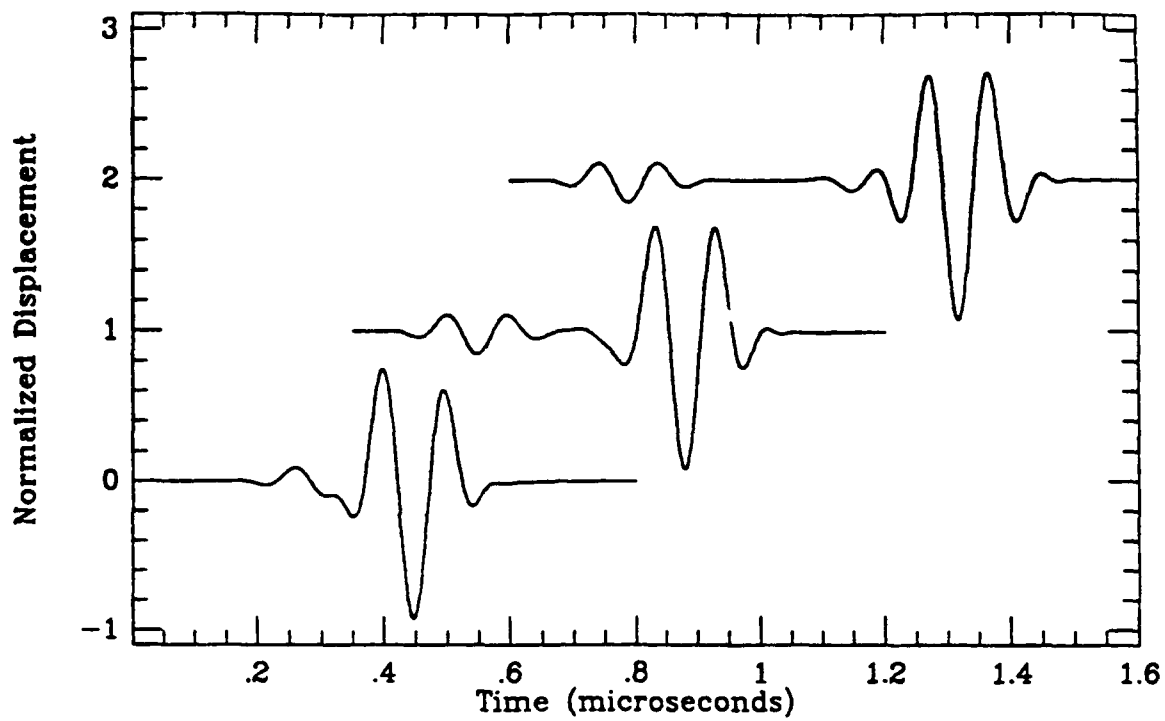


Figure 5.25: Point source z -direction displacement $\psi = 80$ $f = 10$ MHz

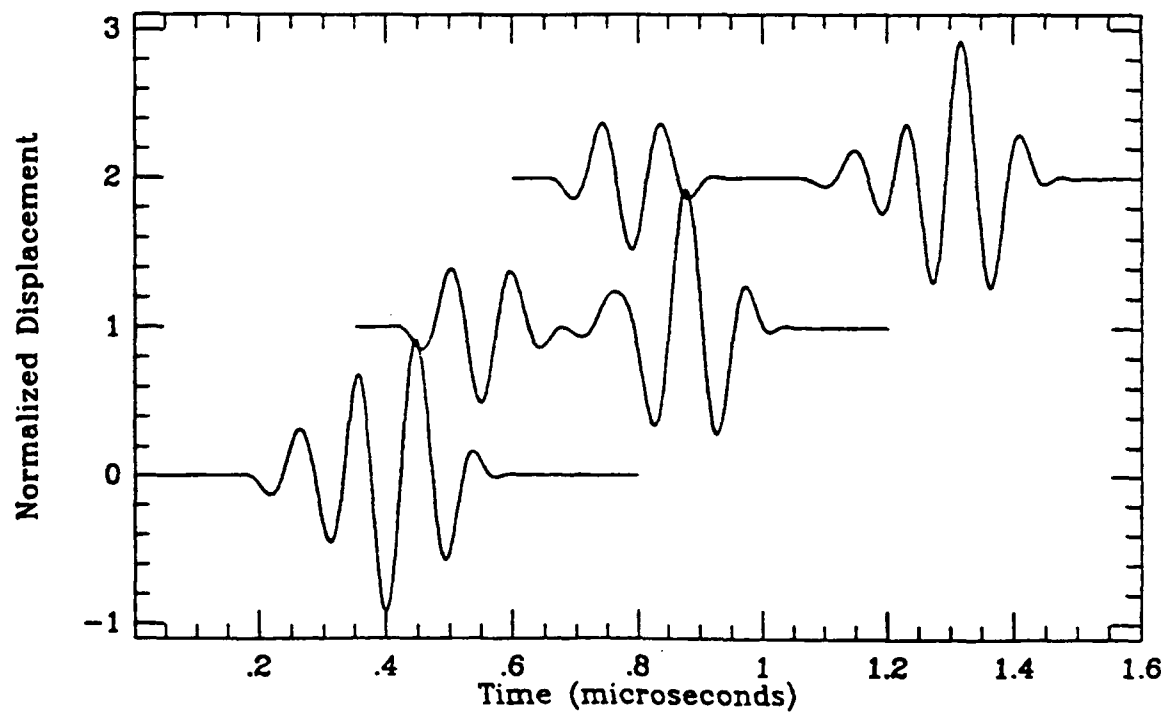


Figure 5.26: Point source r -direction displacement $\psi = 80$ $f = 10$ MHz

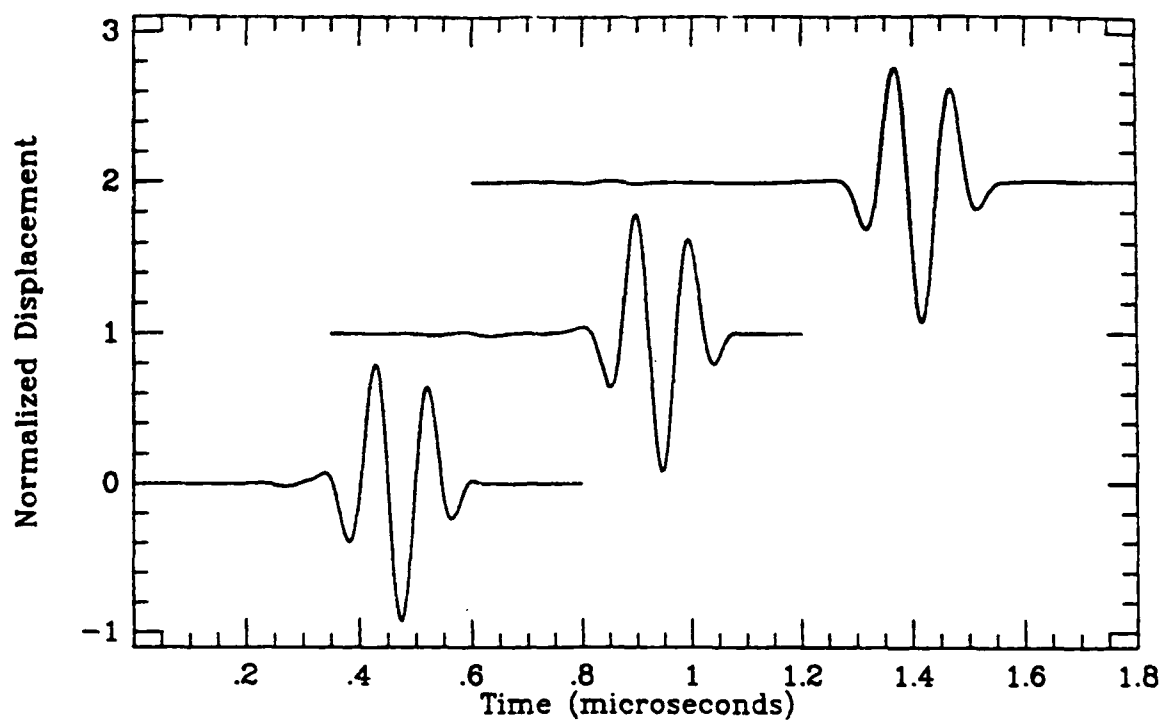


Figure 5.27: Point source z -direction displacement $\psi = 87 f - 10 \text{ MHz}$

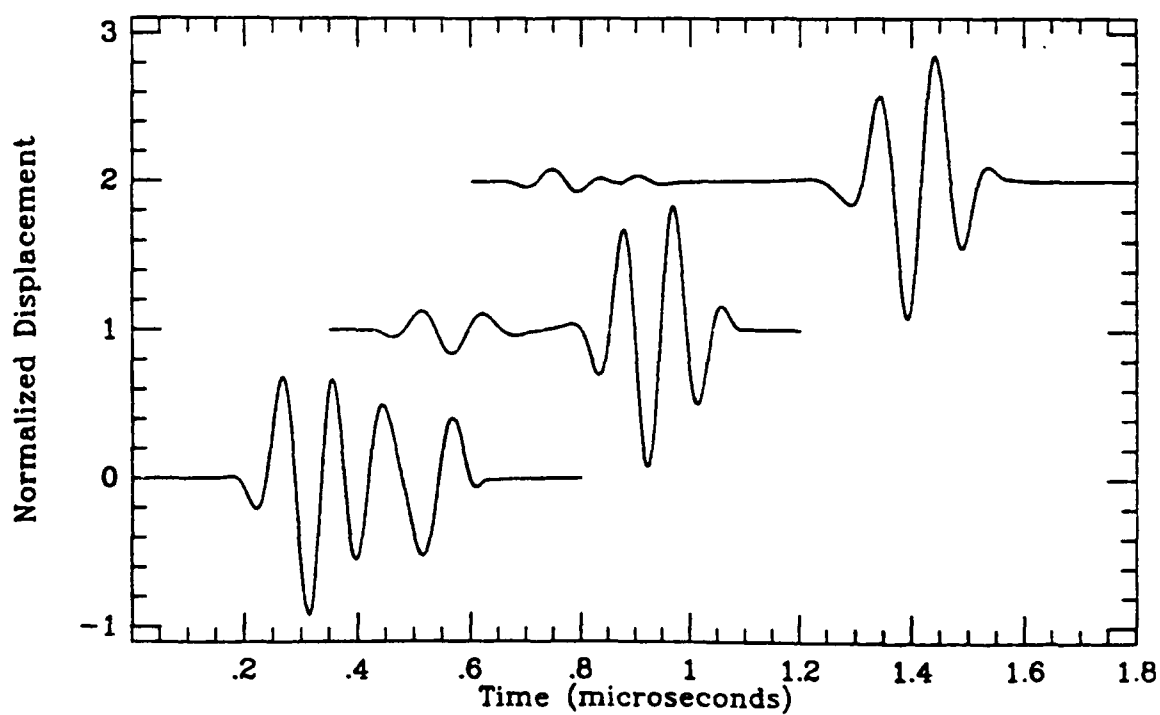


Figure 5.28: Point source r -direction displacement $\psi = 87 f - 10 \text{ MHz}$

Table 5.1: Longitudinal, shear and head wave arrival times in μs .

radius	Long.	Shear	Head Wave	
			60°	87°
1.0	.1597	.2900	.2594	.1722
2.5	.3993	.7251	.6484	.4304
4.0	.6389	1.1601	1.0374	.6887

raised cosine produces a raised cosine displacement. The longitudinal wave for the numerical solution is a raised cosine as expected. The wave timings also agree well with those listed in Table (5.1).

5.5 Experimental Results Comparison

A total debond is modeled experimentally using a single aluminum plate supported at the perimeter. The transducer is placed in the center of the plate to avoid contaminating the A-scan results with reflections from the plate edges. One

quarter inch diameter transducers with center frequencies of 5 and 10 MHz

are used. Figure (5.29) shows the physical dimensions of the experimental configuration. The material properties of the aluminum are $C_l = 6261.0 \text{ m/s}$, $C_s = 3448.2 \text{ m/s}$ and $\rho = 2842.0 \text{ kg/m}^3$. The numerical A-scans are calculated by a weighted average of the displacements at the nodes under the transducer for each time step. The weighting is the same as the distribution of the uniform load to the nodes.

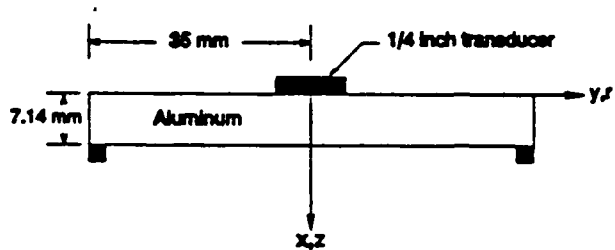


Figure 5.29: Single aluminum plate experimental configuration. (not to scale)

The experimental and numerical results are compared in Figure (5.30). The experimental data is shifted so that the first longitudinal reflection overlays with the numerical

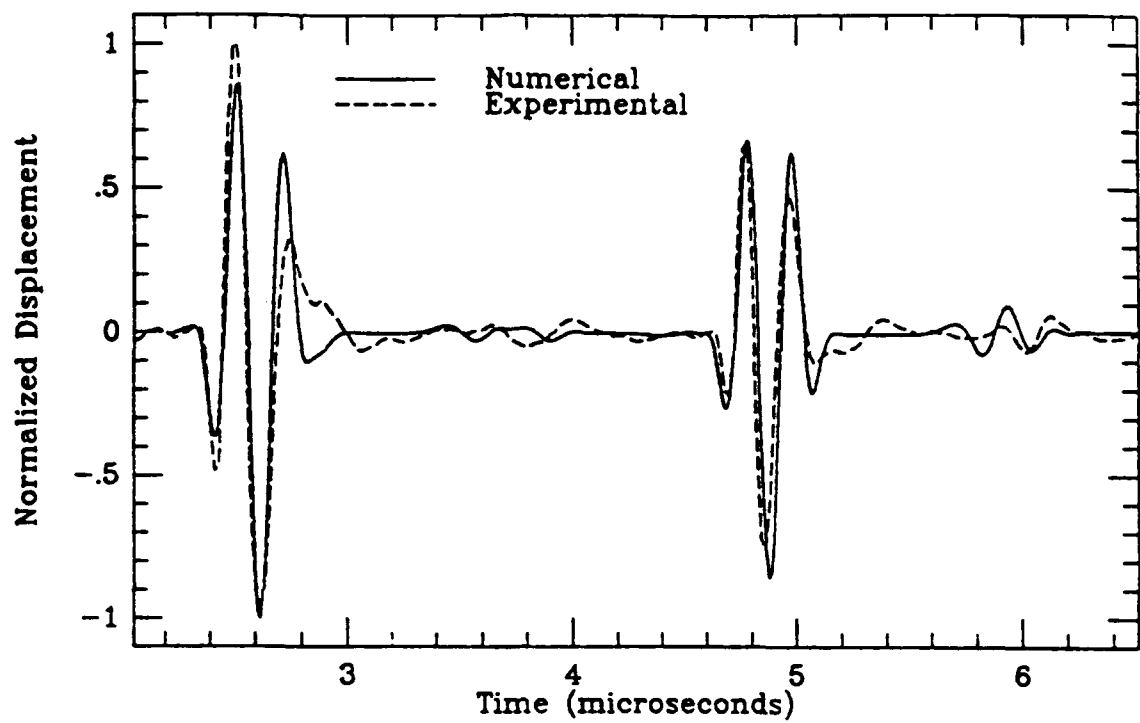


Figure 5.30a: Numerical and experimental A-scans for debond, $f = 5$ MHz

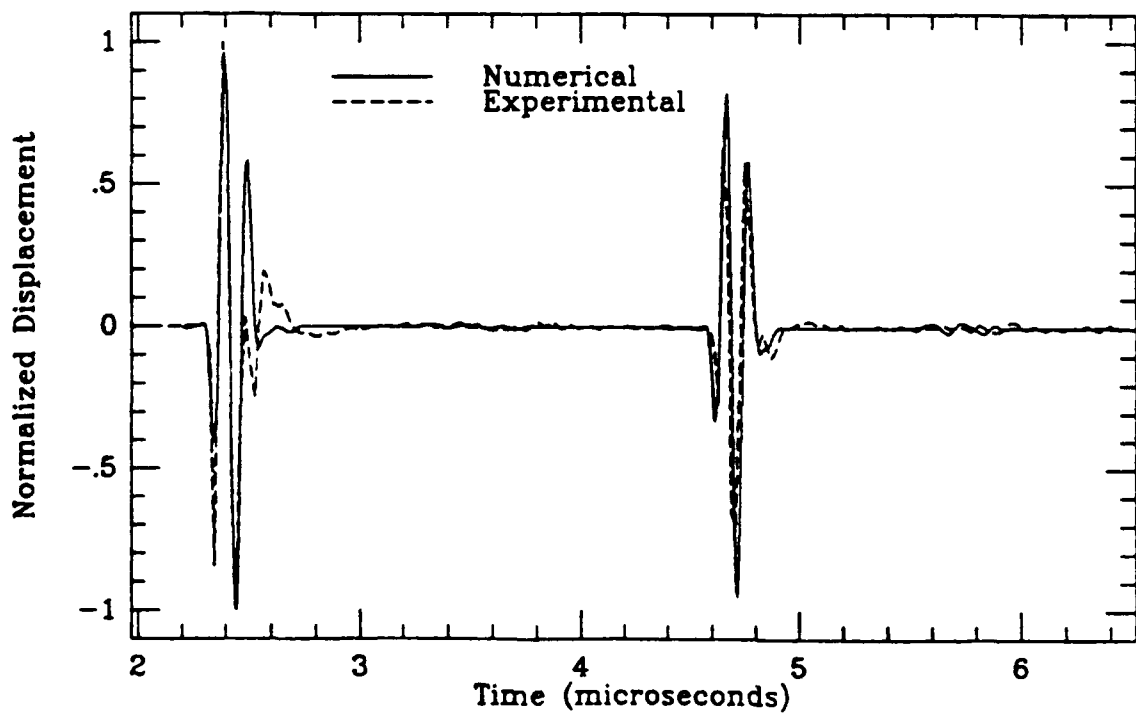
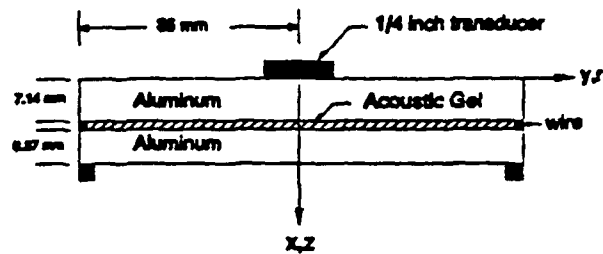


Figure 5.30b: Numerical and experimental A-scans for debond, $f = 10$ MHz

prediction. The axisymmetric code without material damping is used for the numerical solution. The experimental and numerical results are in excellent agreement even without any damping effects. The large waveforms are the first and second longitudinal wave reflections from the bottom surface. The shallow waveforms between the longitudinal reflections are mode converted shear waves created when the longitudinal wave reflects from the bottom surface. Inspection of the experimental results suggests that the input wave is close to the raised cosine but not exactly the same.

A schematic of the layered material experimental configuration using two aluminum plates separated by a thin layer of acoustic gel is shown in Figure (5.31). The material properties of the gel are $C_l = 1490 \text{ m/s}$ and $\rho = 1080.0 \text{ kg/m}^3$.



The shear wave velocity for the gel is very low and is estimated for the numerical solution as 10 percent of C_l . The bond thickness is controlled by a small diameter wire placed around the perimeter of the plates. Physical dimensions are also shown in Figure (5.31).

Figure (5.32) compares the experimental results to numerical solutions. The first wave is the longitudinal wave reflection from the bottom of the top plate. The following smaller wave is the longitudinal wave reflected from the top surface of the lower aluminum plate. The next two waves are longitudinal waves that have reflected back and forth within the bond layer multiple times. The phase difference in the bond layer reflections could be caused by the lack of damping in the numerical model.

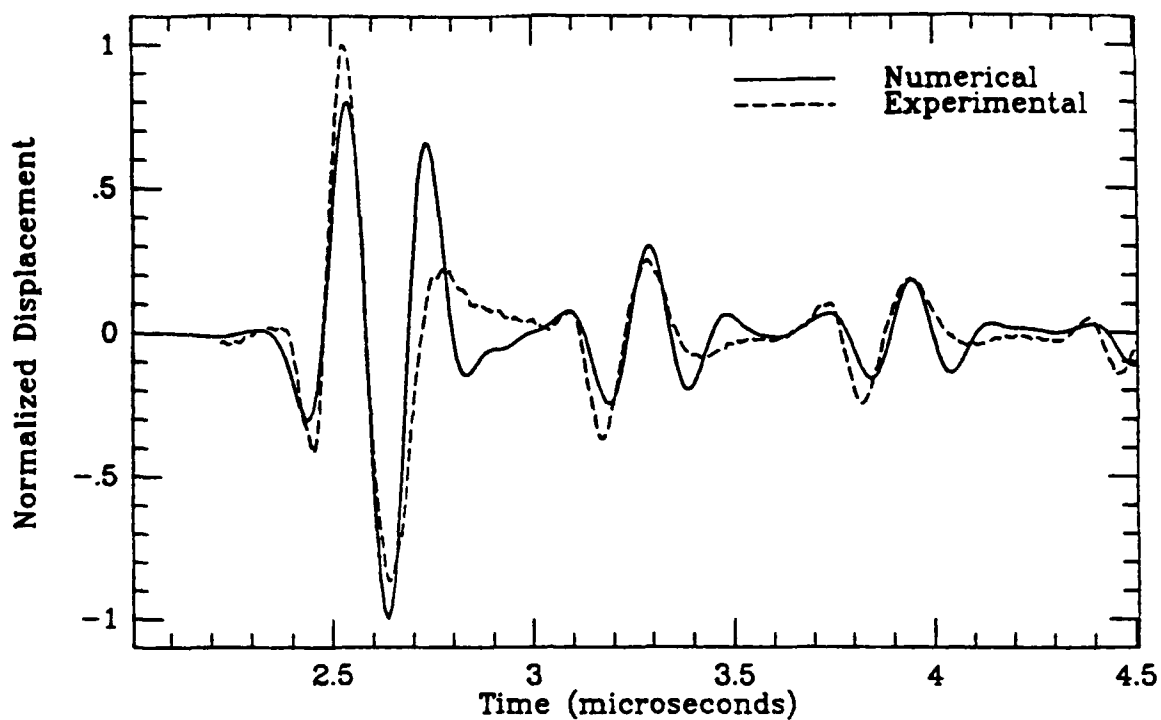


Figure 5.32a: Numerical and experimental A-scans for .486 mm bond $f = 5$ MHz

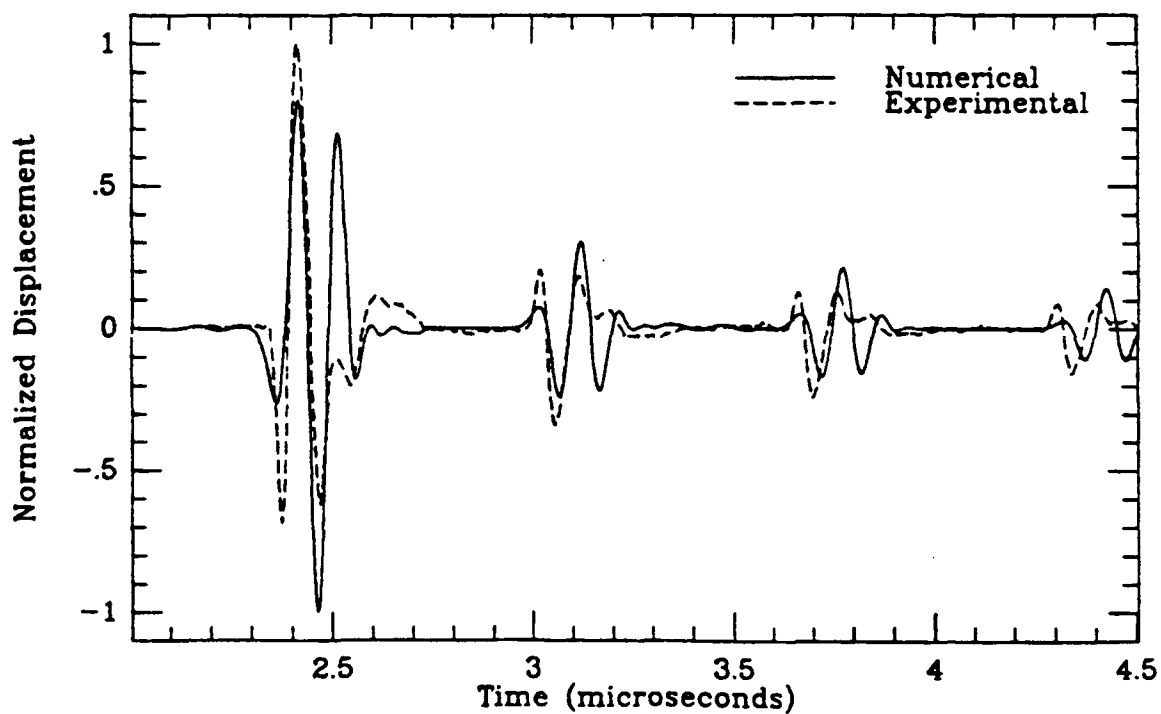


Figure 5.32b: Numerical and experimental A-scans for .486 mm bond $f = 10$ MHz

5.6 Attenuation Example

The damping effect on wave propagation is illustrated by plotting the displacements at successive time intervals with the same scale. The z direction displacements are plotted for a undamped and a damped case at $t = 1.0, 2.0, 3.0$, and $4.0 \mu s$ in Figures (5.33-36). The damping is assumed to be isotropic with values of $D_{1111} = 111.45 \text{ NS/m}^2$ and $D_{1212} = 25.07 \text{ NS/m}^2$ [11] so that the damping matrix is proportional to the stiffness matrix. This situation is equivalent to Rayleigh damping with $\alpha = 0$ [16].

The attenuation of the longitudinal wavefront is evident after only one reflection. At $t = 4.0 \mu s$ the longitudinal wave has been reflected by the top surface for the first time. Introducing viscous damping through equation (2.2) results in damping that is proportional to the square of the frequency, which results in a dispersive solution. Therefore, in addition to decreasing the amplitude of the waves, the damping term produces a change in the waveform. The actual damping in a polycrystalline solid such as aluminum has a more complex attenuation that becomes proportional to the frequency to the fourth power for very high frequencies [31].

5.7 Anisotropy Example

The anisotropic capability of the code is tested using the transversely isotropic $[C]$ matrix for Cobalt. The components of $[C]$ are

$$\begin{aligned} C_{1111} &= 35.81 \times 10^{10} \text{ N/m}^2 \\ C_{1122} &= 10.27 \times 10^{10} \text{ N/m}^2 \\ C_{2233} &= 16.50 \times 10^{10} \text{ N/m}^2 \\ C_{2222} &= 30.70 \times 10^{10} \text{ N/m}^2 \\ C_{1212} &= 7.510 \times 10^{10} \text{ N/m}^2 \\ \rho &= 8900.0 \text{ kg/m}^3 \end{aligned} \tag{5.3}$$

Figure (5.37) shows the z and r direction displacements respectively at $t = 1.8 \mu s$ for

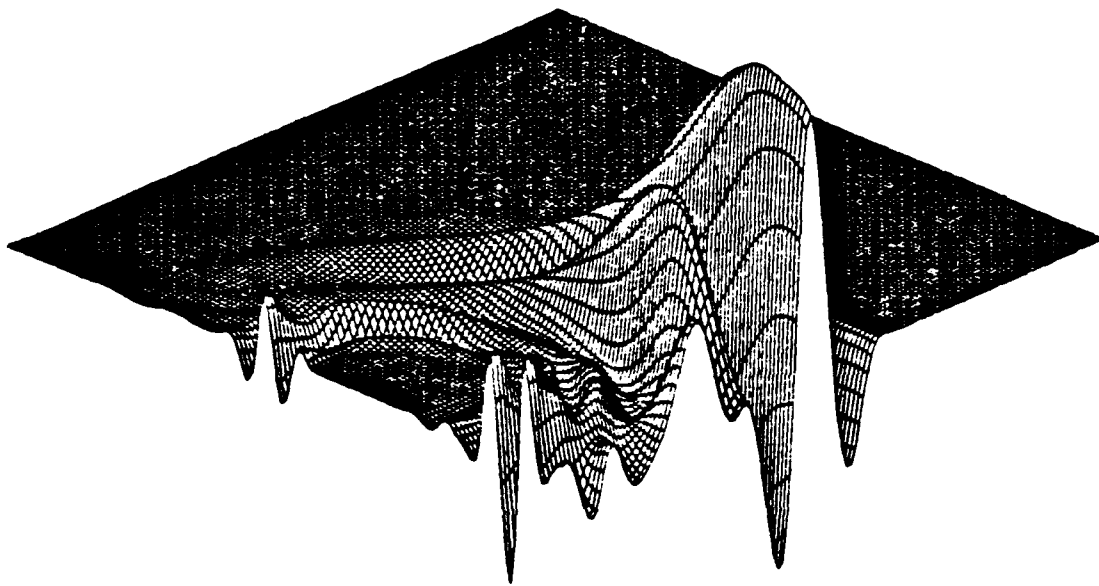


Figure 5.33a: Undamped axisymmetric U_z surface plot, $f = 5 \text{ MHz}$ $t = 1.0 \text{ } \mu\text{s}$

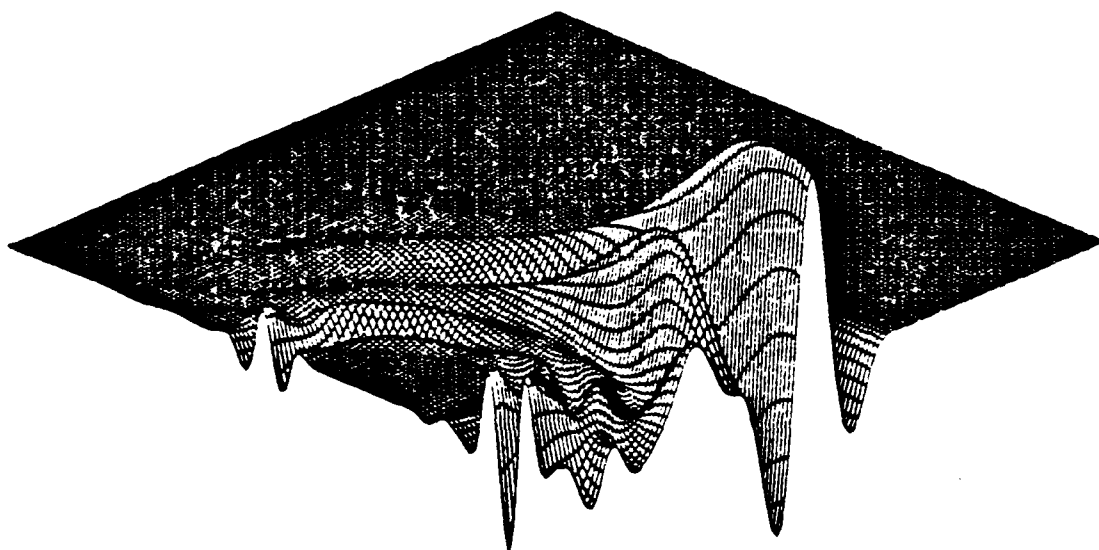


Figure 5.33b: Damped axisymmetric U_z surface plot, $f = 5 \text{ MHz}$ $t = 1.0 \text{ } \mu\text{s}$

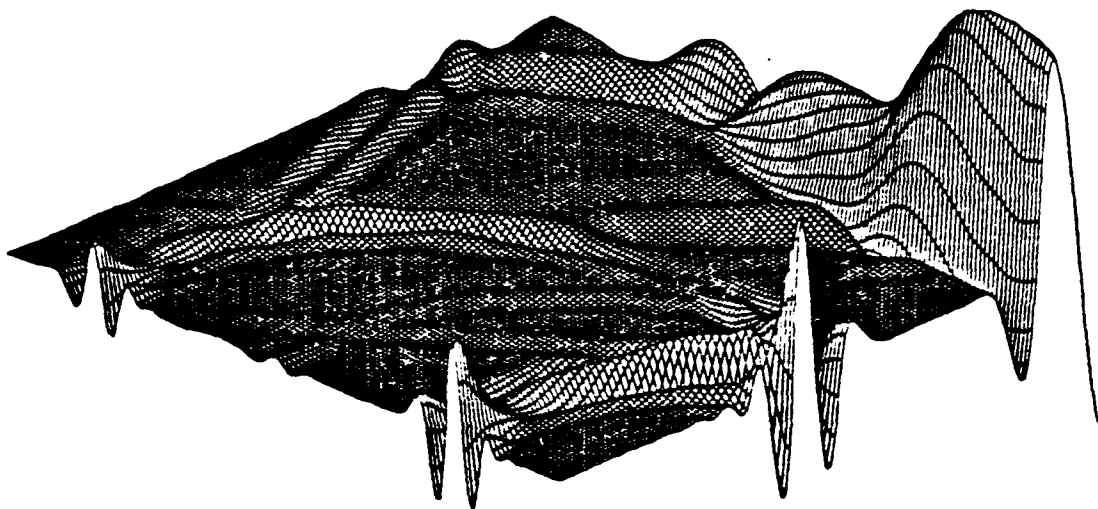


Figure 5.34a: Undamped axisymmetric U_z surface plot, $f = 5 \text{ MHz}$ $t = 2.0 \text{ } \mu\text{s}$

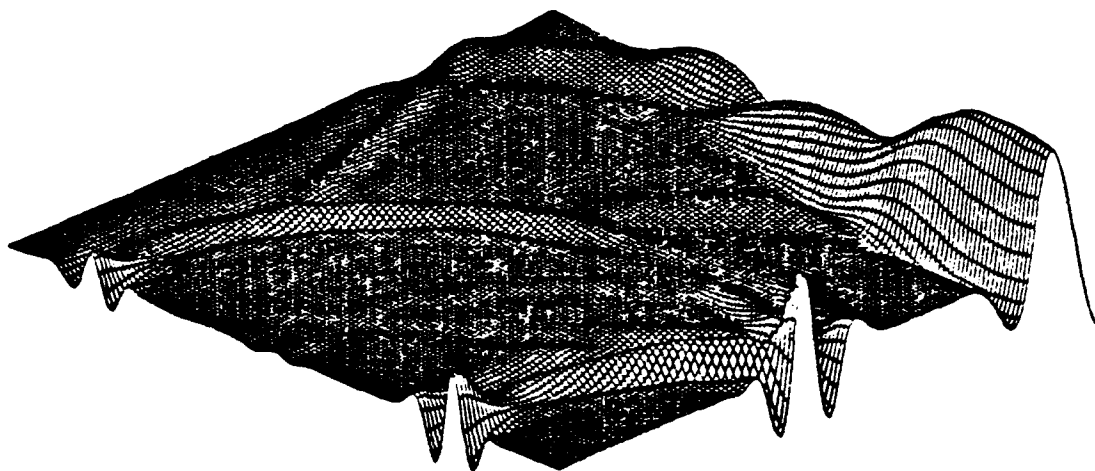


Figure 5.34b: Damped axisymmetric U_z surface plot, $f = 5 \text{ MHz}$ $t = 2.0 \text{ } \mu\text{s}$

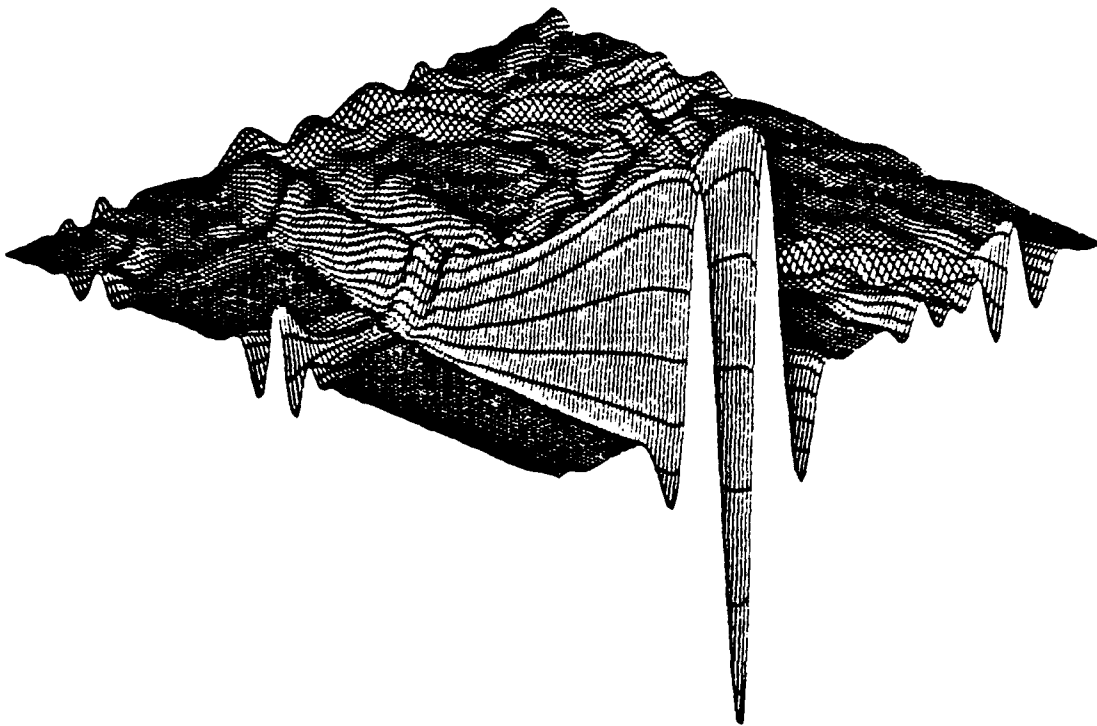


Figure 5.35a: Undamped axisymmetric U_z surface plot, $f = 5 \text{ MHz}$ $t = 3.0 \mu\text{s}$

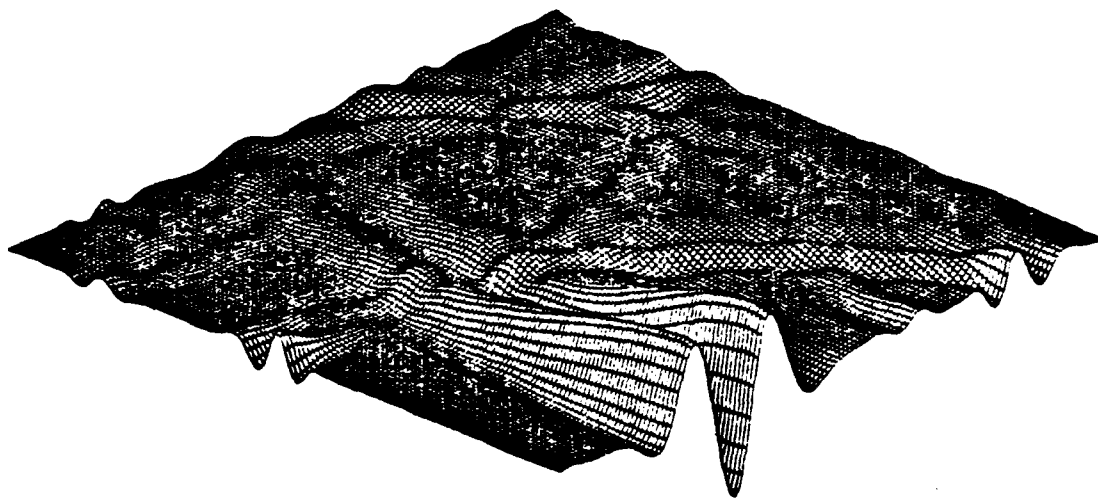


Figure 5.35b: Damped axisymmetric U_z surface plot, $f = 5 \text{ MHz}$ $t = 3.0 \mu\text{s}$

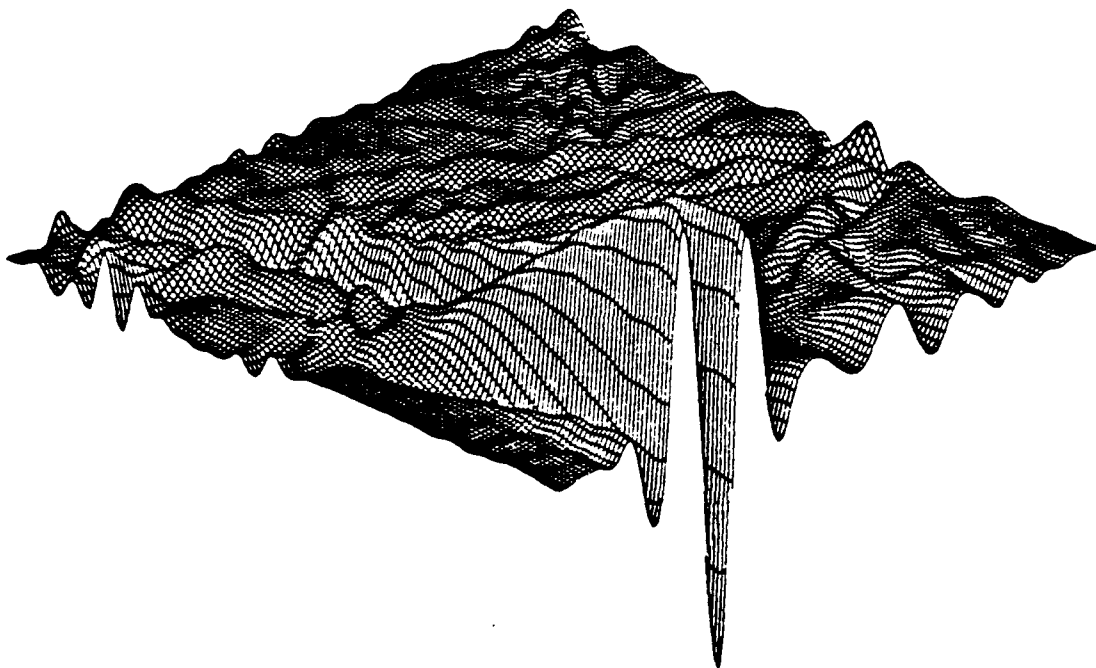


Figure 5.36a: Undamped axisymmetric U , surface plot, $f = 5 \text{ MHz}$ $t = 4.0 \text{ } \mu\text{s}$

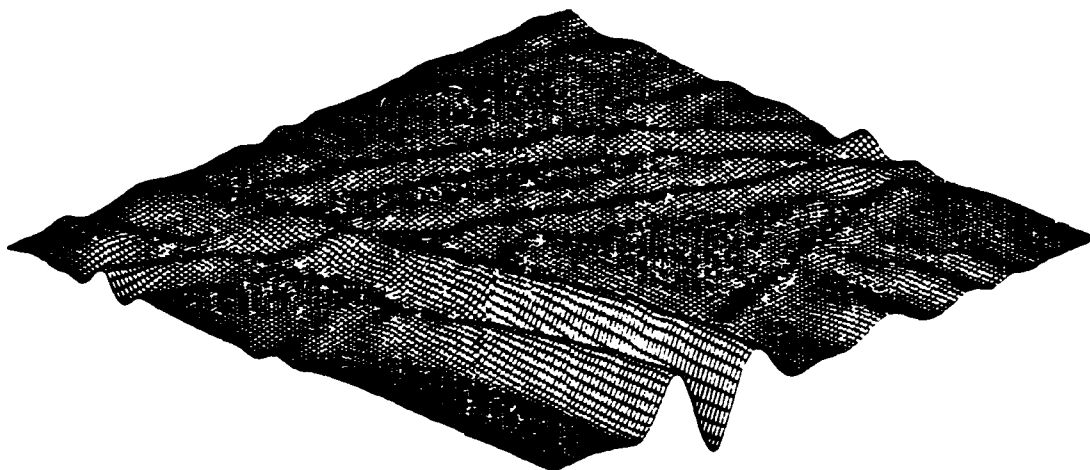


Figure 5.36b: Damped axisymmetric U , surface plot, $f = 5 \text{ MHz}$ $t = 4.0 \text{ } \mu\text{s}$

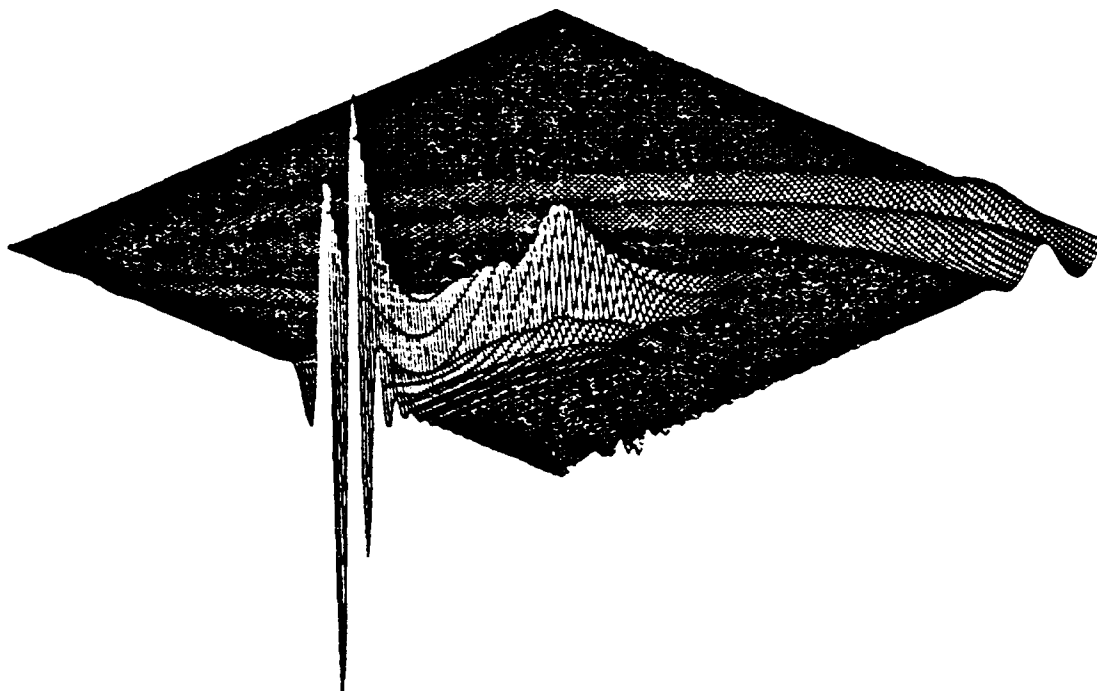


Figure 5.37a: U_x surface plot for transversely isotropic Cobalt, $f = 5 \text{ MHz}$ $t = 1.8 \mu\text{s}$

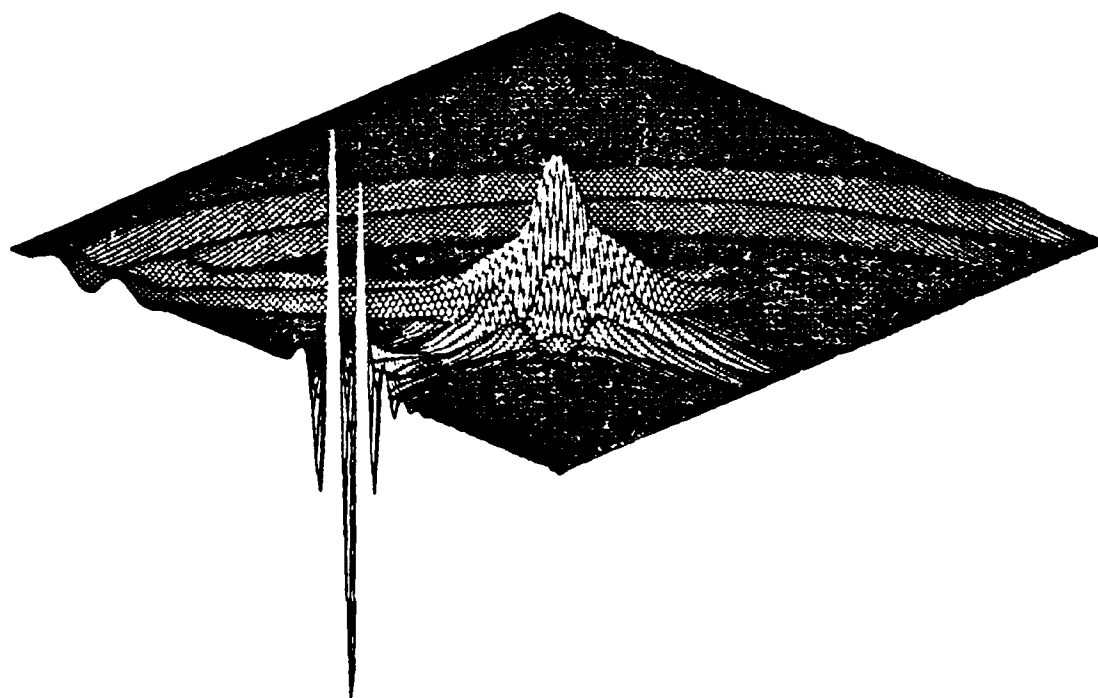


Figure 5.37b: U_y surface plot for transversely isotropic Cobalt, $f = 5 \text{ MHz}$ $t = 1.8 \mu\text{s}$

a point source with a 5 MHz signal. C_{\max} in the Courant constraint is $C_l = \sqrt{\frac{c_{\max}}{\rho}}$. The results are the same as those published [11]. The anisotropic analysis introduces more error into the solution because the wave velocity is now direction dependent. As a result, the Courant constraint varies with direction introducing even more complicated dispersive mesh properties.

REFERENCES

- [1] Segel, E. and Rose, J., "Nondestructive Testing Techniques for Adhesive Bond Joints," in Research Techniques in Nondestructive Testing, Vol. 4, pp. 275-316, (1980).
- [2] Light, G.M. and Kwun, H., "Nondestructive Evaluation of Adhesive Bond Quality," State-of-the-Art Review, SwRI Project 17-7958-838, Southwest Research Institute, San Antonio, Texas, June 1989.
- [3] Aulenbacher, U. and Langenberg, K.J., "Transient Radiation Pattern of Ultrasonic Transducers on Elastic Half-Spaces," in New Procedures in Nondestructive Testing, P. Hoeller, ed., Springer-Verlag, Berlin, 1983.
- [4] Ludwig, R., Moore, D. and Lord, W., "A Comparative Study of Analytical and Numerical Transient Force Excitations on an Elastic Half-Space," *IEEE Transactions on Ultrasonics, Ferroelectrics and Frequency Control*, Vol. 36, No. 3, pp. 342-350, (1989).
- [5] Bond, L.J., Saffari, N. and Punjani, M., "Modelling Ultrasonic Waves Using Finite Difference Methods," in Review of Progress in Quantitative Nondestructive Evaluation, Vol. 6A, D.O. Thompson and D.E. Chimenti, eds., Plenum Press, New York, pp. 135-144, (1987).
- [6] Manolis, G.D., "A Comparative Study on Three B.E.M. Approaches to Problems in Elasto-dynamics," *International Journal for Numerical Methods in Engineering*, Vol. 19, p. 73, (1983).

- [7] Constantino, C.J., "Finite Element Approach to Stress Wave Problems," *Journal of the Engineering Mechanics Division ASCE*, Vol. 93, EM 2, pp. 153-177, (1967).
- [8] Lysmer, J. and Drake, L.A., "A Finite Element Method for Seismology," *Methods in Computational Physics*, Vol. 11, p. 181, (1972).
- [9] Hunt, J.T., Knittel, M.R. and Barach, D., "Finite Element Approach to Acoustic Radiation from Elastic Structures," *Journal of the Acoustical Society of America*, Vol. 55, p. 269, (1974).
- [10] Ludwig, R., "The Finite Element Modeling of Ultrasonic NDT Phenomena," Ph.D. Thesis, Colorado State University, 1986.
- [11] You, Z., Lusk, M., Ludwig, R. and Lord, W., "Numerical Simulation of Ultrasonic Wave Propagation in Anisotropic and Attenuative Solid Materials," *IEEE Transactions on Ultrasonics, Ferroelectrics and Frequency Control*, Vol. 38, No. 5, pp. 436-445, (1991).
- [12] Miyazaki, S. and Chitoshi, M., "Preliminary Study on Ultrasonic Wave Simulation in Qualitative Nondestructive Evaluation," in Review of Progress in Quantitative Nondestructive Evaluation, Vol. 10A, D.O Thompson and D.E. Chimenti, eds., Plenum Press, New York, pp. 153-160, (1991).
- [13] You, Z., Lord, W. and Ludwig, R., "A 3-D Finite Element Formulation for Ultrasonic NDE," in Review of Progress in Quantitative Nondestructive Evaluation, Vol. 10A, D.O Thompson and D.E. Chimenti, eds., Plenum Press, New York, pp. 233-240, (1991).

- [14] Blake, R.J. and Bond, L.J., "Rayleigh Wave Scattering From Three Dimensional Slots," in Review of Progress in Quantitative Nondestructive Evaluation, Vol. 10A, D.O Thompson and D.E. Chimenti, eds., Plenum Press, New York, pp. 113-119, (1991).

- [15] Sullivan, J.M., Ludwig, R., Geng, Y. and Nair, V., "Numerical Comparison of Experimentally Measured Ultrasound Through a Multilayered Specimen," in Review of Progress in Quantitative Nondestructive Evaluation, Vol. 10B, D.O. Thompson and D.E. Chimenti, eds., Plenum Press, New York, pp. 1359-1366, (1991).

- [16] Auld, B.A., Acoustic Fields and Waves in Solids, Vol. 1, Robert E. Krieger Publishing Co., Malabar, Florida, 1990.

- [17] Achenbach, J.D., Wave Propagation in Elastic Solids, North Holland Publishing Co., New York, 1973.

- [18] Finlayson, B.A., The Method of Weighted Residuals and Variational Principles with Application in Fluid Mechanics, Heat and Mass Transfer, Academic Press, New York, 1972.

- [19] Saada, A.S., Elasticity Theory and Applications, Robert E. Krieger Publishing Co., Malabar, Florida, 1974.

- [20] Grandin, H., Fundamentals of the Finite Element Method, Macmillan Publishing Co., New York, 1986.

- [21] Zienkiewicz, O.C. and Taylor, R.L., The Finite Element Method, Vol. 1, McGraw-Hill, New York, 1989.

- [22] Bathe, K.J. and Wilson, E.L., Numerical Methods in Finite Element Analysis, Prentice-Hall Inc. Englewood Cliffs, New Jersey, 1976.
- [23] Zienkiewicz, O.C., "Short Communication - A New Look at the Newmark, Houbolt, and Other Time Stepping Formulas. A Weighted Residual Approach," *Earthquake Engineering and Structural Dynamics*, Vol. 5, pp 413-418, (1977).
- [24] Lord, W., Ludwig, R. and You, Z., "Developments in Ultrasonic Modelling with Finite Element Analysis," *Journal of Nondestructive Evaluation*, Vol. 9, No. 2/3, pp. 129-143, (1990).
- [25] Hinton, E., Rock, T. and Zienkiewicz, O.C., "A Note on Mass Lumping and Related Processes in the Finite Element Method," *Earthquake Engineering and Structural Dynamics*, Vol. 4, pp. 245-249, (1976).
- [26] Belytschko, T., "An Overview of Semidiscretization and Time Integration Procedures," in Computational Methods for Transient Analysis Vol. 1, T. Belytschko and T.J.R. Hughes, eds., North Holland Publishing Co., New York, pp. 1-65, 1983.
- [27] Krieg, R.D. and Key, S.W., "Transient Shell Response by Numerical Time Integration," *International Journal for Numerical Methods in Engineering*, Vol. 7, No. 3, pp. 273-286, (1973).
- [28] Mullen, R. and Belytschko, T., "Dispersion Analysis of Finite Element Semidiscretizations of the Two Dimensional Wave Equation," *International Journal for Numerical Methods in Engineering*, Vol. 18, pp. 11-29, (1982).

- [29] Belytschko, T. and Mullen, R., "On Dispersive Properties of Finite Element Solutions," in Modern Problems in Elastic Wave Propagation, J. Miklowitz and J.D. Achenbach, eds., John Wiley and Sons, New York, pp. 67-82, 1978.
- [30] Ludwig, R. and Lord, W., "A Finite Element Formulation for the Study of Ultrasonic NDT Systems," *IEEE Transactions on Ultrasonics, Ferroelectrics and Frequency Control*, Vol. 35, No. 6, pp. 809-820, (1988).
- [31] Papadakis, E.P., "Ultrasonic Attenuation Caused by Scattering in Polycrystalline Metals," *Journal of the Acoustical Society of America*, Vol. 37, No. 4, pp. 711-717, (1965).
- [32] Hughes, T.J.R. and Lui, W.K., "Implicit-Explicit Finite Elements in Transient Analysis: Stability Theory," *Journal of Applied Mechanics*, Vol. 45, pp. 371-374, (1978).

ULTRASONIC SIGNAL PROCESSING OF ADHESIVE BONDING DATA EMPLOYING CHIRP-Z TRANSFORM AND ADAPTIVE FILTERING TECHNIQUES

V. K. Nair, R. Ludwig, J. M. Sullivan and D. Dai
Department of Electrical Engineering, Worcester Polytechnic Institute
Worcester, Massachusetts 01609, MA

INTRODUCTION

Adhesive bonding has found extensive application in the aircraft and defense industries where the failure of a bond in any of the critical load-bearing components, for example the rotor-blade of an helicopter, can bring about a catastrophic failure. Nondestructive evaluation of adhesively bonded structures attempt to assess the key factors of bond strength and quality. The bond strength [1] is primarily determined by the thickness of the bondline, as this greatly affects the stored energy in the bond. Three factors, if determined, provide a good measure of bond quality. They are bond thickness, contact angle of adhesive to substrate, and substrate surface-free energy.

The objective this paper sets out to achieve is a means of accurately determining the thickness of a bond layer. Digital signal processing is used to analyze the reflected/transmitted data. Both the time domain and frequency domain approaches are investigated. In the frequency domain the Chirp-Z transform [2],[5] is employed to perform the spectral analysis of the received signal. Based on the resonance effect of the bondline the dips in the observed transducer frequency spectra can be correlated to the thickness of the bond. This topic is further discussed in references [6] and [7].

As an alternative, time domain analysis of the reflected signal consists of modeling the bonded structure as an adaptive filter [3], with the taps being representative of the adhesive layer. This technique is used to provide a deconvolved bondline response. Adaptive filters have found wide use in adaptive modeling and system identification in which the unknown system is described by its input-output behavior. The adaptive filter then tries to emulate the system response due to a known input. In its application to deconvolution, the effect of undesired medium

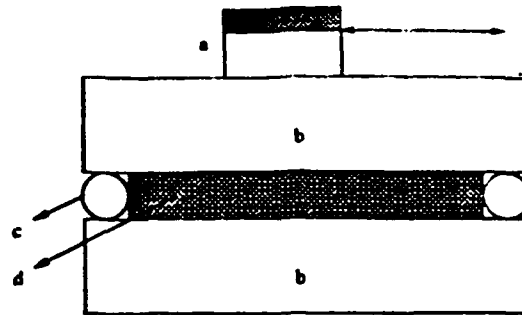


Figure 1: Generic configuration used for the experiments

- a. Transducer in pulse echo mode
- b. Substrate layers
- c. Copper wire spacers
- d. Adhesive layer (Gel)

influence on the signal is sought to be negated. Here the medium which affects the bond-line response can be considered as the cumulative effect of the substrates, the transducer itself and the associated hardware that make up the entire experimental arrangement.

EXPERIMENTAL ARRANGEMENT

The experimental arrangement for this research required the assembly of bonded structures of predetermined thicknesses, as shown in Figure 1. The substrate layers *b*, are optical glass flats of precisely measured thickness. They are approximately isotropic in nature with known material constants. Knowledge of material parameters, like the density and the longitudinal velocity of sound in each of the three layers is essential in determining the thickness of the adhesive layer. The adhesive layer *d*, is simulated by a viscous gel of known material properties. To corroborate the predictions obtained, copper wires *c*, of known diameters were placed as spacers in between the substrates. The contact transducer (0.25 inch aperture) placement *a*, is generally in the Pulse Echo (P.E) mode, with a chosen range of center frequencies between 5-20 MHz.

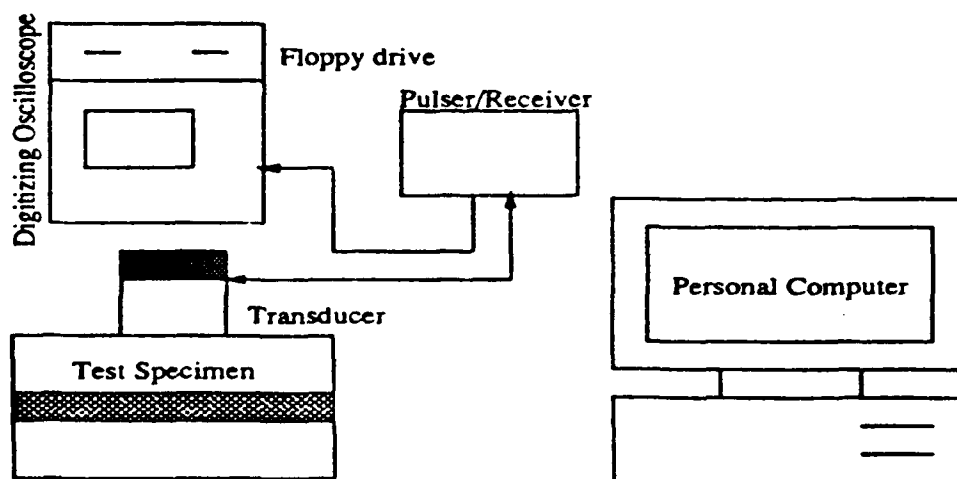


Figure 2: Experimental Arrangement

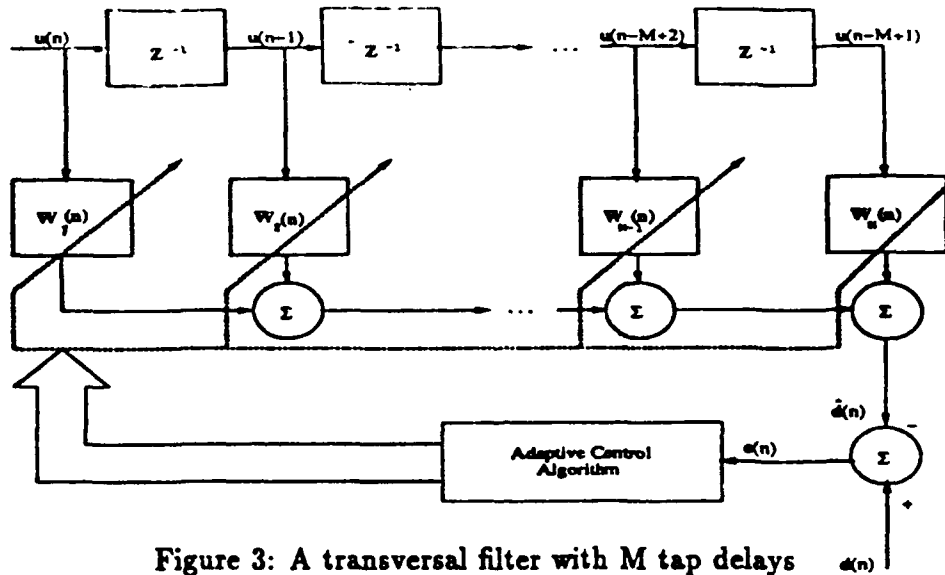


Figure 3: A transversal filter with M tap delays

ADAPTIVE FILTERING APPROACH

Adaptive filters are based mainly on three different approaches: the *Wiener Filter Theory*, the *Kalman Filter Theory*, and the classical *method of least squares*. Since the Wiener and Kalman filters involve a stochastic formulation the deterministic *least squares* approach is chosen. This method requires minimizing an index of performance related to the error. The error is defined as the difference between the desired response and the actual filter output. Three different classes of algorithms form the basis of the method of least squares. They are recursive least squares, least-squares lattice algorithm, and the QR decomposition least squares algorithm. In this paper the *recursive least-squares algorithm* forms the basis of the deconvolution technique.

RECURSIVE LEAST SQUARES ALGORITHM

The structural basis of the recursive least squares (RLS) algorithm is a transversal filter illustrated in Figure 3, where $u(n)$ represents the input to the filter, $d(n)$ represents the desired response, $\hat{d}(n)$ is the output of the filter, and $e(n)$ is referred to as the estimation error. The RLS algorithm starts by defining a correlation matrix $\Phi(n)$ such that

$$\Phi(n) = \sum_{i=1}^n \lambda^{n-i} u(i) u^T(i) \quad \text{where } 0 < \lambda \leq 1 \quad (1)$$

here λ^{n-i} is an exponential weighting factor, or memory factor. The deterministic normal equation is defined as

$$\Phi(n) \hat{w}(n) = \Theta(n) \quad (2)$$

with $\hat{w}(n)$ being the optimum value of the tap-weight vector for which the index of performance attains its minimum value. In equation (2) $\Theta(n)$ is the deterministic cross-correlation vector defined as

$$\Theta(n) = \sum_{i=1}^n \lambda^{n-i} u(i) d(i) \quad (3)$$

The index of performance \mathcal{E} , sought to be minimized in this case is

$$\mathcal{E}(n) = \sum_{i=1}^n \lambda^{n-i} |e(i)|^2 \quad (4)$$

with

$$e(i) = d(i) - \mathbf{w}^T(n) \mathbf{u}(i) \quad (5)$$

Rephrasing equation (2) we can get an expression for the optimal tap-weight vector as

$$\hat{\mathbf{w}}(n) = \Phi^{-1}(n) \Theta(n) \quad (6)$$

The above equation involves the inversion of an M -by- M matrix which is accomplished by employing the Woodbury [3] matrix inversion lemma.

APPLICATION TO BONDED STRUCTURES

Figure 4a illustrates the P.E test of a triple layered medium. The reflected signal $d(t)$ is interpreted to be the convolution of the signal $u(t)$ taken from a single layer of substrate material as shown in Figure 4b, and the adhesive layer, represented as a transfer function $h(t)$ of Figure 4c. The signal $u(t)$ can be considered to have all the external influences sought to be negated from the bondline response. Referring to Figure 3, it can be seen that here the input to the adaptive filter would be $u(t)$ and the desired response to which $u(t)$ is adapted, is $d(t)$. On convergence the filter taps are then representative of the bondline transfer function $h(t)$.

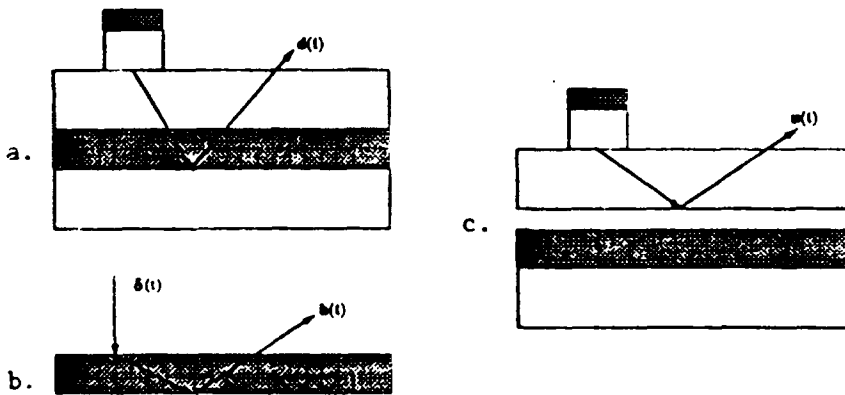


Figure 4: a.Signal from bonded structure $d(t) = u(t) * h(t)$
b.Signal from single layer of substrate material $u(t)$
c.Bondline transfer function $h(t)$

RESULTS

The case study presented here deconvolves the bondline transfer function of a simulated bond of a measured thickness of $117.6 \mu\text{m}$. The adaptive filter set up has 256 taps. The input signal $u(t)$ consists of 512 samples, and the desired response $d(t)$ also has 512 samples, $u(t)$ is delayed by 256 samples to improve performance of the filter [4].

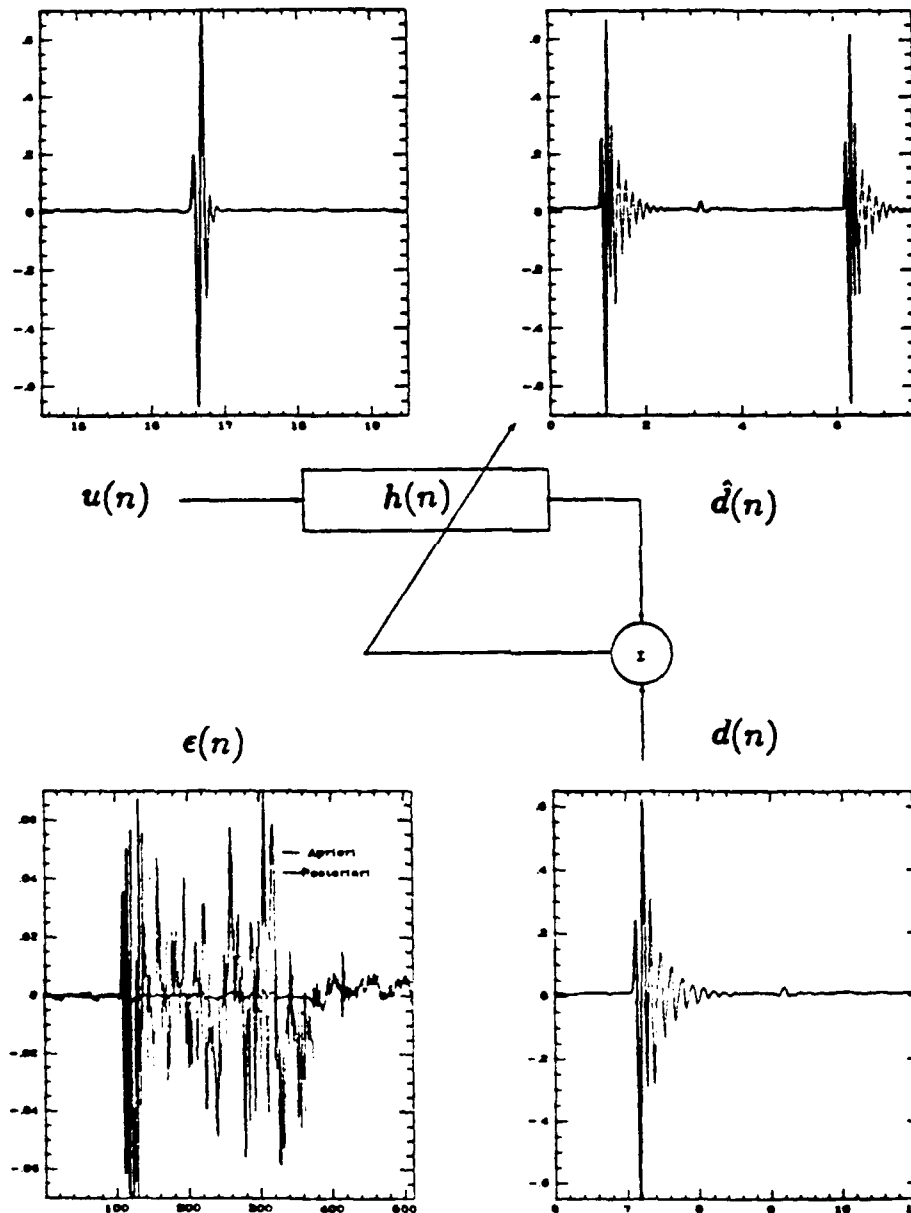


Figure 5: Process of Adaptation

Figure 5 describes the details of the process of adaptation. In this figure $\epsilon(n)$ shows the error signals at each iteration which describe the convergence of the filter. When the *a priori* error and the *a posteriori* error have the same value, the filter has converged to its optimum tap weight vector. The signal $\hat{d}(n)$ describes the predicted output which closely matches $d(n)$. The filter taps on convergence represent the adhesive layer transfer function depicted in Figure 6a. This transfer function is then convolved with an idealized transducer signal having a Gaussian frequency response centered at 10 MHz, shown in Figure 6b.

The result of the convolution is shown in Figure 7a in the time domain. Figure 7b illustrates the frequency domain response of this signal. When the frequency spectrum of the experimentally obtained signal $d(n)$ is overlaid, it can be seen that location of the nulls in either case are in close alignment.

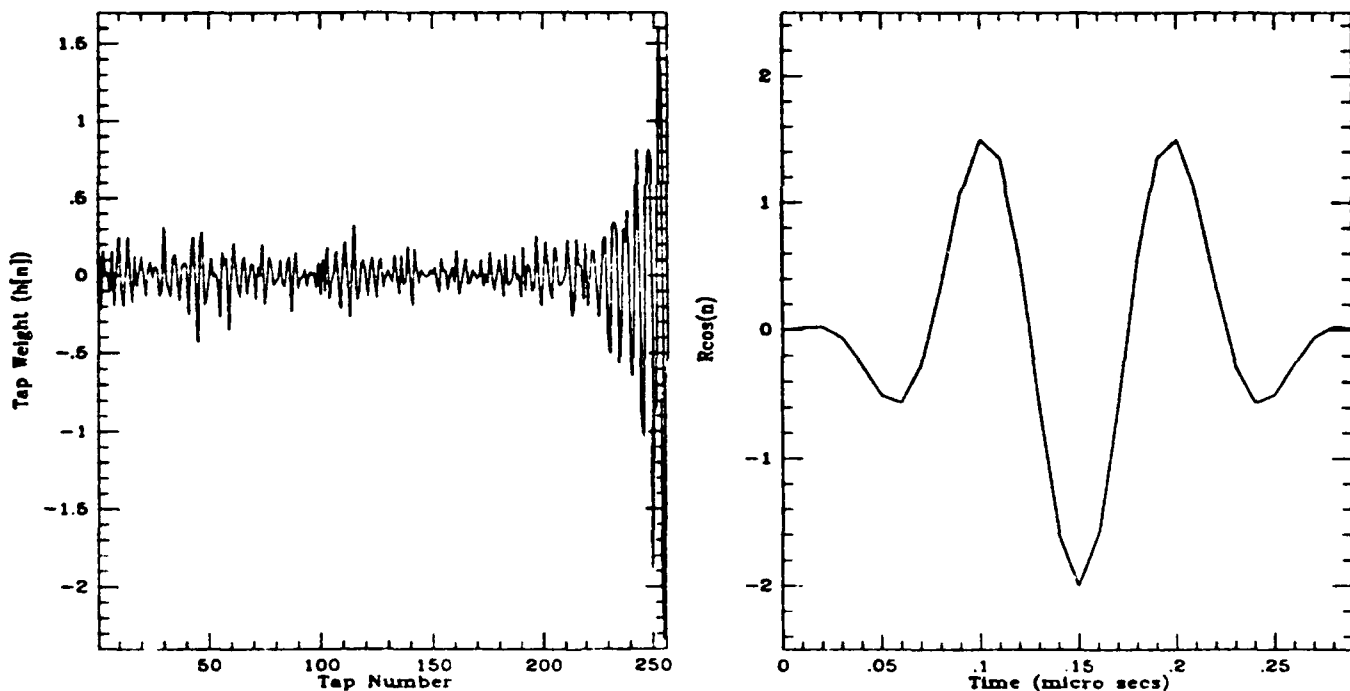


Figure 6: a. Filter taps representing $h(n)$
b. Idealized 10 MHz transducer signal $RCos(n)$

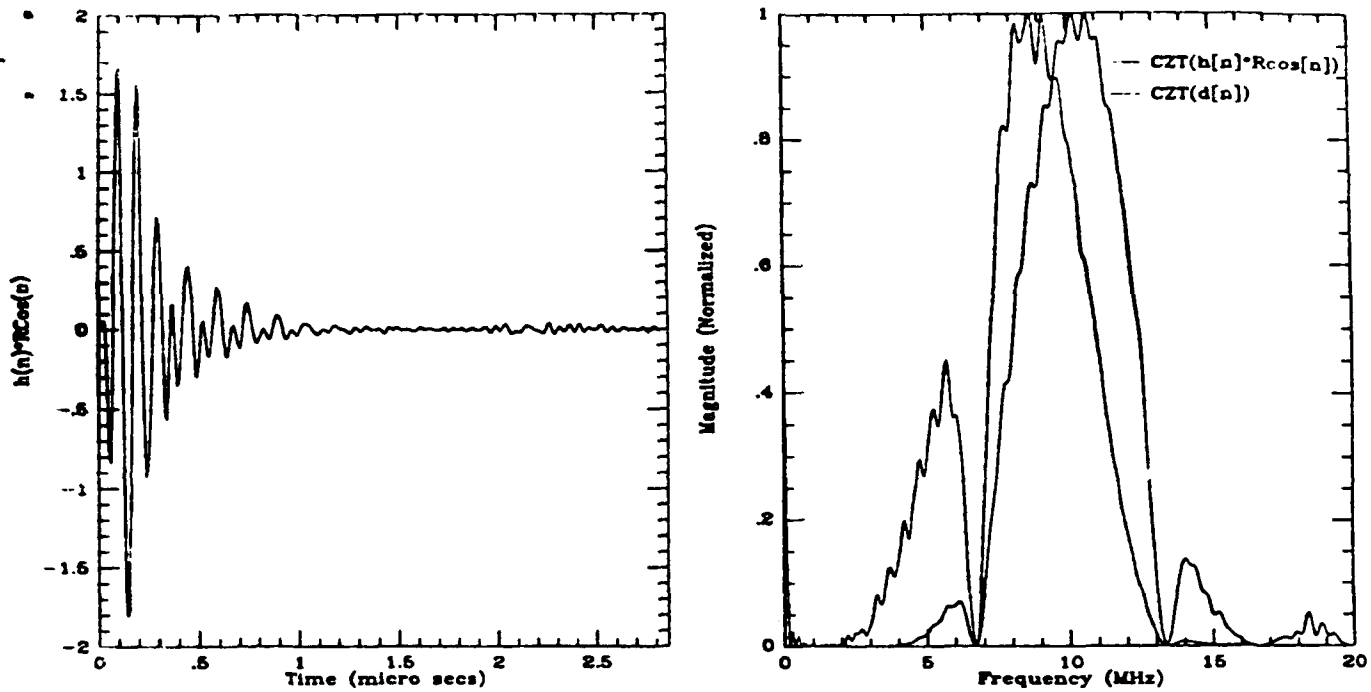


Figure 7: a. Time domain response of $Rcos(n) * h(n)$
b. Frequency domain response of $Rcos(n) * h(n)$

Finally in order to validate the deconvolution model presented here, $u(n)$ and $h(n)$ are convolved and the results compared with $d(n)$. Figure 8a is the time domain response of this convolution which compares favorably with $d(n)$ shown in Figure 5. The comparison in the frequency domain of the signals $u(n) * h(n)$ and $d(n)$ is shown in Figure 8b. As can be seen there is an almost one to one correspondence.

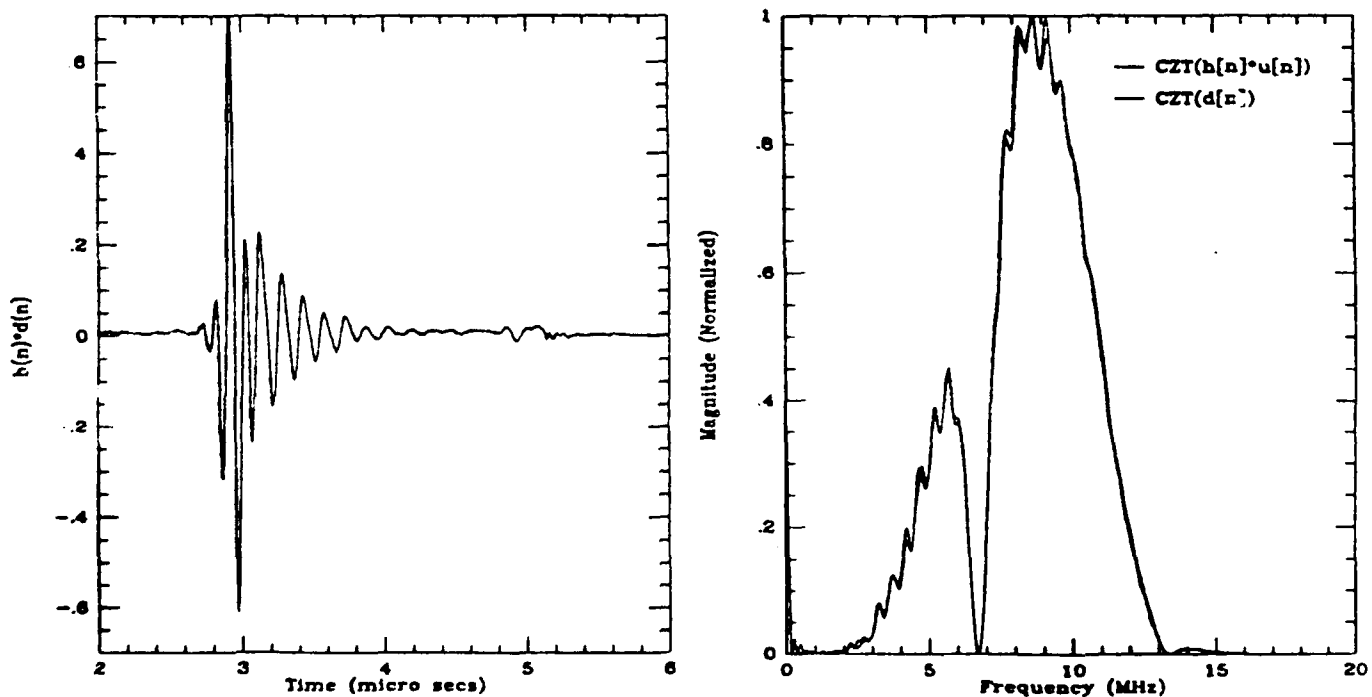


Figure 8: a. Time domain response of $u(n) * h(n)$
b. Frequency domain response of $u(n) * h(n)$

CONCLUSION

This paper discusses the precise thickness measurement of thin adhesive layers by employing a method of deconvolving bondline response. For the thickness measurement a physical model was developed, to which a frequency domain analysis can be applied. Successful measurement of thin layers based on this frequency domain model has been demonstrated [6],[7]. To deconvolve the adhesive layer response a transfer function model is developed based on adaptive filters. The deconvolved bondline transfer function is obtained, and compared to experimentally recorded signals. These comparisons show excellent agreement.

The application of this technique to realistic bonding configurations is one of the future goals. Identification of broad band signals to replace the simulated transducer signal, would provide a better frequency evaluation of the bondline transfer function. Future work may also entail applying the transfer function model to pattern recognition schemes.

REFERENCES

- 1 G.M.Light, H. Kwun, "NONDESTRUCTIVE EVALUATION OF ADEESIVE BOND QUALITY", *STATE-OF-THE-ART REVIEW - SwRI Project 17-7958-838*, Southwest Research Institute, San Antonio, TX, June 1989.
- 2 Alan V. Oppenheim and Ronald W. Schaffer, *Digital Signal Processing*, Prentice-Hall, Inc., Englewood Cliffs, New Jersey, 1975.
- 3 Simon Haykin, *Adaptive Filter Theory*, Prentice-Hall, Inc., Englewood Cliffs, New Jersey, 1986.
- 4 Bernard Widrow and Samuel D. Stearns, *Adaptive Signal Processing*, Prentice Hall, Inc., Englewood Cliffs, New Jersey, 1985.
- 5 Lawrence R. Rabiner and Bernard Gold, "Theory and Application of Digital Signal Processing", Prentice Hall, Inc., Englewood Cliffs, New Jersey, 1975.
- 6 V. K. Nair, R. Ludwig, R Anastasi, "The Chirp Z-Transform Applied to Adhesively Bonded Structures", *IEEE Transactions on Instrumentation and Measurements*, Vol. 40, NO. 4, pp 751-758, August 1991.
- 7 Nair V. K. "Nondestructive Evaluation of Adhesive Bonds", M.S Thesis, 1991, Worcester Polytechnic Institute, Worcester MA.

ACKNOWLEDGEMENT

This work was sponsored, in part, by the U. S. Army Materials Technology Laboratory, Watertown, MA (Reference # DAAL04-90-C-0024).

APPENDIX A

The elastic constitutive matrices for isotropic materials in terms of Lamé's constants are shown in the index contracted forms of the stress strain relations for plane strain in equation (A.1) and for axisymmetry in equation (A.2).

$$\begin{Bmatrix} \sigma_{xx} \\ \sigma_{yy} \\ \sigma_{xy} \end{Bmatrix} = \begin{bmatrix} \lambda+2\mu & \lambda & 0 \\ \lambda & \lambda+2\mu & 0 \\ 0 & 0 & 2\mu \end{bmatrix} \begin{Bmatrix} \varepsilon_{xx} \\ \varepsilon_{yy} \\ \varepsilon_{xy} \end{Bmatrix} \quad (\text{A.1})$$

$$\begin{Bmatrix} \sigma_{zz} \\ \sigma_{rr} \\ \sigma_{\theta\theta} \\ \sigma_{rz} \end{Bmatrix} = \begin{bmatrix} \lambda+2\mu & \lambda & \lambda & 0 \\ \lambda & \lambda+2\mu & \lambda & 0 \\ \lambda & \lambda & \lambda+2\mu & 0 \\ 0 & 0 & 0 & 2\mu \end{bmatrix} \begin{Bmatrix} \varepsilon_{zz} \\ \varepsilon_{rr} \\ \varepsilon_{\theta\theta} \\ \varepsilon_{rz} \end{Bmatrix} \quad (\text{A.2})$$